HIGH-PERFORMANCE SIGNAL ACQUISITION ALGORITHMS FOR WIRELESS COMMUNICATIONS RECEIVERS

A Dissertation

by

KAI SHI

Submitted to the Office of Graduate Studies of
Texas A&M University
in partial fulfillment of the requirements for the degree of

DOCTOR OF PHILOSOPHY

August 2005

Major Subject: Electrical Engineering

HIGH-PERFORMANCE SIGNAL ACQUISITION ALGORITHMS FOR WIRELESS COMMUNICATIONS RECEIVERS

A Dissertation

by

KAI SHI

Submitted to the Office of Graduate Studies of
Texas A&M University
in partial fulfillment of the requirements for the degree of

DOCTOR OF PHILOSOPHY

Approved by:

Chair of Committee,	Erchin Serpedin
Committee Members,	Scott L. Miller
	Xi Zhang
	Andreas Klappenecker
Head of Department,	Chanan Singh

August 2005

Major Subject: Electrical Engineering

ABSTRACT

High-Performance Signal Acquisition Algorithms
for Wireless Communications Receivers. (August 2005)
Kai Shi, B.Sc., Nanjing University, Nanjing, China;
M.Eng., Southeast University, Nanjing, China
Chair of Advisory Committee: Dr. Erchin Serpedin

Due to the uncertainties introduced by the propagation channel, and RF and mixed signal circuits imperfections, digital communication receivers require efficient and robust signal acquisition algorithms for timing and carrier recovery, and interference rejection.

The main theme of this work is the development of efficient and robust signal synchronization and interference rejection schemes for narrowband, wideband and ultra wideband communications systems. A series of novel signal acquisition schemes together with their performance analysis and comparisons with existing state-of-the-art results are introduced. The design effort is first focused on narrowband systems, and then on wideband and ultra wideband systems.

For single carrier modulated narrowband systems, it is found that conventional timing recovery schemes present low efficiency, e.g., certain feedback timing recovery schemes exhibit the so-called hang-up phenomenon, while another class of blind feedforward timing recovery schemes presents large self-noise. Based on a general research framework, we propose new anti-hangup algorithms and prefiltering techniques to speed up the feedback timing recovery and reduce the self-noise of feedforward timing estimators, respectively.

Orthogonal frequency division multiplexing (OFDM) technique is well suited for wideband wireless systems. However, OFDM receivers require high performance car-

rier and timing synchronization. A new coarse synchronization scheme is proposed for efficient carrier frequency offset and timing acquisition. Also, a novel highly accurate decision-directed algorithm is proposed to track and compensate the residual phase and timing errors after the coarse synchronization step. Both theoretical analysis and computer simulations indicate that the proposed algorithms greatly improve the performance of OFDM receivers.

The results of an in-depth study show that a narrowband interference (NBI) could cause serious performance loss in multiband OFDM based ultra-wideband (UWB) systems. A novel NBI mitigation scheme, based on a digital NBI detector and adaptive analog notch filter bank, is proposed to reduce the effects of NBI in UWB systems. Simulation results show that the proposed NBI mitigation scheme improves significantly the performance of a standard UWB receiver (this improvement manifests as a signal-to-noise ratio (SNR) gain of 9 dB).

To my parents and wife

ACKNOWLEDGMENTS

I would like to thank my advisor, Professor Erchin Serpedin, for his constant support, guidance and inspiration during my years at TAMU. This research work would never have been accomplished without his encouragement and help.

Special thanks goes to Prof. Scott L. Miller for teaching me modulation theory and serving as a member of my Ph.D. committee. I would also like to thank Prof. Xi Zhang and Prof. Andreas Klappenecker for serving on my advisory committee. I am also thankful to some professors in our department, Prof. Krishna R. Narayanan for his lectures on coding theory, and Prof. Aydin Karsilayan for his inspiration and guidance when I was working on the UWB project.

I also enjoyed working with many colleagues in the Wireless Communications Laboratory (WCL), and in particular I would like to thank Dr. Yang Wang, Yik-chung Wu, Dr. Zhongmin Liu, Dr. Shengjie Zhao, Dr. Jing Li, Dr. Guoshen Yue, Nitin A. Nangare, Janath Peiris, Dr. Vivek Gulati, Hari Sankar, Yong Sun and Jun Zheng. I owe also special thanks to some researchers from the Analog and Mixed Signal Group at TAMU: Burak Kelleci, Timothy Fischer, and Haitao Tong.

I would like to thank Dr. Zoran Zvonar, Dr. Aiguo Yan, Deepak Mathew and Lidwine Martinot for their encouragement and guidance when I worked as a system engineering intern at Analog Devices. This successful experience will have a strong impact on my future career.

Finally, I would like to express my gratitude to my parents and sister for their encouragement and constant support. This dissertation is dedicated to my wife, Likun Cao. Her love, understanding and encouragement represented the momentum to complete this Ph.D. program.

TABLE OF CONTENTS

CHAPTER Page

Page

LIST OF TABLES

LIST OF FIGURES

FIGURE Page

FIGURE Page

FIGURE Page

CHAPTER I

INTRODUCTION

A. Background

Thanks to its convenience, wireless communication is a promising technology and is becoming dominant among all *last-one-mile* technologies. To transmit data symbols over the air efficiently, wireless transceivers often involve carrier modulation. In the transmitter, after digital-to-analog (D/A) conversion, the complex baseband signals are modulated to high frequency signals by I (in phase) and Q (quadrature) modulator. At the receiver, the received signals are converted into the baseband by IQ demodulator. Then some optimal or sub-optimal detectors can be used for data recovery. Due to the RF imperfections and the uncertainty of propagation channel, the received signals could be seriously distorted and interfered by other wireless systems.

As shown in Fig. 1, to compensate various distortions and interferences, the digital receiver requires efficient carrier and timing recovery, channel estimation and interference rejection schemes. This family of algorithms is generally referred to as signal acquisition. Efficient and robust signal acquisition algorithms are very critical for the success of data recovery. Note that, for some wireless systems, only some blocks in Fig. 1 are required and their processing flow may be different from the order shown in Fig. 1.

References [1] - [4] are excellent books on carrier and timing recovery that have been reported in the literature. In addition, most of the existing results on interference rejection were well summarized in [5]- [6] and their references. The goal of this dissertation is to build a general framework for signal acquisition and explore high-

---

The journal model is *IEEE Transactions on Automatic Control.*

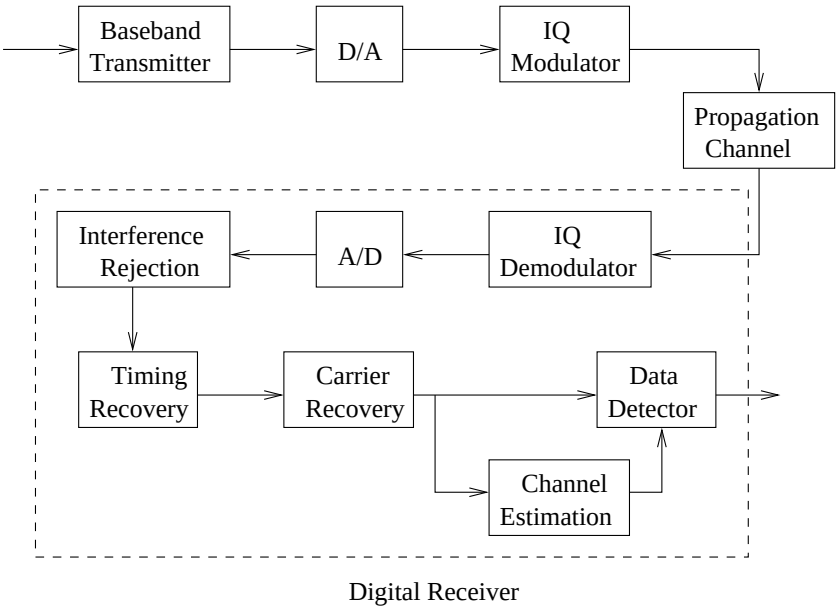

Fig. 1. Signal acquisition at digital receiver.

performance algorithms for various wireless systems. Note that channel estimation is not the focus of this dissertation and some existing work on channel estimation can be found in [1]- [2].

Depending on whether the receiver knows the transmitted data or not, the signal acquisition schemes can be classified into three broad categories: data-aided (DA), decision-directed (DD), and non-data aided (NDA) or blind. All these schemes will be addressed in this dissertation, e.g., the DA scheme is used for coarse synchronization of OFDM receivers (Chapter IV), the DD scheme is used for fine synchronization of OFDM receivers (Chapter V), and NDA schemes are discussed in Chapters II and III.

1. Timing Recovery

In digital communication receivers, the received signal is sampled by means of an analog to digital (A/D) converter. However, there is an arbitrary symbol timing delay between the receiver and transmitter, which is not known by the A/D converter. To get correct data strobe for detection, the digital receiver requires timing recovery. At first, the timing offset is estimated using the received data and then a timing error controller is used to compensate the estimated timing offset. Depending on the type of compensation method used, timing recovery schemes can be classified into two classes: feedback and feedforward. In the feedback timing recovery scheme shown

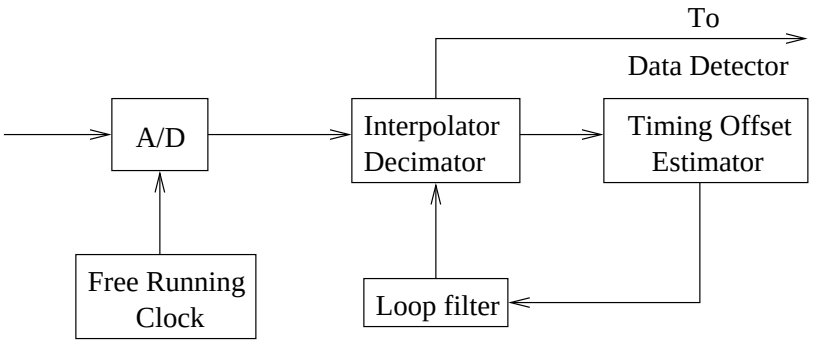

Fig. 2. Feedback timing recovery scheme.

in Fig. 2, the estimated timing error is fed back to adjust the time offset of digital interpolator (or A/D converter) and the resulting new samples are used to estimate the residual timing error. Based on this iterative operation, the system timing error converges to the stable operation point. Thanks to its simplicity, the feedback scheme is often used in practice. However, for certain initial values of the timing error, the acquisition time of blind feedback timing recovery schemes could be extremely large. This problem is called hang-up [7]- [9] and will be addressed in Chapter II. As shown in Fig. 3, a typical feedforward timing recovery scheme uses the estimated timing offset

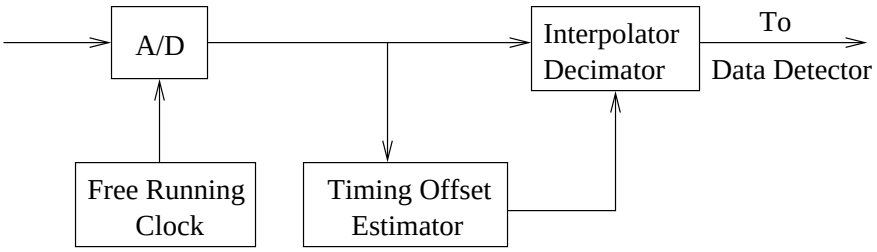

Fig. 3. Feedforward timing recovery scheme.

to control the digital interpolator. Since there is no feedback between the timing offset estimator and timing error controller, the hang-up phenomenon is avoided in feedforward systems [10]- [15]. However, the feedforward timing estimator presents the self-noise which is embedded in most of blind estimators [16].

2. Carrier Recovery

Due to the imperfections in oscillators and Doppler shifts introduced by the propagation channel, carrier frequency and phase offsets are present in the received signal. The carrier synchronization task resumes to estimating and compensating these offsets at the receiver. Compared to single carrier systems, orthogonal frequency division multiplexing (OFDM) systems [17] are very sensitive to carrier frequency offsets. Several schemes have been proposed for coarse estimation of the carrier frequency offset [18]- [26], which are not efficient in terms of performance and complexity. Therefore, an important effort in this dissertation is allocated to the problem of carrier synchronization for OFDM systems. For OFDM receivers, the performance of carrier frequency offset estimator depends on the initial timing synchronization. Therefore, the timing synchronization of OFDM receivers will be also explored in this work.

As shown in Fig. 4, the synchronization of OFDM systems consists of two steps: coarse and fine synchronization. The coarse synchronization step assumes the task of

removing the large timing and carrier frequency offsets before the fast Fourier transform (FFT) block. After coarse synchronization, the received signal is converted into the frequency domain and might still present residual phase and timing errors. Without compensation, these residual errors could introduce significant performance loss. Since these residual errors are small in magnitude, fine synchronization is normally performed in the frequency domain using tracking.

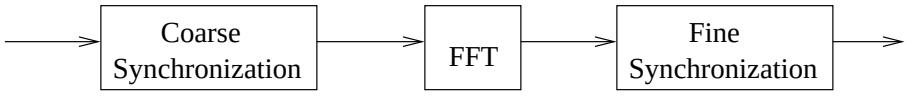

Fig. 4. Coarse and fine synchronization of OFDM receiver.

3. Interference Mitigation

Ultra-wideband (UWB) [27] systems provide high data rate, low-power, huge spatial capacity and high precision ranging for the quickly growing home networking market.

Since UWB systems use very low transmission power and operate at license-free bands [28], a narrowband interference (NBI) might represent a very critical obstruction for the successful operation of UWB systems. It is found that the NBI could cause serious performance loss for these systems. Conventional NBI mitigation schemes [5]-[6] requires high precision ADC and are not feasible for UWB receivers. Designing low complexity and robust NBI mitigation schemes for UWB receivers will represent an additional major research thrust of this work.

B. Organization of Dissertation

The unifying feature of this work is the development of robust and efficient signal acquisition and interference cancellation schemes for general narrowband, wideband

and ultra wideband communication systems. Novel and high performance signal synchronization schemes are first proposed for narrowband communication systems in Chapters II and III of this work. In Chapters IV and V, the analysis is focused on the important problem of designing robust and efficient signal acquisition algorithms for the class of wideband systems belonging to the OFDM family. Finally, Chapter VI explores the applicability and robustness of the wideband signal interception schemes to ultra wideband systems. Also, Chapter VI proposes a novel, robust and high performance narrowband interference mitigation scheme for the family of multiband OFDM-based UWB transceivers.

All the proposed signal acquisition and interference mitigation schemes are introduced gradually starting with narrowband systems, then extending the analysis to wideband and ultra wideband systems. Fig. 5 illustrates how this dissertation is structured.

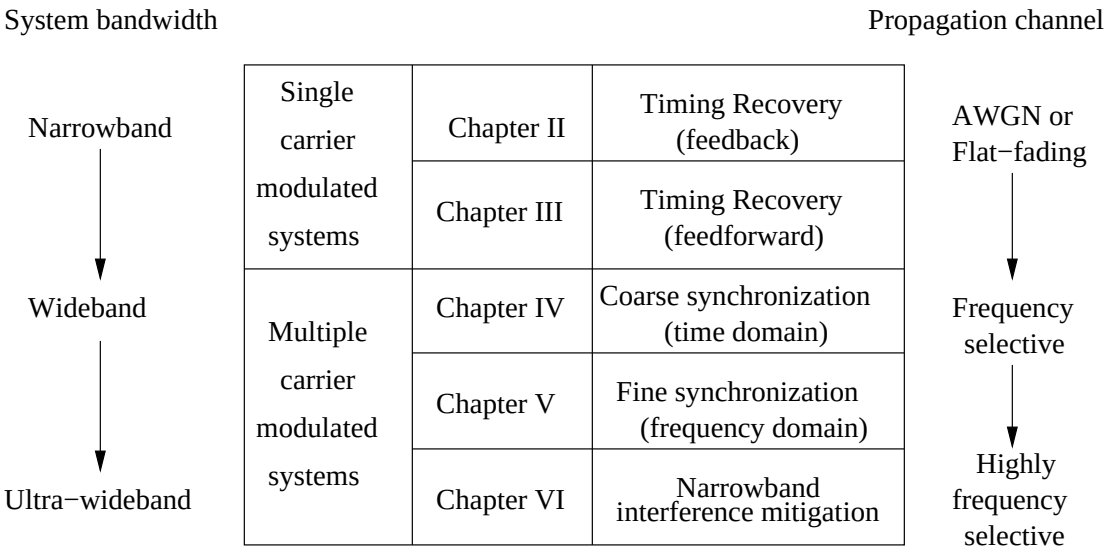

Fig. 5. Content and organization of dissertation.

In Chapters II and III, we will focus on exploring the high-performance timing

recovery schemes for narrowband systems, where the wireless propagation channel can be assumed to be AWGN channel or flat fading channel.

Chapter II deals with the well known hang-up problem for blind feedback timing recovery schemes. When the initial timing offset of blind feedback timing recovery scheme is close to half of symbol period, the acquisition time becomes extremely long. A novel low complexity anti-hangup algorithm will be proposed to resolve the hang-up problem. Simulation results show that the proposed algorithm greatly reduces the probability of hang-up and speeds up the feedback timing recovery.

The performance of blind feedforward timing recovery scheme will be analyzed in Chapter III. It is found that the feedforward timing recovery schemes exhibit a large self-noise especially for systems with small roll-off factors. The statistical analysis of self-noise leads to a novel prefiltering scheme, which can be used to reduce the self-noise of blind feedforward timing estimators.

Chapter IV, V and VI deal with high performance synchronization and interference mitigation algorithms for wideband and ultra-wideband systems, where the propagation channel could be highly frequency-selective.

Chapter IV deals with coarse carrier and timing synchronization for OFDM receivers. A novel and robust synchronization scheme is proposed for efficient carrier frequency offset and timing acquisition.

Fine synchronization (tracking) in frequency domain is discussed in Chapter V. A new decision directed algorithm is proposed to track the residual phase and timing error. Both theoretical analysis and computer simulations indicate that the proposed algorithms greatly improve the efficiency and performance of standard OFDM receivers.

Chapter VI is dedicated to the problem of narrowband interference mitigation in multiband OFDM (MB-OFDM) UWB systems. A new NBI cancellation scheme,

based on a digital NBI detector and adaptive analog notch filter bank, is proposed to reduce the effects of NBI on UWB systems. Simulation results show that the proposed scheme improves significantly the performance of UWB receivers, an improvement which translates into an SNR gain of 9 dB. It should be noted that some research results on the adaptive analog notch filtering were contributed in collaboration with other researchers: Burak Kelleci, Timothy W. Fischer and Dr. Aydın İlker Karsilayan. In fact, their contributions proved to be of fundamental importance for this study, and of very substantial value.

Some concluding remarks are provided in Chapter VII. Appendices A-F present some mathematical results that are used in the previous chapters.

CHAPTER II

FAST FEEDBACK TIMING RECOVERY FOR NARROWBAND SYSTEMS

A. Introduction

Thanks to its simplicity and robust tracking capability, the digital phase-lock loop (PLL) is often used for timing recovery [4]. Normally, the digital PLL for timing recovery consists of three elements, which include a timing error detector to estimate the current timing error, a lowpass loop filter to decrease the estimation error and a timing corrector to control the timing error.

Fast timing acquisition and good tracking performance are desirable but are difficult to achieve simultaneously because the design of PLL is a trade-off between acquisition time and tracking error. In noise-free channels, as long as the loop filter is determined, the average acquisition time should be a constant. However, for some timing error detectors [29]- [31], the PLL occasionally presents a very long acquisition time, a phenomenon which is referred to as the hangup problem [7]- [9]. The slow timing recovery is undesirable especially for burst transmission systems.

By introducing a hysteresis effect using a special preamble sequence, the authors of [32] proposed a fast timing recovery scheme to avoid the hangup in the decision-directed timing synchronizer [29]. However, this method works only for partial-response signals. The hangup problem also exists in blind timing synchronizers [30]- [31] for linear and non-linear modulations and it requires a more general approach.

To resolve this problem, in this chapter we propose a novel two-step hangup robust timing recovery scheme. Based on an initial estimate obtained in the first step, we try to reduce the timing uncertainty from $[-T/2, T/2]$ to $[-T/4, T/4]$ (T is

the symbol period), and thus to avoid the hangup in the second step. The increased complexity is very low since the proposed scheme can use the same timing error detector as that used in the conventional scheme. We provide simulation results for two well-known timing error detectors [30]- [31] and show that the proposed scheme greatly speeds up the timing recovery for both linearly and nonlinearly modulated transmissions [1].

B. Signal Model and Feedback Timing Recovery

In AWGN channels, the received signal can be expressed by

$$r(t) = x(t) + n(t) \ , \tag{2.1}$$

where $x(t)$ represents the transmitted linearly or non-linearly modulated signal and $n(t)$ denotes the band-limited additive noise. In (2.1), we omit carrier frequency offset since timing synchronizer to be discussed is robust to such small frequency offset.

After passing through matched filter, the received signal becomes $y(t)$. At times $lT - \epsilon T$, the sampled signal can be expressed as

$$y_l(\epsilon) = y(lT - \epsilon T) \ , \tag{2.2}$$

where T, l and ϵT represent the data symbol period, the data symbol index and the fractional timing offset in the analog to digital converter (ADC), respectively. For simplicity, we omit the carrier frequency offset and phase offset in (2.2) since the timing estimators we will use later are robust to these offsets.

The standard digital phase-lock loop (PLL) is often used for timing recovery. The digital PLL for timing recovery is usually made up of three elements [1]- [2]: a timing error detector (TED), a loop filter and a timing corrector. First, the TED

outputs a symbol-rate error signal $e(l)$, which depends on the time estimates $\{\hat{\epsilon}_l\}$. Reference [30] provides the derivation of a lot of timing error detectors which can be blind, decision directed or data-aided. In this chapter, we focus on blind timing error detectors. Note that the PN sequence synchronization for the spread spectrum receiver is out of the interests of this chapter. For linearly modulated signals, the Gardner's TED [30] can be used

$$e(l) = \mathrm{Re}\left\{ y^*_{l-1/2}(\hat{\epsilon}_{l-1}) \left[y_{l-1}(\hat{\epsilon}_{l-1}) - y_l(\hat{\epsilon}_l) \right] \right\} \ . \tag{2.3}$$

For minimum shift keying (MSK) type signals, the Mengali's TED [31] and [1] can be used

$$\begin{aligned} e(l) \ := \ & e(l, D) = (-1)^{D+1} \mathrm{Re}\left\{ y^2_{l-1/4}(\hat{\epsilon}_{l-1}) y^{*2}_{l-D-1/4}(\hat{\epsilon}_{l-D-1}) \right. \\ & \left. - y^2_{l+1/4}(\hat{\epsilon}_l) y^{*2}_{l-D+1/4}(\hat{\epsilon}_{l-D}) \right\} \end{aligned} \tag{2.4}$$

In (2.4), D is a design parameter and should be a positive integer. It is pointed out in [1] that $D = 1$ is preferable for MSK and $D = 2$ leads to the best performance for Gaussian MSK (GMSK). From the above equation, the sampling clock for Gardner's TED and Mengali' TED should be at least $T_s = T/2$ and $T_s = T/4$, respectively. The error signal is used to recursively update the timing estimates in the loop filter. For the first-order loop filter, the updating equation is given by:

$$\hat{\epsilon}_l = \hat{\epsilon}_{l-1} - \gamma e(l) \ , \tag{2.5}$$

where γ denotes the step size.

Finally, the timing estimates $\hat{\epsilon}_l$ are exploited to control the timing corrector. Depending on the sampling scheme, the timing correction can be realized with different methods. If synchronous sampling is used, the timing estimates are fed into a number

controlled oscillator (NCO) to adjust the sampling clock in the ADC. If asynchronous sampling is used, as shown in Fig. 6, the sampling clock in ADC is free running and the timing errors are corrected by a digital timing interpolator [33]- [34]. Since the asynchronous sampling easily leads to high performance all-digital receivers, we will focus on asynchronous sampling hereafter. It should be also mentioned that the proposed scheme works for synchronous sampling. In Fig. 6, after timing acquisition is obtained, the decimator outputs symbol-rate samples to data detector. For linearly modulated systems, the lowpass filter can be a matched filter while for nonlinearly modulated systems, an anti-alias lowpass filter should be used.

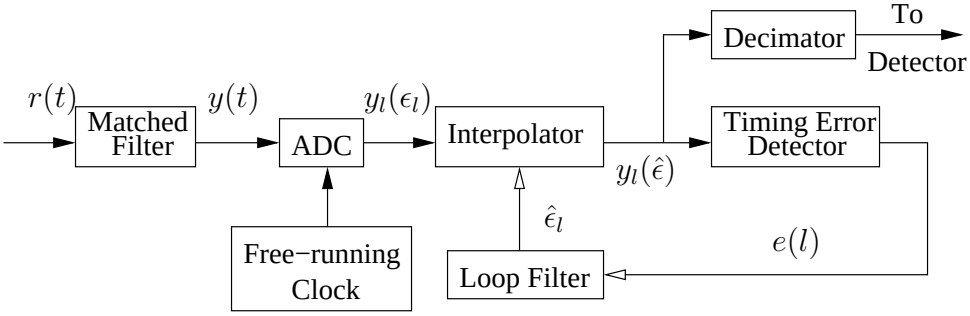

Fig. 6. Conventional timing recovery scheme.

C. Hangup in Digital PLL

The design of a loop filter is in general a trade-off between acquisition timing and tracking performance. In particular, for the first-order loop filter, if the step-size γ is reduced, the PLL needs a longer acquisition time, while the tracking error becomes smaller.

The S-curve of the timing error detector is often used to investigate the performance of PLL and is defined by the conditional expectation of the timing error

signal:

$$S(\delta) = \mathrm{E}\{e(l)|\delta\} \ , \tag{2.6}$$

where δ is the difference between the true time offset and the current timing estimate $\delta = (\hat{\epsilon}_l - \epsilon_l)T$. It is the S-curve that determinates the strength of pulling the PLL from the initial timing offset to the stable point $\delta = 0$. Also, the acquisition and tracking performance depends on the loop filter. From [1], the loop bandwidth during tracking is given by

$$B_L T = \frac{\gamma A}{4 - 2\gamma A} \ , \tag{2.7}$$

where A is the slope of S-curve at $\delta = 0$ and $\gamma A < 2$ is assumed. In noise-free channels, the acquisition time of the digital PLL can be approximated by (pp. 403-404, [2])

$$T_{acq} \approx \frac{2|\epsilon_0|}{B_L} \ , \tag{2.8}$$

which depends on the loop bandwidth and initial timing offset ϵ_0. Assuming $\epsilon_0' s$ are uniformly distributed over $[-1/2, 1/2]$, we obtain the average acquisition time

$$\bar{T}_{acq} = \frac{1}{2B_L} = \frac{(2 - \gamma A)T}{A} \ . \tag{2.9}$$

Therefore, in noise-free channels, the acquisition time of the digital PLL is often assumed to be inversely proportional to the loop bandwidth B_L. However, for some timing recovery schemes, the digital PLL occasionally requires a very long acquisition time. This phenomenon is called hangup and often happens in PLLs [7]- [9].

In Fig. 7, we plot the S-curves of different timing error detectors in noise-free channels. For Gardner's TED, we assume that the system uses a QPSK modulation and a raised cosine (RC) filter with roll-off factor $\rho = 0.5$. For Mengali's TED, a GMSK modulated system with pre-modulation bandwidth $BT = 0.3$ is assumed. These simulation parameters will be used throughout this chapter.

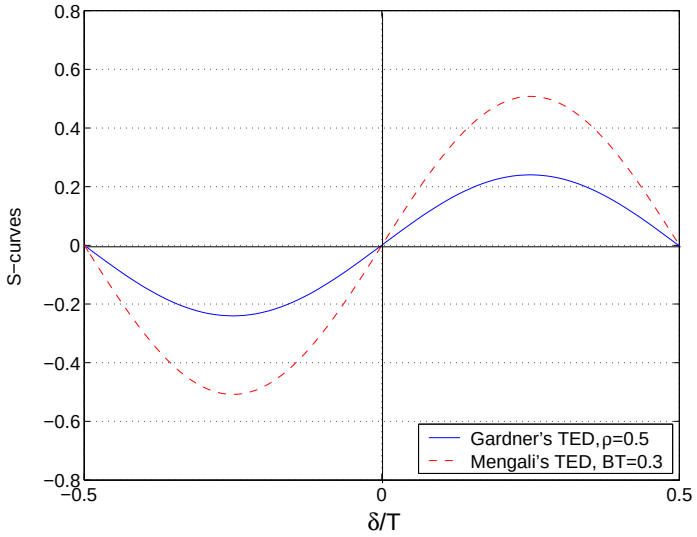

Fig. 7. The S-curves of timing error detectors.

The above S-curves have nulls at $\delta = 0$, which corresponds to the desirable stable point. However, the S-curves have additional zeros at $\delta = \pm T/2$. Therefore, if the initial timing offset is close to $\pm T/2$, the average output of TED will be very small. Due to the small pull-in strength at $\delta = \pm T/2$, it often takes the PLL a very long time to converge to the stable point.

In Fig. 8, the Gardner' TED is used and we plot the time errors versus the number of symbols for different initial timing offsets ϵ_0. In the case of $\epsilon_0 T = 0.45T$, the PLL presents monotonic convergence. However, when $\epsilon_0 T = 0.5T$, the PLL fluctuates around $0.5T$ for a long time before it begins to converge toward the stable point.

D. Anti-hangup Timing Recovery Scheme

To remedy the hangup problem, one may use different loop filters during acquisition and tracking (pp. 405-406, [2]), e.g., to obtain fast acquisition, one may use a larger step size, which is replaced by a smaller step size to reduce the mean-square error during tracking. It is found that the probability of hangup is greatly reduced (but

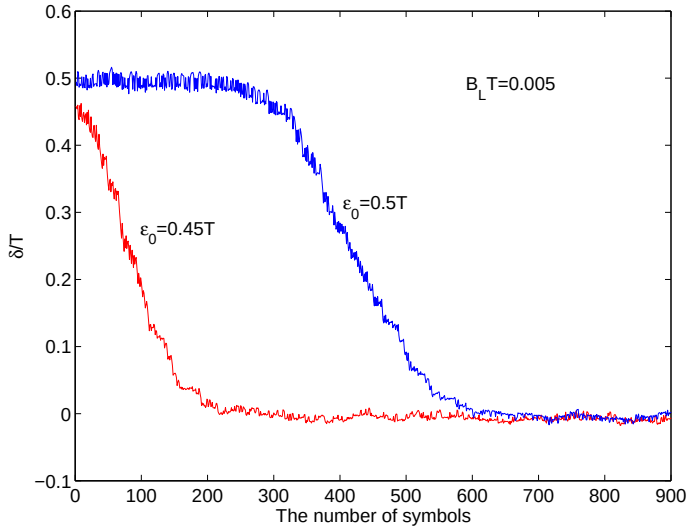

Fig. 8. Timing errors versus the number of symbols for Gardner's TED.

not avoided) by this method.

From the discussion in Section III, we know that the hangup will happen only if the initial timing offset is close to $\pm T/2$. For discussion purpose, we divide the whole range of timing uncertainty into two subsets: $t_1 = [-T/4, T/4]$ and $t_2 = (T/4, T/2] \cup [-T/2, -T/4)$. If the subset of initial timing error is known in the receiver, we may be able to avoid hangup by proper controlling. In the timing error detector, shifting the samples by $T/4$ in (2.6), we obtain the shifted S-curves:

$$S_s(\delta) = E\{e(l - 1/4)|\delta\} \ . \tag{2.10}$$

As shown in Fig. 9, the shifted S-curves are even functions and cross the zero axis at $\delta = \pm T/4$. Also, $S_s(\epsilon_0)$ can be estimated as follows

$$S_1 = \frac{1}{L} \sum_{l=0}^{L-1} e(l - 1/4) \ , \tag{2.11}$$

where we assume that the timing corrector and loop filter are not working during

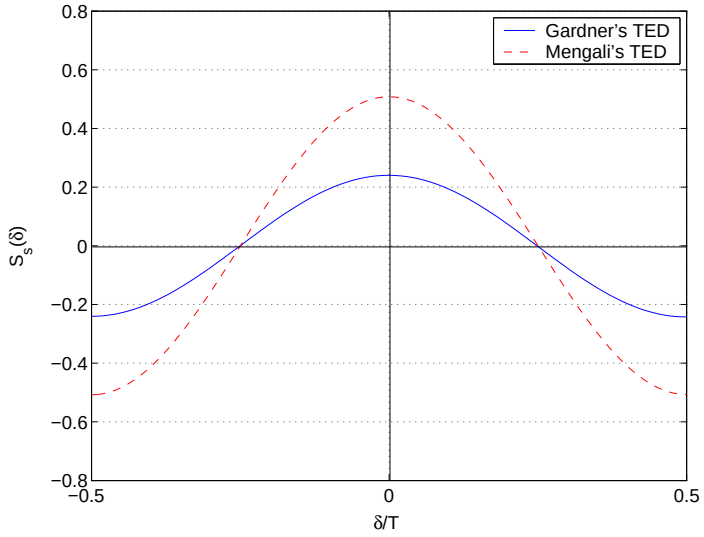

Fig. 9. The shifted version of S-curves.

$t < LT$ and $\hat{\epsilon}_l = 0$ for $l < L$. Thus, the subset of initial timing offset may be easily detected as follows

$$\epsilon_0 T \in t_1 \text{ if } S_1 \geq 0 \text{ or } \epsilon_0 T \in t_2 \text{ if } S_1 < 0 \ . \tag{2.12}$$

If we detect $\epsilon_0 T \in t_1$, $e(l)$ should be used to update the timing estimates in the loop filter $t > LT$ and the decimator outputs $y_l(\hat{\epsilon}_l)$ for data detection. However, if $\epsilon_0 T \in t_2$ is detected, to avoid hangup, we should use $e(l - 1/2)$ to control the loop filter. Assuming the coarse detections are always correct, we obtain the new S-curves in Fig. 10. Besides the stable point at $\delta = 0$, there are two additional stable points at $\delta = \pm T/2$. If $\epsilon_0 T \in t_1$, the PLL will converge to $\delta = 0$. However, if $\epsilon_0 T \in t_2$, it will converge to $\delta = \pm T/2$. Thus, to obtain correct data detection, $y_{l\pm 1/2}(\hat{\epsilon}_l)$ should be used in the decimator for $\epsilon_0 \in t_2$.

Based on above results, in Fig. 11, we propose a new fast timing recovery scheme which assumes a two-step operation:

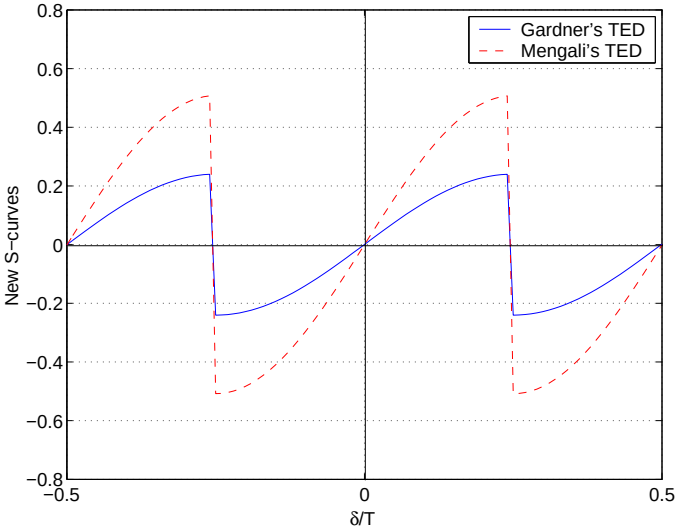

Fig. 10. The new S-curves.

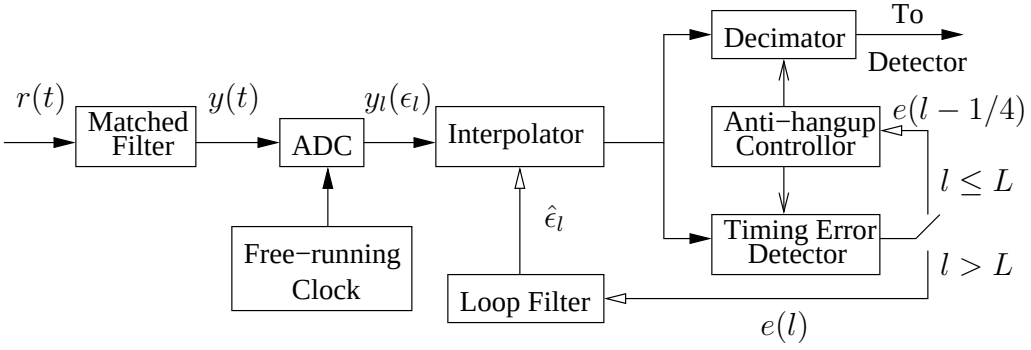

Fig. 11. Fast timing recovery scheme.

1. Feedforward estimation during $t \leq LT$ according to (2.11). The output of timing error detector is switched to the accumulator in the anti-hangup controller, then the feedfoward estimation is used to obtain the coarse information (t_1 or t_2) of $\epsilon_0 T$ using (2.12).

2. Feedback timing recovery during $t > LT$. Depending on the coarse timing information obtained in the first step, the TED selects a proper set of samples to estimate timing errors and update the loop filter for tracking.

The performance of the new scheme depends on the design parameter L. If L is too small, the estimate S_1 will be unreliable and will result in incorrect timing detection, which may further lead to hangup. Assuming hangup will happen only if $\delta_0 = \pm T/2$, the conditional probability

$$P_h := \text{Prob}\left\{[S_1 > 0 | \epsilon_0 T = \pm T/2] \cup [S_1 < 0 | \epsilon_0 T = 0]\right\}$$

should be kept very low to avoid hangup. On the other hand, if in the first step we choose L too large, the overall acquisition time may be increased compared to the conventional scheme. Therefore, small L should be chosen as long as P_h is kept low. Although the variance of $e(l)$ in Gardner's TED can be calculated as [35], it is found that $e(l)$ can not be approximated to be Gaussian distributed for nonzero δ. Thus, it is very difficult to obtain the theoretical value of P_h. In Fig. 12, we plot the simulation results of P_h versus different $L's$ for both Gardner's TED and Mengali's TED. For Gardner's TED with $\rho = 0.5$, $L = 20$ may be enough to keep P_h low. However, due to its higher order (4th order) nonlinearity (2.4), Mengali's TED does not perform well at low SNR and requires a longer L. As pointed out in [36], averaging $e(l, D)$ over different values of D can improve the performance of feedforward estimation. Thus,

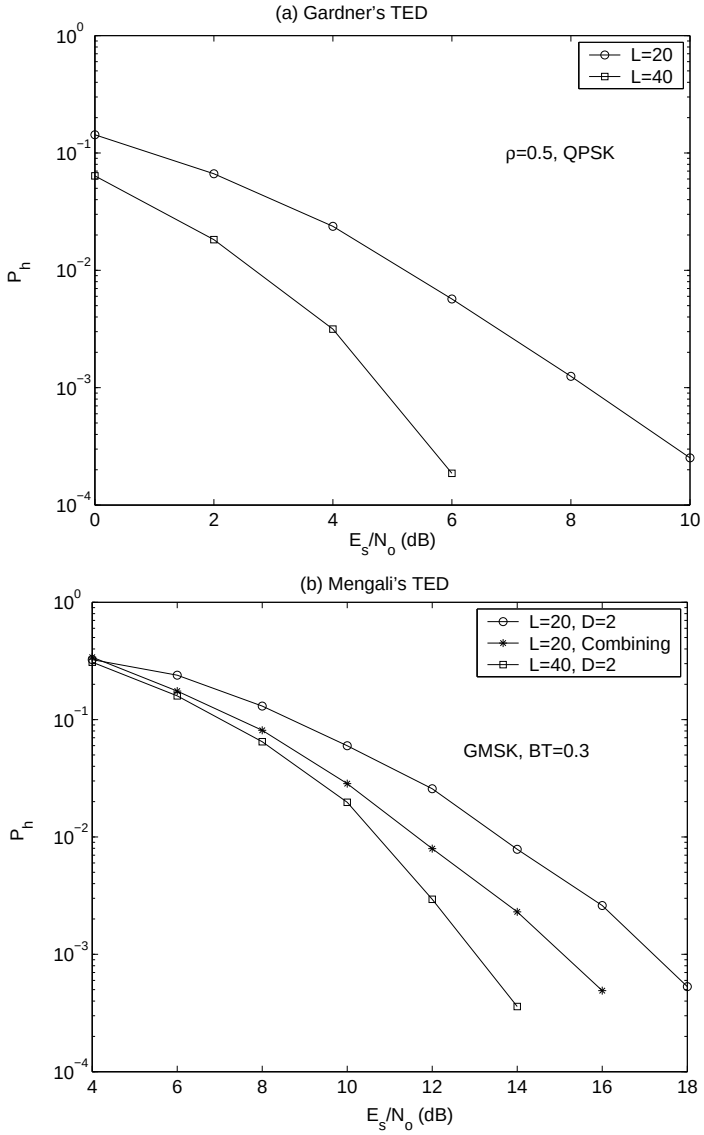

Fig. 12. P_h versus different L.

in the first step operation, the following estimator can be used to reduce P_h:

$$S_2 = \frac{1}{3L} \sum_{D=1}^{3} \sum_{l=0}^{L-1} e(l - 1/4, D) \ . \tag{2.13}$$

As shown in Fig. 12 (b), for the same L, the simulated P_h with the above combining estimator is much lower than the P_h obtained with estimator (2.4).

To verify the advantage of the proposed timing recovery scheme, we run simulations to compare the performance of the different timing recovery schemes. In simulations, we assume a system with QPSK modulation and a RC filter with $\rho = 0.5$. For conventional and proposed schemes, the step size of loop filter is fixed to $\gamma = 0.013$, which leads to a loop bandwidth during tracking: $B_L T = 0.005$. Also, $L = 20$ symbols are used during the first step of the proposed scheme.

For the adaptive loop filter scheme, to speed up the acquisition, a larger step size $\gamma = 0.026$ is used during initial acquisition. According to (pp. 405-406, [2]), for Gardner's TED, $e(l - 1/4)$ can be used to detect if PLL is in lock. From [30], denoting $H(f)$ as the Fourier transform of RC filter, we can express the expectation of $e(l - 1/4)$ by

$$\mathrm{E}[e(l - 1/4)] = \cos(2\pi\delta) \cdot \frac{2}{T} \int_{-1/2T}^{1/2T} H(f - \frac{1}{2T}) H(f + \frac{1}{2T}) \cos(\pi f T) df \ , \tag{2.14}$$

which is maximum when the PLL is in lock. A low-pass filter is used to average $e(l - 1/4)$

$$L_d(l) = \gamma_f L_d(l - 1) + (1 - \gamma_f) e(l - 1/4) \ , \tag{2.15}$$

where γ_f denotes the forgetting factor and our simulations assume $\gamma_f = 0.95$. $L_d(l)$ is then compared with an appropriate threshold T_{hr} for lock detection. As long as the PLL is in lock, the step size of loop filter will be changed to $\gamma = 0.013$ to reduce the tracking error. A threshold of $T_{hr} = 0.11$, which is a half of (2.14) when $\delta = 0$

and $\rho = 0.5$, is used in simulations.

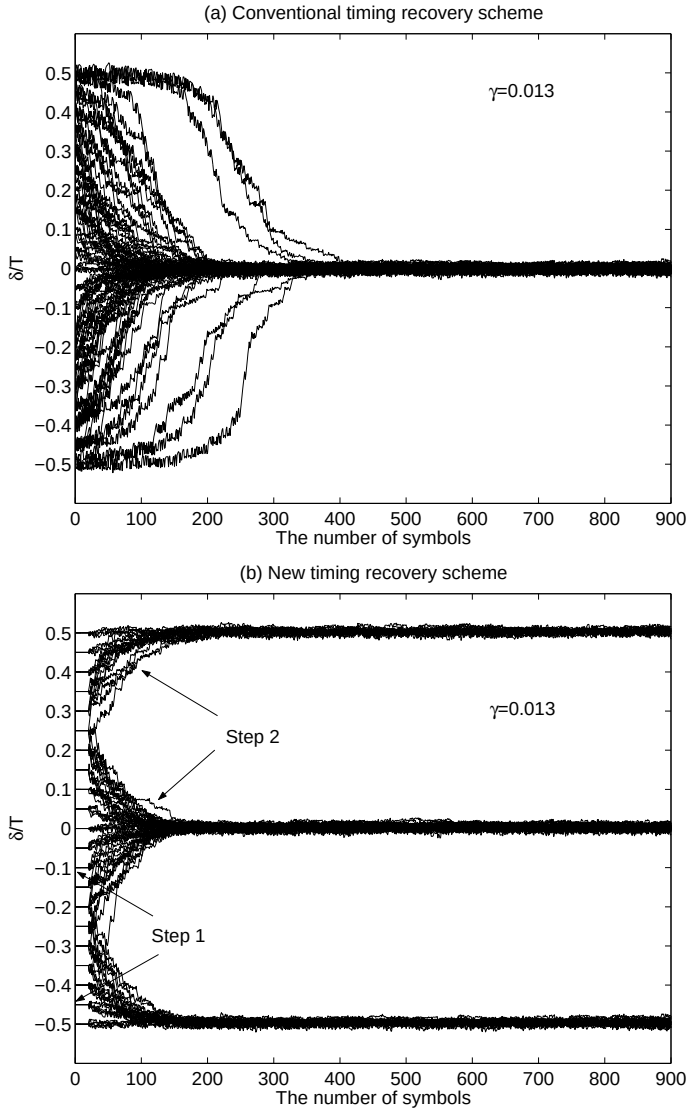

Fig. 13. Performance comparison in AWGN channels, $E_s/N_o = 15$ dB, 100 runs.

Fig. 13 shows 100 runs in AWGN channels, using different initial timing offsets and noise sequences. Figs. 13 (a), (b) are the simulation results of the conventional scheme, the proposed scheme, and adaptive loop filter scheme, respectively. Since all schemes use the same loop bandwidth during tracking, they present similar tracking

error. However, their acquisition performance is very different. For the conventional scheme, although all runs finally converge to $\delta = 0$, sometimes the acquisition is very slow. In 5 out of 100 runs, the convergence to $\delta = 0$ is not achieved even after 300 symbols. On the other hand, the proposed scheme exhibits fast time recovery. For all experiments using the proposed scheme, the convergence is obtained in less than 150 symbols.

Interesting enough, the timing acquisition of the proposed scheme is even faster than that of conventional scheme when $\epsilon_0 T \neq \pm T/2$. This can be explained by the smaller timing uncertainty obtained in the feedfoward estimation of proposed scheme. In noise-free channels, assuming ϵ_0 are uniformly distributed over $[-T/4, T/4]$ after feedforward estimation, we obtain the average acquisition time of proposed scheme

$$\bar{T}_{acq} = \frac{1}{4B_L} + LT \ , \tag{2.16}$$

which is only a half of (2.9) if LT is omitted.

It is noticed that the proposed scheme presents three stable points $(0, \pm T/2)$, which verifies our previous discussion. However, correct data strobes can be obtained by properly controlling the decimator in Fig. 11.

The performance of conventional and proposed timing recovery schemes is also evaluated in flat fading channels. Due to the channel fading, the received signal exhibits a large dynamic range, which may lead to a variable loop bandwidth. To keep the loop bandwidth constant, before the signal enters the timing loop, a AGC is used to normalize the received signal by using the root mean-square of the received signal vector. As shown in Fig. 14, compared to the conventional scheme, the proposed scheme also presents faster acquisition in fading channels.

Similar improvements can be found for the timing recovery schemes that assume Mengali's TEDs in MSK-type systems. These results verify that the proposed scheme

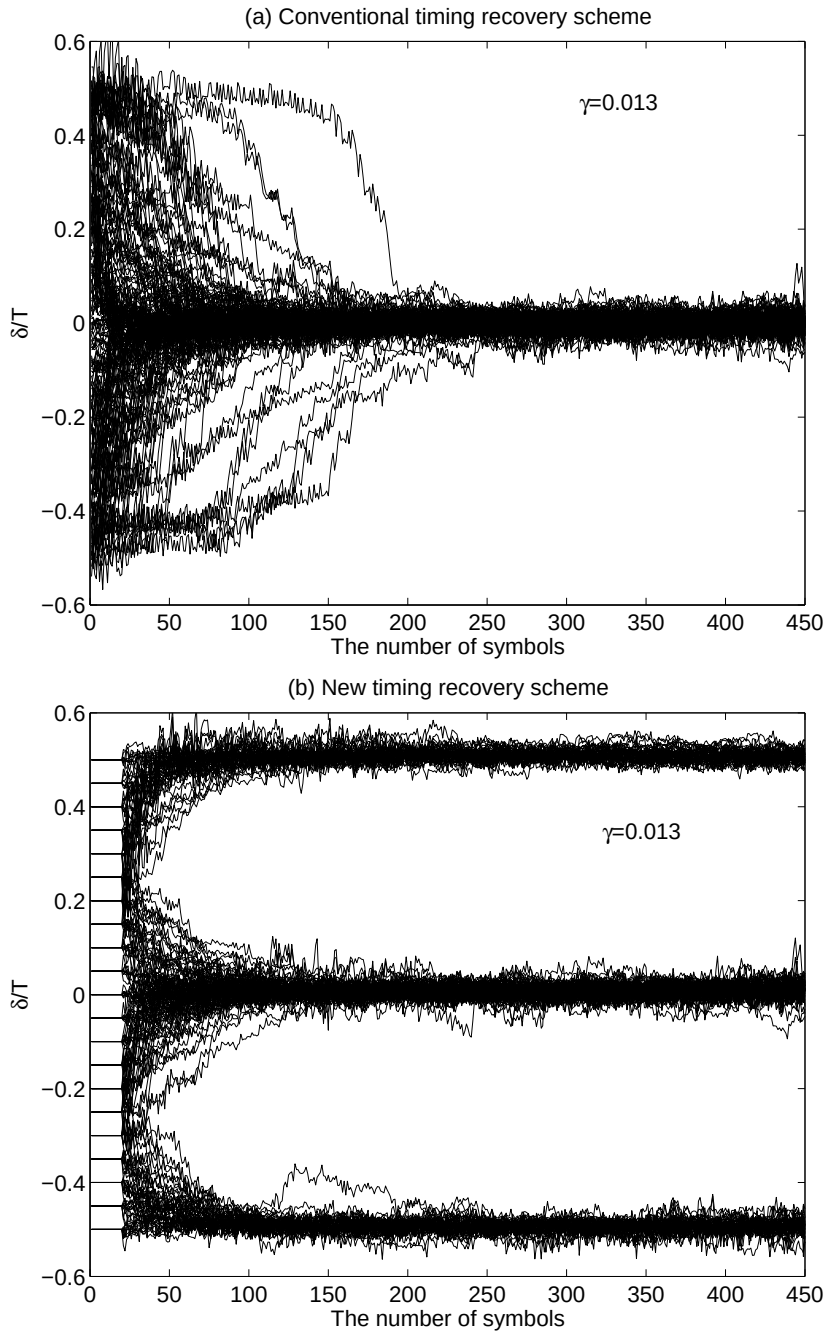

Fig. 14. Performance comparison in flat fading channels, $B_L T = 0.01$, $E_s/N_o = 20$ dB, $f_d T = 0.0002$.

greatly speeds up the timing acquisition.

We remark that it is not free to achieve fast time recovery. Although the same TED can be used in the two schemes, the proposed scheme requires an additional anti-hangup controller. Thus, the proposed scheme slightly increases the complexity of timing synchronization. Furthermore, the original Gardner's TED assumes only two samples per symbol while the proposed scheme requires four samples per symbol. It should be mentioned we do not increase the sampling requirement for Mengali's TED which originally assumes four samples per symbol [31].

E. Summary

In this chapter we have proposed a new anti-hangup timing recovery scheme which assumes a two-step operation. Based on the initial timing estimate obtained in the first step, we reduce the timing uncertainty from $[-T/2, T/2]$ to $[-T/4, T/4]$, and thus avoid the hangup phenomenon in the second step. For two well-known timing error detectors, we show through simulation results that this simple scheme greatly speeds up the timing recovery for both linearly and nonlinearly modulated systems.

Blind feedforward timing estimator [10] was proposed to avoid hang-up problem. However, some blind feedforward estimator present error floors at hight SNR, which is caused by the self-noise [7]. In next chapter, a novel prefilter will be proposed to reduce the self-noise of feedward timing estimators.

CHAPTER III

JITTER-FREE FEEDFORWARD TIMING RECOVERY FOR NARROWBAND SYSTEMS

A. Jitter-Free Prefilter for Feedforward Timing Recovery of Linear Modulations

1. Introduction

Nondata-aided (blind) feedforward timing recovery schemes [10]- [15] enable fast and reliable synchronization, and therefore, they have found use in burst transmission systems. A general cyclostationary framework that exploits second-order nonlinearities to design digital blind feedforward synchronizers was proposed in [13].

For systems with large excess bandwidth, the performance of the synchronizers that exploit the spectral line generated by a nonlinearity is asymptotically (large sample) very close to the Cramer-Rao bound. If the excess bandwidth is small, significant jitter is induced by data pattern which degrades the performance of the timing recovery scheme in mid and high SNRs [16].

Franks and Bubrouski found that the analog second-order nonlinearity based timing synchronizer can be jitter-free if an appropriate prefilter is used [38]. Reference [39] extended Franks and Bubrouski result to analog synchronizers that assume arbitrary nonlinearities. For digital timing recovery, [40]- [41] exploited similar prefilters to improve the performance of Gardner's nondata aided timing recovery scheme [30]. By means of simulation results, [42] reported that a similar prefilter could be used to improve the performance of the four samples per symbol based feedforward scheme [10]. However, no rigorous theoretical analysis was conducted in [42] to justify the jitter-free timing recovery condition.

In this section, we derive a closed-form expression for the power of self-noise

present in digital blind feedforward timing estimator [15], which is a modified version of [14] and needs two samples per symbol. This rigorous derivation of the self-noise power is later exploited for designing a prefilter that ensures nearly jitter-free timing recovery scheme. The proposed analysis and design can be easily applied to feedforward timing recovery schemes that assume oversampling factors larger than or equal to three (see e.g., [10]). In essence, it is shown that if the Franks-Bubrouski condition is fulfilled, i.e., the frequency response of the equivalent pulse is symmetric with respect to half the symbol rate and has bandwidth less than symbol rate, then a nearly jitter-free digital feedforward timing recovery scheme is obtained for any oversampling factor. Finally, we find the equivalence between the digital feedforward timing estimator and the analog synchronizer can directly lead to the prefilter by utilizing the previous results in [39].

2. Signal Model and Symbol Timing Estimators

We consider the baseband representation of a linearly modulated signal transmitted through an AWGN channel. The receiver input is expressed as

$$r(t) = \sum_{l} a_l h_T(t - lT - \epsilon T) + w(t), \tag{3.1}$$

where a_l stand for zero-mean unit variance ($E|a_l|^2 = 1$) independently and identically distributed (i.i.d) complex valued symbols with the fourth-order moment $E[|a_l|^4] = \gamma$, $h_T(t)$ is the transmitter's filter, and $w(t)$ is complex white Gaussian noise with two-sided power spectral density $N_0/2$ per component. In (1), ϵ denotes the unknown symbol timing delay (normalized by the symbol period T).

To simplify the analysis, we assume that the frequency offset has been compensated before the timing recovery task is performed (see e.g., [13] for such frequency compensation schemes). Since the proposed timing delay estimator is insensitive to

carrier phase offsets, we also omit the presence of carrier phase offset in (3.1). After matched filtering with $h_R(T)$, the resulting signal $x(t)$ is oversampled by $T_s := T/P$, with the oversampling factor $P \geq 2$, and the received sequence is given by

$$x[n] = \sum_l a_l h_c[n - lP - \epsilon P] + v[n], \tag{3.2}$$

where $x[n] := x(nT_s)$, $v[n] := w(t) \otimes h_R(t)|_{t=nT_s}$, $h_c[n] := h_c(nT_s)$, $h_c(t) := h_T(t - \epsilon T) \otimes h_R(t)$, and $\otimes$ denotes the convolution operator. We assume that $h_c(t)$ is a raised cosine (RC) pulse of bandwidth $[-(1+\rho)/2T, (1+\rho)/2T]$, with the roll-off factor ρ $(0 < \rho < 1)$ and its Fourier transform (FT) is denoted $H_c(F)$.

To estimate the timing offset, the second-order cyclostationary statistics of an observation vector with N symbols will be exploited. The sample cyclic correlation coefficient at cycle k and lag τ (integer) is given by

$$\hat{R}_x(k, \tau) = \frac{1}{NP} \sum_{n=0}^{NP-\tau-1} x^*[n] x[n+\tau] e^{-j2\pi kn/P}, \tag{3.3}$$

where $*$ denotes the conjugation operator. Based on (3.3), a general estimator was derived by Gini and Giannakis [13] for oversampling factors $P \geq 3$

$$\hat{\epsilon} = -\frac{1}{2\pi} \arg \left\{ \sum_{\tau=-L_g}^{L_g} \frac{1}{G(\tau)} \hat{R}_x(1, |\tau|) \right\}, \tag{3.4}$$

For any even and real $h_c(t)$, e.g., the RC pulse, $G(\tau)$ is a real and even function and defined by

$$G(\tau) := \frac{P}{T} \int_{-1/2T}^{1/2T} H_c(F - \frac{1}{2T}) H_c(F + \frac{1}{2T}) e^{j2\pi\tau TF/P} dF. \tag{3.5}$$

The upper limit L_g of summation (3.4) is fixed as the maximum lag τ that provides a non-zero value for $|G(\tau)| (\gg 0)$. In (3.4), L_g cyclic correlations $\hat{R}_x(1, \tau)$ are averaged with weighting factors $G^{-1}(\tau)$. Simulation results in [12] shows that estimator (3.4) with small L_g exhibits good performance. Thus, in this chapter we

use O&M estimator ($L_g = 0$) for $P \geq 3$. A new timing estimator using two samples per symbol was proposed by Lee in [14]. However, Lee's estimator is biased for large ρ and the authors in [15] modified Lee's estimator and obtained an unbiased estimator. Therefore, we introduce herein the following symbol timing estimators[1]

$$\hat{\epsilon} = -\frac{1}{2\pi}\arg\{\Gamma(\epsilon)\}\ , \tag{3.6}$$

$$\Gamma(\epsilon) = \begin{cases} \hat{R}_x(1;0) - j\frac{G(0)}{G(1)}\Re\{\hat{R}_x(1;1)\}, & P = 2 \\ \hat{R}_x(1;0), & P \geq 3. \end{cases}$$

The performance of the above estimators is very close to modified Cramer-Rao bound (MCRB) [1] for large roll-off factors ρ as shown in [15] and [12]. However, for small ρ, a large error floor will be caused by self-noise, a fact which can be observed next section for oversampling factors $P = 2$. Similar results can be observed for $P \geq 3$ and are not presented here for space limitation.

To reduce this self-noise, we introduce a prefilter $h_{pre}(t)$ with FT $H_{pre}(F)$. Since this chapter focuses on the compensation of self-noise, we omit the additive noise hereafter. Thus, we replace $h_c[n]$ in (2) with $h[n] := h_1(nT_s)$, where $h_1(t) := h_c(t) \otimes h_{pre}(t)$. Also, in (3.5), $H_c(F)$ is replaced with $H_1(F) := H_c(F)H_{pre}(F)$, the FT of real-valued filter $h_1(t)$, which is assumed to be an even function.

3. Nearly Jitter-Free Prefilter

At first, let us consider a special case $\epsilon = 0$. For $P = 2$, considering $\hat{R}_x(1;0)$ is real-valued, to get jitter-free estimation $\hat{\epsilon} = 0$, we need

$$\Re\{\hat{R}_x(1;1)\} = \frac{1}{2N}\Re\left\{\sum_l \sum_k a_l^* a_k \sum_{n=0}^{2N-2} h[n-2l]h[n+1-2k](-1)^n\right\} \tag{3.7}$$

[1]Notations $\Re\{\cdot\}$ and $\Im\{\cdot\}$ denote the real and imaginary part, respectively.

to be zero. This can be obtained if we let $h[n-2l]h[n+1-2k]=0$, or equivalently the product of two consecutive samples is zero. Since $h[2n]=h_1(nT)$ is the data strobe with unit amplitude, it follows that

$$\begin{aligned} h[2n+1] &= h_1(nT+T/2) \\ &= \int_{-1/T}^{1/T} H_1(F)e^{j2\pi FT(n+1/2)}dF \\ &= \int_{0}^{1/T} [H_1(F)-H_1(F-1/T)]e^{j2\pi FT(n+1/2)}dF \end{aligned} \tag{3.8}$$

should be zero for any n, which results in

$$H_1(F)=H_1(F-1/T)\ ,\ F\in(0,1/T)\ . \tag{3.9}$$

Considering $H_1(F)$ is an even function, we find that, for $F>0$, $H_1(F)$ should be symmetric around $1/2T$ (or $-1/2T$, for $F<0$) and with bandwidth less than $1/T$. For RC pulse, the above result leads to the prefilter

$$h_{pre}(t)=h_c(t)\cos(2\pi t/T)\ . \tag{3.10}$$

Actually, (3.8) was also used in [40] to derive the prefilter for Gardner's feedback scheme [30].

Motivated by this special result, we want to check if the above prefilter has removed the self-noise of estimator (3.6) for general cases ($\epsilon\neq 0$). However, for non-zero timing offset case, the above analysis can not verify the estimator with the prefilter (3.10) is jitter-free. Then we resort to calculate the mean-square error (MSE) of the estimators in closed form. For simplicity, we will keep to the self-noise calculation for $P=2$.

The estimation error of (3.6) can be expressed as

$$\hat{\epsilon}-\epsilon=-\frac{1}{2\pi}\arg\{\Gamma(\epsilon)e^{j2\pi\epsilon}\}\ . \tag{3.11}$$

Taking the tan-function of both sides of (3.11), we obtain

$$\tan[2\pi(\hat{\epsilon}-\epsilon)] = -\frac{\Im\{\Gamma(\epsilon)e^{j2\pi\epsilon}\}}{\Re\{\Gamma(\epsilon)e^{j2\pi\epsilon}\}} \approx 2\pi(\hat{\epsilon}-\epsilon)\ , \tag{3.12}$$

where the last approximation holds whenever the estimation error is small since $\tan(x) \approx x$ for $|x| << 1$. Therefore, we can express the square of estimation error

$$4\pi^2(\hat{\epsilon}-\epsilon)^2 \approx \frac{\Im^2\{\Gamma(\epsilon)e^{j2\pi\epsilon}\}}{\Re^2\{\Gamma(\epsilon)e^{j2\pi\epsilon}\}} = \frac{Q_{ss}}{I_{ss}}, \tag{3.13}$$

where $I_{ss} := \Re^2\{\Gamma(\epsilon)e^{j2\pi\epsilon}\}$ and $Q_{ss} := \Im^2\{\Gamma(\epsilon)e^{j2\pi\epsilon}\}$ represent the in-phase and quadrature components of the self-noise, respectively.

The calculation of $E[Q_{ss}]$ and $E[I_{ss}]$ for $P = 2$ are calculated in Appendix-A. Since the first term of $E[I_{ss}]$, $N^2[G(1)G(0)]^2$, is much larger than other terms present in $E[I_{ss}]$ and $E[Q_{ss}]$, we can make the following approximation

$$E[4\pi^2(\hat{\epsilon}-\epsilon)^2] \approx \frac{E[Q_{ss}]}{E[I_{ss}]} \approx \frac{E[Q_{ss}]}{N^2[G(1)G(0)]^2}\ . \tag{3.14}$$

With the prefilter (3.10), after some more lengthy algebra (omitted here for simplicity), $E[Q_{ss}]$ can be further written by

$$E[Q_{ss}] = \sin^2(4\pi\epsilon)\int_{-1/2T}^{1/2T}\left[(\gamma-2)\frac{8}{T^3}Q_1(V)+\frac{4}{T^4}Q_2(V)\right]\frac{\sin^2(\pi NVT)}{\pi^2V^2}dV \tag{3.15}$$

where

$$\begin{aligned} Q_1(V) = &\int_{-1/2T}^{1/2T}\int_{-1/2T}^{1/2T} H_2(F_1,V)H_2(F_2,-V) \\ &\cdot[G^2(0)+G^2(1)-2G(0)G(1)\cos(\pi F_1 T)]dF_1dF_2, \end{aligned} \tag{3.16}$$

$$Q_2(V) = \int_{-1/2T}^{1/2T}\left[G^2(0)+G^2(1)-2G(0)G(1)\cos(\pi FT)\right]H_2^2(F,V)dF\ . \tag{3.17}$$

and $H_2(F,V) := H_1(F-\frac{1}{2T}-V)H_1(F+\frac{1}{2T})$.

To check whether we have removed the self-noise, we evaluate numerically the

terms involved in (3.16)- (3.17). In Fig. 15, we plot the ratios $G_m(1,0)/G_m(0,0),\ m = 1,\ 2$, for different roll-off factors ρ, where

$$\begin{aligned} G_m(0,V) &:= \int_{-1/2T}^{1/2T} H_2^m(F,V)dF\ , \\ G_m(1,V) &:= \int_{-1/2T}^{1/2T} H_2^m(F,V)\cos(\pi FT)dF\ . \end{aligned} \tag{3.18}$$

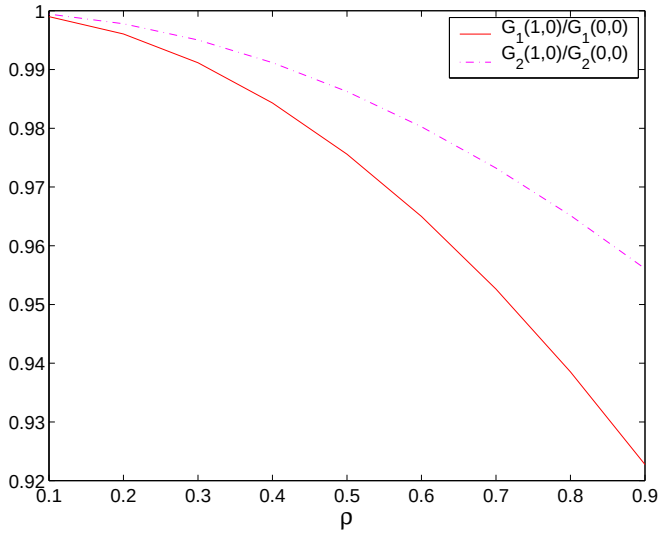

Fig. 15. Plots of $G_m(1,0)/G_m(0,0)$ for $m = 1, 2$ versus various roll-off factors ρ.

Fig. 15 shows that $G_m(1,0)/G_m(0,0)$ is very close to 1, especially for small ρ. Recalling that $G_1(1,0) = G(1)$ and $G_1(0,0) = G(0)$, we can approximate $G(1) \approx G(0)$. Thus, we can approximate (3.16)-(3.17) by

$$Q_1(V) \approx 2G^2(0)G_1(0,-V)[G_1(0,V) - G_1(1,V)], \tag{3.19}$$

$$Q_2(V) \approx 2G^2(0)[G_2(0,V) - G_2(1,V)]\ . \tag{3.20}$$

Similarly, we can also approximate $G_m(1,V)/\ G_m(0,V) \approx 1$ for small V. Note that for large V, $\sin^2(\pi NVT)/(\pi^2V^2) \approx 0$, we can approximate $Q_1(V) \approx 0$ and $Q_2(V) \approx 0$ in (3.15). Thus, we obtain $E[Q_{ss}] \approx 0$, which means that we can reduce

the self-noise with the prefilter defined in (3.10).

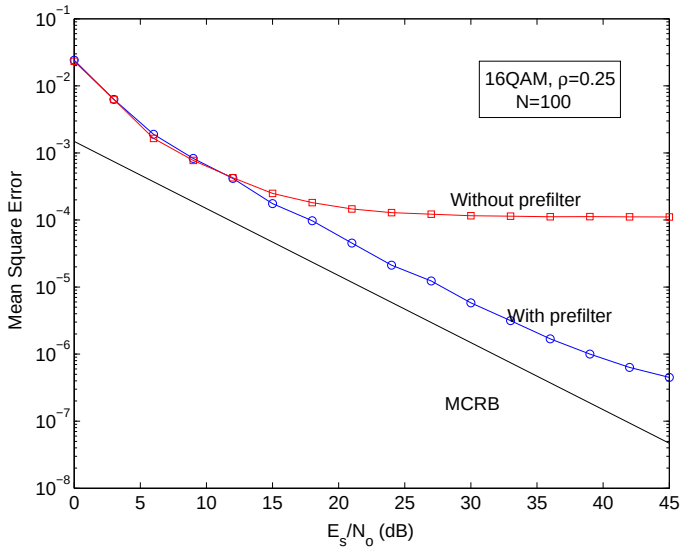

Fig. 16. Comparison of symbol timing estimators for $P = 2$.

To verify this result, we compare the performance of estimators with and without prefilter for systems with low roll-off factors ($\rho = 0.25$) by simulations in Fig. 16. For each SNR value, we average the performance of $1,000$ Monte-Carlo runs over different timing offsets. At mid and high SNRs where the performance is dominated by the self-noise, no obvious error floor is observed for SNR less than 35dB for the estimator with prefilter and its performance is closer to the MCRB. At low SNRs where the additive noise is dominant, the prefilter does not degrade the performance since the same excess bandwidth is preserved. In Fig. 17, we also compare the performance of estimator with prefilter for different N. Except for very high SNR, there is still no error floor for short observation interval N=24, which verifies that nearly jitter-free timing recovery can be obtained by prefilter..

The above analysis can be easily extended to O&M estimator. By calculating self-noise in (3.6) for ($P \geq 3$), we find the same filter as (3.10) can be used to remove

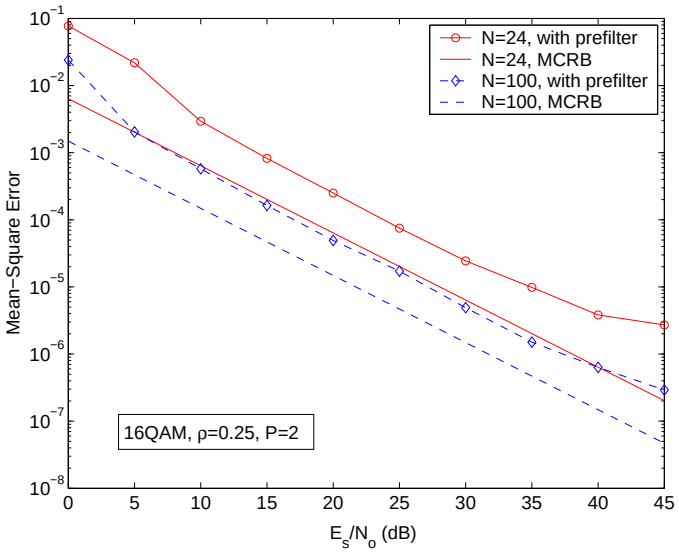

Fig. 17. Comparison of the performance of estimator for different N.

the self-noise for O&M estimator, and this theoretical result can be used to justify the simulation results in [42]. Also, we find that this prefilter brings a new explanation for (3.4). If we replace $h_{pre}(t)$ by an equivalent FIR $h_{pre}[n]$ of L_P+1 taps and assume $\hat{R}_x(1,|\tau|)$ are related to the samples at the input of the prefilter, the timing estimator (3.6) for $P \geq 3$ can be viewed as

$$\hat{\epsilon} = -\frac{1}{2\pi}\arg\left[\sum_{\tau=-L_P}^{L_P} r_{h_{pre}}[\tau]\hat{R}_x(1,|\tau|)\right], \tag{3.21}$$

where $r_{h_{pre}}[\tau] := \sum_{\tau_1=|\tau|}^{L_P+|\tau|} h_{pre}[\tau_1]h^*_{pre}[\tau_1-|\tau|]$ can be viewed as the autocorrelation coefficient at lag τ of the impulse response of the prefilter. Thus, to remove the self-noise, the $2L_p+1$ cyclic correlations in (3.4) should be averaged with weighting factors that depend on the prefilter's autocorrelation coefficients.

We remark that in frequency-selective channel the symmetry of $H_1(F)$ can not be obtained unless the channel is perfectly known. Thus, jitter free timing recovery cannot be obtained by simple prefiltering in this channel.

4. Summary

We have derived a closed-form expression for the power of self-noise for a blind feedforward symbol timing estimators that assume oversampling factors equal to 2. It has been shown that an appropriate prefilter after the receiver's matched filter can be utilized to reduce the jitter. This result can be easily extended for estimators with higher ($P \geq 3$) oversampling factors. Simulation results prove that the synchronizer which assumes such a prefilter is nearly jitter-free even in the presence of a finite (reduced) number of samples as long as linear-modulated signals are assumed. Such prefilters actually can improve performance of square-law estimators for MSK and GMSK-type signals, a topic which will be researched in the next section.

B. Jitter-Free Prefilter for Feedforward Timing Recovery of GMSK Modulations

1. Introduction

According to Laurent's approximation [43], minimum-shift keying (MSK)-type signals can be viewed as a superposition of some linearly modulated waveforms. Based on this interpretation, several blind feedforward timing estimators, similar in structure to the schemes proposed for linear modulations [10]- [15], were proposed for MSK/Gaussian MSK (GMSK) modulations in [44]- [47]. At low signal-to-noise ratios (SNRs), the estimators [46]- [47] approach the Cramer-Rao bound (CRB) and outperform the timing recovery schemes [44]- [45]. By exploiting jointly the information contained in the in-phase and quadrature components of the received signal, a novel timing recovery algorithm with improved performance relative to the timing estimator [46] is proposed. Unfortunately, due to self-noise (jitter), the performance of timing recovery schemes [46] and [47] for GMSK modulations is far from CRB at mid and high SNRs. Motivated by the fact that prefilter based structures can improve the performance of

feedforward timing estimators for linear modulations (see [48] and the references cited therein), this chapter proposes a similar prefilter to reduce the self-noise of timing recovery schemes [46]- [47]. Computer simulations show that the proposed prefilter based timing recovery schemes exhibit improved performance at mid and high SNRs with respect to the existing schemes [46]- [47].

2. Signal Model and Estimators

According to Laurent's approximation [43], an MSK-type signal can be approximated by

$$s(t) \approx \sum_{l} \exp\left[j\frac{\pi}{2}\sum_{i=1}^{l} I_i\right] h_T(t - lT) \ , \tag{3.22}$$

where

$$h_T(t) := \prod_{i=0}^{L-1} p(t + iT) \ , \tag{3.23}$$

$$p(t) := \begin{cases} \sin[\pi q(t)], & 0 \le t \le LT \\ p(2LT - t), & LT < t \le 2LT \\ 0, & \text{otherwise.} \end{cases} \tag{3.24}$$

In (3.22)-(3.24), T denotes the symbol period, I_l stands for the zero mean and independently and identically distributed (i.i.d) binary information sequence and $q(t)$ is the phase response of the modulator, supposed of length L. If the signal $s(t)$ is assumed to be transmitted through an AWGN channel, after carrier frequency and phase offset compensation, the receiver output can be expressed as

$$r(t) = s(t - \epsilon T) + w(t), \tag{3.25}$$

where $w(t)$ stands for complex white Gaussian noise with two-sided power spectral density $N_0/2$ and ϵT denotes the unknown symbol timing delay. Since the MSK-

type signal can be viewed as a linearly modulated signal with pulse shaping filter $h_T(t)$, the received signal is processed through the matched filter $h_R(t) := h_T(-t)$ and oversampled with the sampling period $T_s = T/P$ ($P \geq 3$). Consequently, the received sequence can be expressed as

$$x(n) = \sum_l a_l h(n - lP - \epsilon P) + v(n) \ , \tag{3.26}$$

where $a_l \in \{\pm j\}$ for odd l, $a_l \in \{\pm 1\}$ for even l, $v(n) := w(t) \otimes h_R(t)|_{t=nTs}$, $h(n) := h_T(t) \otimes h_R(t)|_{t=nTs}$, and $\otimes$ denotes the convolution operator. Also, let $H(f)$ stand for the Fourier transform (FT) of $h(n)$. After performing some approximations (accurate only for low SNRs) on the log-likelihood function, Morelli and Vitetta derived the blind feedforward timing estimator [47]

$$\hat{\epsilon} := -\frac{1}{2\pi} \arg \left\{ \sum_{\tau=0}^{P-1} |R(\tau)|^2 e^{-j2\pi\tau/P} \right\}, \tag{3.27}$$

where $R(\tau)$ is obtained by an operation of squaring the observation vector of length L_0:

$$R(\tau) = \sum_{n=0}^{L_0-1} (-1)^{n+1} x^2(nP + \tau) \ , \tag{3.28}$$

and the modulating factor $(-1)^{n+1}$ is used to remove the time-varying effects introduced by the data modulation. The above estimator is very similar to the digital timing recovery algorithm proposed for linear modulations in [10].

A feedforward clock recovery configuration is shown in Fig. 18. The estimated value $\hat{\epsilon}$ is post-processed by a lowpass filter with saw-tooth nonlinearity [10] to control the interpolator. The prefilter $h_{pre}(n)$ will be later introduced to improve the performance of timing estimator by reducing its self-noise.

Note that (3.26) can be rewritten as

$$x(n) = \sum_l b_{2l} h(n - 2lP - \epsilon_I P) + j \sum_l b_{2l+1} h(n - 2lP - \epsilon_Q P) + v(n) \ , \tag{3.29}$$

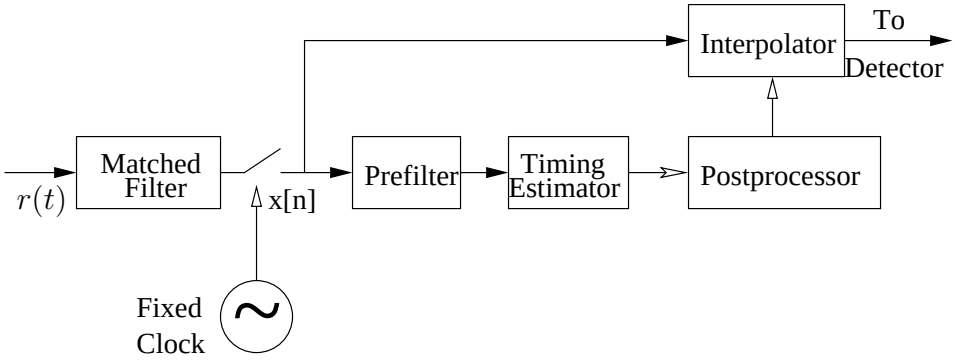

Fig. 18. Feedforward clock recovery scheme.

where $b_l \in \{\pm 1\}$, $\epsilon_I = \epsilon$ and $\epsilon_Q = \epsilon + 1$. Thus, an MSK-type signal can be viewed as an offset QPSK (OQPSK) modulated signal and both in-phase (I) and quadrature (Q) components of (3.29) are cyclostationary with period $2P$. Following the steps in [13], the cyclic correlations of the real and imaginary components of $x(n)$ are found to be

$$\begin{aligned} \sum_n \{\Re[x(n)]\}^2 e^{-j2\pi n/2P} &\propto e^{-j\pi\epsilon_I} , \\ \sum_n \{\Im[x(n)]\}^2 e^{-j2\pi n/2P} &\propto e^{-j\pi\epsilon_Q} , \end{aligned} \tag{3.30}$$

where $\Re[x]$ and $\Im[x]$ denote the real and imaginary parts of the complex-valued number x, respectively. In [46], estimates of the timing delay are obtained by exploiting separately the in-phase (I) and quadrature (Q) components of the received signal, and are given by

$$\begin{aligned} \hat{\epsilon}_I &= -\frac{1}{\pi}\arg\left\{\sum_{n=0}^{L_0P-1} \{\Re[x(n)]\}^2 e^{-j2\pi n/2P}\right\} , \\ \hat{\epsilon}_Q &= -\frac{1}{\pi}\arg\left\{\sum_{n=0}^{L_0P-1} \{\Im[x(n)]\}^2 e^{-j2\pi n/2P}\right\} . \end{aligned} \tag{3.31}$$

Estimator [46] exploits separately these estimates to obtain an estimate of the timing

delay ϵ. However, we notice that if both I and Q components are jointly exploited to estimate ϵ, the performance of [46] can be further improved. Taking (3.30) into account, this new estimator takes the form:

$$\begin{aligned}\hat{\epsilon} &:= -\frac{1}{\pi}\arg\left\{\sum_{n=0}^{L_0P-1}\{\Re[x(n)]\}^2 e^{-j2\pi n/2P} + e^{j\pi}\cdot\sum_{n=0}^{L_0P-1}\{\Im[x(n)]\}^2 e^{-j2\pi n/2P}\right\}, \\ &= -\frac{1}{\pi}\arg\left\{\sum_{n=0}^{L_0P-1}\Re[x^2(n)]e^{-j\pi n/P}\right\}. \end{aligned} \tag{3.32}$$

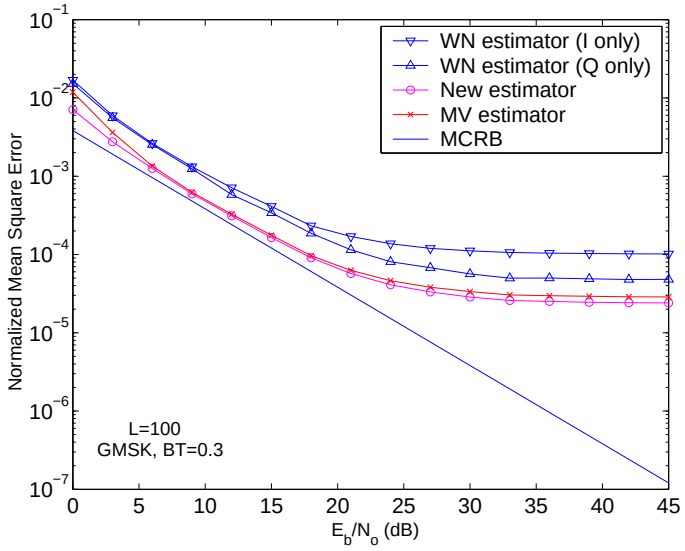

Fig. 19. Performance comparisons of various estimators for GMSK modulations.

In Fig. 19, computer simulations illustrate the performance of the above mentioned estimators for GMSK modulations. The performance of the new estimator (3.32) is always better than that corresponding to the estimator that relies only on either the I or Q-component [46]. If no phase offset is assumed, the performance of (3.32) is even slightly better than than that exhibited by the Morelli and Vitetta (MV) estimator. Unfortunately, (3.32) is sensitive to residual phase offsets while the MV estimator works well for large phase offsets. Because the prefilter to be discussed

in next section provides more improvement for GMSK modulations rather than for MSK modulations, in what follows we will focus only on designing prefilter based timing estimators for GMSK modulations.

3. Self-Noise Compensating Prefilter

At low SNRs, the performance of MV estimator is very close to CRB since it is an approximate ML estimator at low SNRs. However, the MV estimator is not necessarily good at medium and high SNRs since its approximation is not accurate anymore. It is known that the self-noise dominates the performance of such estimators at high SNRs. The simulation results presented in Fig. 19 show that for GMSK modulations the performance of the MV estimator is far away from CRB at high SNRs, which indicates that large self-noise exists in (3.27).

For linear modulations, some prefilters have been found to reduce the self-noise in analog synchronizers [38] as well as in digital synchronizers [40] and [48] that exploit second-order nonlinearities. Since the MV estimator is very similar to the second-order nonlinearity based timing recovery algorithm [10] [2], we expect that a properly designed prefilter can also reduce the self-noise of both the MV estimator and the new estimator (3.32), which is also similar in structure to [10].

Both estimators (3.27) and (3.32) exploit two key facts: an MSK-type signal is equivalent to an OQPSK modulation, and the symbol period of the I and Q components of an MSK-type signal is $2T$. Therefore, we find that the excess bandwidth of MSK-type signals is the part of signal bandwidth larger than $1/4T$ instead of $1/2T$ (which holds for linear modulations). Thus, to reduce the self-noise, we introduce

[2] The only difference is that for removing the effect of possible phase offsets in (3.27), the absolute value of $R(\tau)$ is computed before evaluating the complex Fourier coefficients.

a prefilter similar in structure to the one proposed in [48] for feedforward timing recovery in linear modulations

$$h_{pre}(n) := \cos(\pi n/P)h(n) \; . \tag{3.33}$$

In the frequency domain, (3.33) is just the shifted version (shifted by $1/2T$) of $h(n)$ such that the FT of $h_{pre}(n) \otimes h(n)$, $H_{pre}(f) \cdot H(f)$, is almost[3] symmetrical around $1/4T$.

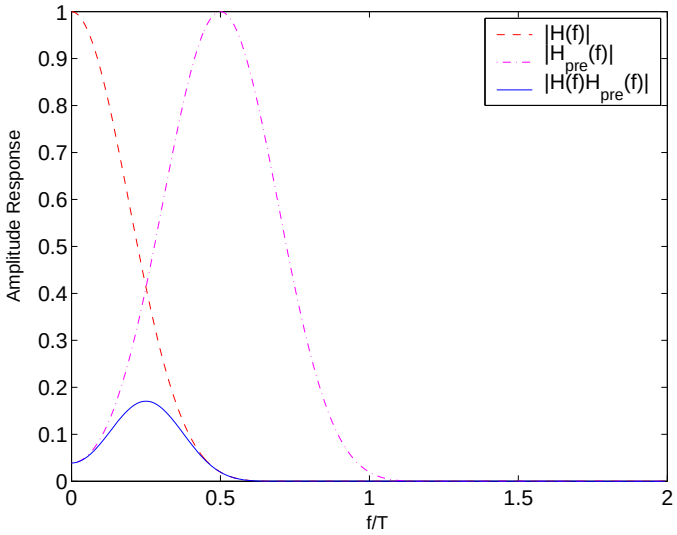

Fig. 20. Amplitude response of filters.

This prefilter is shown in Fig. 20 for GMSK modulations. This prefilter is expected to reduce the self-noise of timing recovery estimators. Similar results have been reported and analytically proven in [48] for linear modulations. To investigate the performance of prefilter based timing recovery estimators, simulation results for GMSK modulations with pre-modulator bandwidth $BT = 0.3$ are illustrated in

[3]To maintain $H_{pre}(f) \cdot H(f)$ strictly symmetrical around $\frac{1}{T}$, an additional bandpass filter may be required. However, for GMSK, we find that (3.33) is sufficient to obtain the desired symmetry.

Fig. 21. The observation length is 100 and the oversampling factor is $P = 4$. All simulation results are obtained by performing 2,000 Monte-Carlo trials averaged over different timing offsets for each SNR value. Also, the modified CRB (MCRB) [1] is plotted.

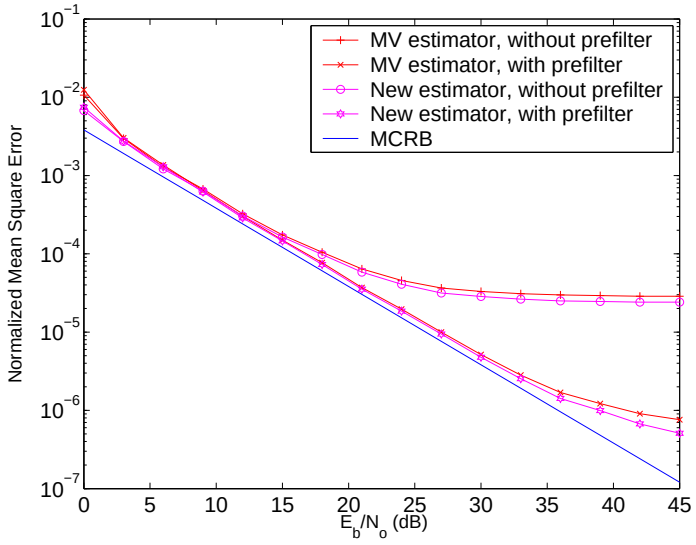

Fig. 21. The performance of estimators with and without prefilter.

$$\mathrm{MCRB}(\epsilon) = \frac{1}{2\pi^2 \cdot L_0 \cdot E_b/N_o \cdot \int_{-\infty}^{\infty} T g^2(t) dt} \,, \tag{3.34}$$

where $g(t)$ is the frequency response of modulator. The simulation results indicate that the proposed prefilter improves significantly the performance of the MV estimator and the new estimator (3.32) for SNR values equal to and larger than 15 dB, while at low SNRs their performance is almost the same. Also, the proposed prefilter can work for MSK modulations (a result that is not detailed herein). Since the excess bandwidth of GMSK modulations is much smaller than that corresponding to MSK modulations, much more significant self-noise is induced in (3.27) and (3.32). Therefore, the usage of self-noise compensating prefilters leads to larger performance

improvement for GMSK modulations. We notice further that there is still an error floor at very high SNRs, a fact which can be explained by the Laurent approximation error in (3.22) and the approximation made in [48] when deriving the expression of self-noise. As a side observation, we remark that the above mentioned improvement is obtained by increasing the complexity of the receiver since an additional prefilter besides the matched filter $H_R(t)$ is required. However, we have found that a prefilter with 20 taps is precise enough for GMSK modulations with BT=0.3.

4. Summary

A new timing estimator with improved performance relative to the Wu and Ng estimator [46] has been proposed for MSK-type modulations. The performance of this new estimator is slightly better than that of Morelli and Vitetta estimator [47]. However, both estimators are sensitive to phase offset errors. We have also derived a new digital prefilter to reduce the self-noise for both the MV estimator [47] and the WN estimator [46], a result which represents an extension of [48]. Simulation results assessed in AWGN channels show that the estimators with the proposed prefilter are very close to CRB for practical SNR. For GMSK modulations with pre-modulator bandwidth of 0.3, this simple prefilter improves the performance of existing timing recovery schemes for SNRs equal to or larger than 15 dB. The proposed prefilter based timing recovery estimators are almost jitter free and present slightly increased complexity.

CHAPTER IV

EFFICIENT COARSE FRAME AND CARRIER SYNCHRONIZATION FOR OFDM SYSTEMS

A. Introduction

In last two chapters, we have discussed timing recovery for single carrier modulated systems, where we assume AWGN or flat fading channel. As the system bandwidth increases, the propagation channel becomes more frequency selective. Due to its high complexity and slow convergence, the conventional equalizer (time domain) is not fit for wideband systems. Thanks to the simple frequency domain equalization, orthogonal frequency division multiplex (OFDM) systems have been adopted in wideband systems.

However, due to the sensitivity of OFDM systems to synchronization errors (especially to carrier frequency offset), reliable synchronization schemes must be designed for these systems. By exploiting the known structure of a training symbol or a cyclic prefix, several schemes have been proposed for coarse estimation of the carrier frequency offset and timing delay [18]- [26], and [49].

In [19], the training symbol contains two identical halves [+A +A], and the timing delay estimator is obtained by searching for the peak of correlation between the first and second halves of the received symbols. By comparing the phase difference between the identical parts, a coarse frequency offset estimator is also proposed. However, the correlation peak of the timing metric exhibits a plateau which causes large variance for the timing estimator [21]. Based on a training preamble having the same structure as the one used in the Schmidl-Cox's estimator [19], reference [20] showed that the performance of the MMSE (Minimum Mean-Square Error) and ML

(Maximum Likelihood) timing estimators still perform unsatisfactorily.

Similar to the signaling set-up adopted in [19], Coulson used two repeated m-sequences as a training symbol [24]- [25]. However, the proposed time synchronization algorithm is likely to fail in the presence of large carrier frequency offsets, and presents high implementation complexity due to the matched filtering. We remark that a training symbol with the same structure as the one proposed in [24] is exploited in [26] to develop reliable frequency and time acquisition schemes. However, the proposed time synchronization algorithm is also sensitive to large frequency offsets.

By adopting a structured training symbol of the form [+B +B -B -B], Bhargava *et.al.* proposed a coarse timing delay estimator that outperformed Schmidl-Cox's estimator [21]. However, reference [21] does not provide any detailed insight or analysis pertaining to the features of this estimator. Inspired by the signaling set-up proposed in [21], this chapter aims to develop reliable and reduced complexity coarse frame and carrier frequency acquisition schemes that exploit a structured training symbol of the form:

$$[\pm \mathrm{B} \ \pm \mathrm{B} \ \pm \mathrm{B} \ \pm \mathrm{B}] \,, \tag{4.1}$$

where B stands for a sequence of $N/4$ training samples with constant variance (power) (e.g., an m-sequence), and it can be generated with good approximation by using an $N/4$-point IFFT of an m-sequence. Principally, any signal with constant envelope in the time domain and a bandwidth similar to the OFDM data symbol can be used as a training symbol. It is found that among all the signaling set-ups (4.1), the training symbol:

$$[+\mathrm{B} \ + \mathrm{B} \ - \mathrm{B} \ + \mathrm{B}] \,, \tag{4.2}$$

leads to timing acquisition schemes that exhibit the best detection properties in terms of lower false detection probability and higher correct acquisition probability. In

addition, it turns out that the negative term -B present in (4.2) can be placed in any location with no loss in performance[1]. By exploiting the structured training symbol (4.2), this chapter proposes robust acquisition schemes for time delay and carrier frequency offset for OFDM systems that operate in additive white Gaussian noise (AWGN) and frequency-selective channels. The proposed time synchronizer offers more accurate estimates than the estimators [19] and [21]. It is also found that the performance of the proposed time and frequency offset estimators is nearly the same as [24]. In addition, the proposed estimator requires a reduced implementation complexity and is more robust to large frequency offsets with respect to (w.r.t) [24].

The rest of chapter is organized as follows. In Section B, we describe the signal model and introduce some modeling assumptions. In Section C, an optimum maximum likelihood (ML) estimator is derived for the continuous transmission scenario. We modify this ML estimator to a sub-optimum estimator with reduced complexity, which is shown to exhibit robust performance to fading channel for both burst and continuous transmission scenarios. A theoretical performance analysis study is conducted in Section D. Finally, Section E describes computer simulations that illustrate the advantages of the proposed estimator and that corroborate the theoretical performance analysis performed in Section D.

B. Signal Model

The OFDM baseband signal is generated by the IFFT-transform:

$$x(n) = \frac{1}{\sqrt{N}} \sum_{k=0}^{N-1} s_k e^{j2\pi kn/N}, \qquad -L \leq n \leq N-1 \,, \tag{4.3}$$

[1]All of them are similar to the bark code with length 4

where s_k represents the data sequence modulated on the kth subcarrier, which may assume any modulation format (such as QAM or PSK), and is independently and identically distributed (i.i.d.) with zero mean and variance $E\{|s_k|^2\} = \sigma_s^2$. Let N, L, and $1/T_u = 1/(NT_s)$ denote the number of subcarriers, the length of cyclic prefix (guard time), and the subcarrier spacing, respectively. Normally, the length of cyclic prefix L is selected to be not more than $N/5$, which can be interpreted as a 1-dB signal-to-noise ratio (SNR) loss introduced by the cyclic prefix [17, p. 46]. Herein, without loss of generality (w.l.o.g.) the value $L = N/8$ is adopted.

At the beginning of our study, we assume a flat fading channel model to derive the maximum likelihood estimator. Later it will be shown by computer simulations that the proposed estimator works well for frequency-selective channels, too. Assuming the sampling period $T_s = T_u/N$, the received signal samples can be expressed as:

$$r(n) = \alpha(n)x(n-\vartheta)e^{j(2\pi f_n n/N+\theta)} + w(n)\ , \tag{4.4}$$

where ϑ stands for the timing offset, $\alpha(n)$ is the channel amplitude, $f_n := f_e T_u = f_e N T_s$ is the normalized carrier frequency offset, θ denotes the phase offset, and $w(n)$ denotes the samples of a zero-mean complex white Gaussian noise random process with variance $E\{|w(n)|^2\} = \sigma_w^2$ and is assumed independent w.r.t $x(n)$. In slow-varying channels, we can assume $\alpha(n)$ to be a constant α over the duration of several OFDM symbols. The signal-to-noise ratio is represented in terms of the variable SNR:$=\alpha^2\sigma_s^2/\sigma_w^2$.

After coarse frame and carrier synchronization is achieved, the receiver discards the cyclic prefix, and the modulated symbol stream $\{s_k\}$ can be recovered by means of an FFT-operation. Due to the presence of cyclic prefix, small (fractional) time offsets ϑ in magnitude less than the interval (L) spanned by the cyclic prefix cause no ISI or interchannel interference (ICI) [49]- [50]. The time offset induces a phase offset

$\exp(-j2\pi\vartheta n/N)$ on the nth subcarrier, which can be corrected using channel estimation techniques. Therefore it is enough to estimate the start of training sequence within one sample period.

This chapter focuses on the estimation of f_n (packet detection) and ϑ. Although, α and θ are unknown to the receiver, their estimation can be avoided via differential encoding/decoding or can be obtained with channel estimation (pilot symbol based) techniques [49]- [50].

C. Maximum Likelihood Estimator

To derive the maximum likelihood estimator, we use a method similar to the one reported in [23]. First, we consider the continuous transmission scenario. Assume that the length of the observation vector R is so long that it incorporates the whole training symbol $[r(d)\cdots\ r(d+N-1)]^T$:

$$R := [r(d-p)\quad r(d-p+1)\ \cdots\ r(d)\ \cdots\ r(d+N-1)\quad r(d+N)\ \cdots\ r(d+N+q-1)]^T, \tag{4.5}$$

where $U := p+q+N$ denotes the length of the observation vector R, p and q are the length of subvectors preceding and succeeding the training symbol, respectively. Due to the repetitive structure of the training symbol, the autocorrelation function of the observation vector takes the form:

$$\Phi_{rr}(m) := E\{r(n)r^*(n+m)\} = \begin{cases} \alpha^2\sigma_s^2+\sigma_w^2, & m=0 \\ (-1)^{(t+1)}\alpha^2\sigma_s^2\beta^t, & m=tN/4;\ n\in\ \Gamma_1;\ t=1,2,3 \\ (-1)^t\alpha^2\sigma_s^2\beta^t, & m=tN/4;\ n\in\ \Gamma_2;\ t=1,2 \\ -\alpha^2\sigma_s^2\beta, & m=N/4;\ n\in\ \Gamma_3 \\ 0, & \text{otherwise}, \end{cases} \tag{4.6}$$

where α is assumed to be constant during the whole observation vector R, $\beta := \exp(-j\pi f_n/2)$ and $\Gamma_i := [r_{d+(i-1)N/4} \ \cdots \ r_{d+iN/4-1}]^T$, $i = 1, \ldots, 4$, represents the received samples corresponding to the ith part of the training symbol.

For the channel assumed in (4.4), we obtain the conditional probability density function (pdf) of the observation vector R w.r.t. $\{d, \ f_n\}$ in the form

$$f(R \mid f_n, \ d) = \frac{\exp(-R^H C^{-1} R)}{(2\pi)^U \det(C)} , \tag{4.7}$$

where $[\cdot]^H$ is the Hermitian operator and C is the autocorrelation matrix of the observation vector R. Let I_k stand for the identity matrix of dimension k. From (4.6), it follows that

$$C = \text{diag}\{\Phi_{rr}(0) I_p, \quad H_N, \quad \Phi_{rr}(0) I_q\} , \tag{4.8}$$

where H_N is the block hermitian matrix

$$H_N := (\alpha^2 \sigma_s^2 + \sigma_w^2) \begin{pmatrix} 1 & \rho\beta & -\rho\beta^2 & \rho\beta^3 \\ \rho\beta^{-1} & 1 & -\rho\beta & \rho\beta^2 \\ -\rho\beta^{-2} & -\rho\beta^{-1} & 1 & -\rho\beta \\ \rho\beta^{-3} & \rho\beta^{-2} & -\rho\beta^{-1} & 1 \end{pmatrix} \otimes I_{N/4} , \tag{4.9}$$

where $\rho := \text{SNR}/(\text{SNR} + 1)$ and $\otimes$ denotes the Kronecker product. Since C has a diagonal structure, its inverse is still diagonal:

$$C^{-1} = \text{diag}\{(1/\Phi_{rr}(0)) I_p, \quad H_N^{-1}, \quad (1/\Phi_{rr}(0)) I_q\} . \tag{4.10}$$

Exploiting the hermitian symmetry of H_N and the following property of the

Kronecker product $(A \otimes B)^{-1} = A^{-1} \otimes B^{-1}$, some calculations show that:

$$H_N^{-1} = \kappa \begin{pmatrix} 2\rho+1 & -\rho\beta & \rho\beta^2 & -\rho\beta^3 \\ -\rho\beta^{-1} & 2\rho+1 & \rho\beta & -\rho\beta^2 \\ \rho\beta^{-2} & \rho\beta^{-1} & 2\rho+1 & \rho\beta \\ -\rho\beta^{-3} & -\rho\beta^{-2} & \rho\beta^{-1} & 2\rho+1 \end{pmatrix} \otimes I_{N/4} \ , \tag{4.11}$$

where $\kappa := 1/(1+2\rho-3\rho^2)$. Substituting (4.10) and (4.11) into (4.7), after some lengthy algebraic manipulations, the pdf of R w.r.t. $\{f_n,\ d\}$ becomes

$$\begin{aligned} & f(R \mid f_n,\ d) = \frac{1}{(2\pi)^U \det(C)} \\ & \exp\left\{ \frac{-1}{(\alpha^2\sigma_s^2+\sigma_w^2)} \left[\sum_{n=d-p}^{d+N+q-1} |r(n)|^2 + 3\rho\kappa \sum_{n=d}^{d+N-1} |r(n)|^2 + 2\kappa\Re\left(\sum_{n=d}^{d+N/4-1} \right.\right. \right. \\ & [-r^*(n)r(n+N/4) + r^*(n+N/4)r(n+N/2) + r^*(n+N/2)r(n+3N/4)]\beta \\ & \left.\left.\left. +[r^*(n)r(n+N/2) - r^*(n+N/4)r(n+3N/4)]\beta^2 - r^*(n)r(n+3N/4)\beta^3 \right) \right] \right\} \end{aligned}$$

where $\det(C)$ is independent of f_n and d.

The maximum likelihood estimator for the time and carrier frequency offset is given by

$$(\hat{f}_n, \hat{d}) = \arg\max_{\bar{f}_n, \bar{d}} f(R \mid \bar{f}_n, \bar{d}) \tag{4.12}$$

where $\bar{f}_n$ and $\bar{d}$ stand for the trial values corresponding to time and frequency offset, respectively. Defining sub-vectors $R_i := [r(\bar{d}+(i-1)N/4),\ \cdots,\ r(\bar{d}+iN/4-1)]^T,\ i = 1, \ldots, 4$ and omitting the constants which are independent of f_n and d, we obtain the log-likelihood function: $\Lambda(\bar{f}_n, \bar{d})$

$$\begin{aligned} & = 3\rho \sum_{i=1}^{4} |R_i|^2 - 2\Re[\underbrace{(R_1^H R_2 - R_2^H R_3 - R_3^H R_4)}_{P_1(\bar{d})}\beta + \underbrace{(R_2^H R_4 - R_1^H R_3)}_{P_2(\bar{d})}\beta^2 + \underbrace{R_1^H R_4}_{P_3(\bar{d})}\beta^3] \\ & \geq 3\rho \sum_{i=1}^{4} |R_i|^2 - 2\Re[\ |P_1(\bar{d})\beta| + |P_2(\bar{d})\beta^2| + |P_3(\bar{d})\beta^3|\ ] \end{aligned}$$

$$= 3\rho\sum_{i=1}^{4}|R_i|^2 - 2[\underbrace{|P_1(\bar{d})| + |P_2(\bar{d})| + |P_3|(\bar{d})}_{P(\bar{d})}] \tag{4.13}$$

where $|R_i|^2 := R_i^H R_i$. In the last step of (4.13) we obtain a decoupled timing metric $\Lambda(\bar{d})$ which still depends on unknown time-varying α. Observing the first term of $\Lambda(\bar{d})$ is the power estimation of R, if we divide $\Lambda(\bar{d})$ by its first term and omit the unknown ρ, it follows a normalized time metric :

$$Q(\bar{d}) := \frac{P(\bar{d})}{\frac{3}{2}\sum_{i=1}^{4}|R_i|^2} , \tag{4.14}$$

Later we will show that the mean value of $Q(\bar{d})$ is independent of α in quasi-static channel. So we obtain a decoupled implementation of the time and frequency offset estimators for flat fading channel:

$$\hat{d} := \arg\max_{\bar{d}} Q(\bar{d}), \tag{4.15}$$

$$\hat{f}_n := \frac{2}{\pi}\arg\ P_1(\hat{d}) . \tag{4.16}$$

Let us consider the burst transmission scenario, e.g., a Time Division Duplex system. Normally, the received frame is preceded by noise only. The autocorrelation matrix C is block diagonal:

$$C = \mathrm{diag}\{\sigma_w^2 I_p, \quad H_N, \quad (\alpha^2\sigma_s^2 + \sigma_w^2)I_q\} . \tag{4.17}$$

Using techniques similar to the ones depicted previously, we can obtain a log-likelihood function which incorporates the dependency on the unknown number p noise-like terms preceding the training symbol in the observation vector R. Fortunately, as shown in Fig. 22, the timing metric of (4.14) still obtain maximum at the start of the frame. So we will use (4.15) and (4.16) both on continuous and burst transmission scenarios, although they are not rigorous results for the second case. Since the pro-

posed training symbol based fast acquisition scheme is more fit for burst mode, the following analysis will focus on burst transmission scenarios.

Defining $l := \bar{d} - d$, after some lengthy algebraic manipulations (see Appendix-B),at high SNR, we can approximate $P(l)$ as a real non-central Gaussian random variable (RV) with mean and variance

$$\mu_P := (3N/2 - 7|l|)\sigma_s^2\alpha^2 \ , \quad \sigma_P^2 := (9N - 31|l|)\sigma_s^2\sigma_w^2\alpha^2/2 \ , \tag{4.18}$$

respectively, which represent good approximations in the range $|l| \leq N/6$. We replace [2]the denominator of (4.13) by $V(l) = \frac{3}{2}\sum_{i=3}^{4}|R_i|^2$, which can be approximated as a real Gaussian RV with mean and variance (see Appendix-B)

$$\mu_V := 3N/2(\sigma_s^2\alpha^2 + \sigma_w^2) \ , \quad \sigma_V^2 := 9N\sigma_w^2(\sigma_s^2\alpha^2 + \sigma_w^2/2) \ . \tag{4.19}$$

So $V(l)$ is independent of l when $|l| \leq N/2$. Substituting (4.18) and (4.19) into (4.14), the mean of $Q(l)$ is given by

$$\mu_Q := \left(1 - \frac{14|l|}{3N}\right) \cdot \rho \approx 1 - \frac{14|l|}{3N} \quad \text{(High SNR)}, \tag{4.20}$$

which is independent of α at high SNR in quasi-static flat fading channel.

For the training symbol [+A +A], a timing metric similar to (4.19) is proposed in [24]

$$Q^{'}(l) = \frac{P^{'}(l)}{V^{'}(l)} = \frac{|R_1^H R_2 + R_3^H R_4|}{|R_1|^2 + |R_2|^2} \ , \tag{4.21}$$

and its mean value is given by $\mu_Q^{'} = (1 - 2|l|/N)\,\rho$.

Fig. 22-a depicts the expected value of the time metrics corresponding to two different OFDM signaling set-ups with 128 subcarriers each. The plots illustrate that

---

[2]One explanation for this modification is that we try to keep μ_Q as small as possible for $|l| < N/2$ to get robust packet detection.

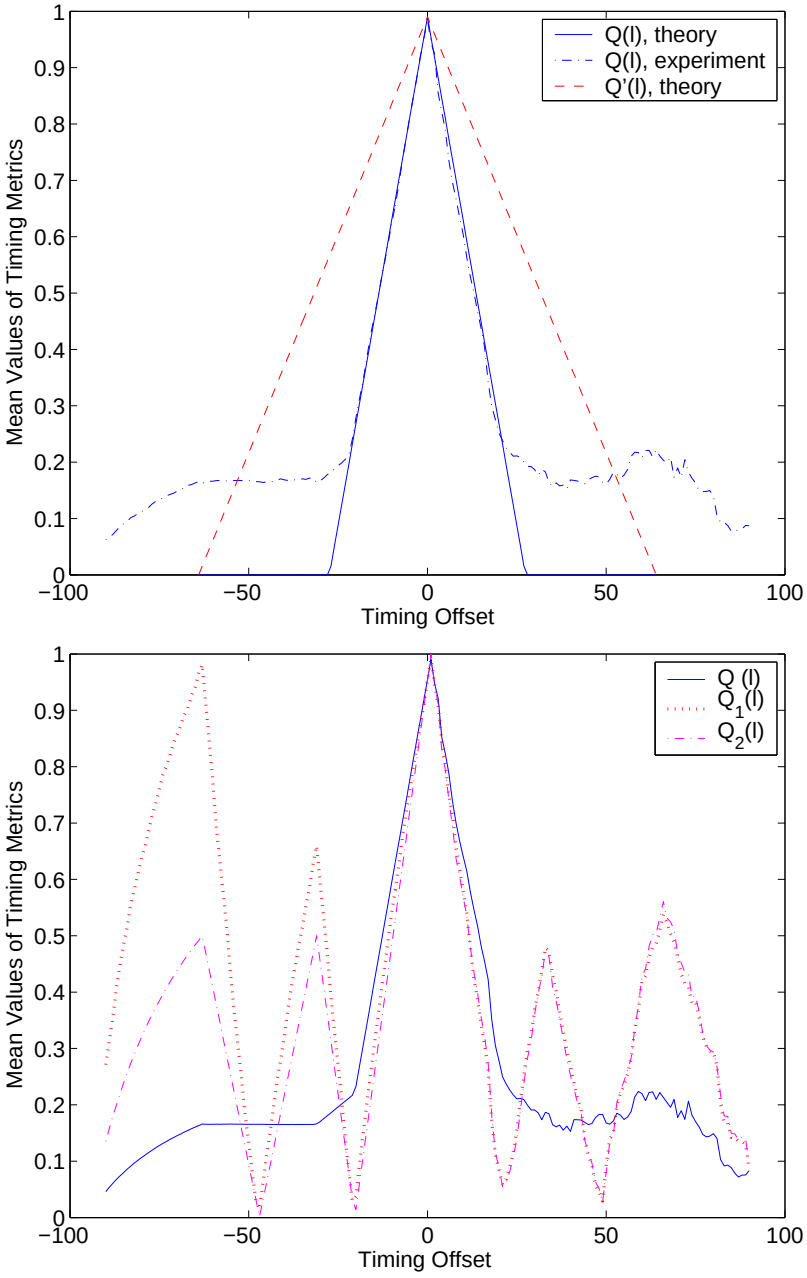

Fig. 22. Mean values of timing metrics, SNR=20dB.

the experimental value of the mean of metric $Q(l)$ is very close to the theoretical value (4.20) for $-N/6 \leq l < 0$. Actually, the approximation (4.20) holds only for $-N/6 \leq l < 0$ (see Appendix-A). However, a similar analysis can be made for $l < -N/6$, as it is shown by the experimental values depicted in Fig. 22-a. A slightly increased discrepancy between the theoretical values (4.20) and the experimental values appears whenever $l > 0$, a result which is due to the fact that the samples succeeding the training symbol contain data besides noise. Fig. 1-a shows that the timing metric corresponding to the training symbol [+B +B -B +B] has a much better localization property than that corresponding to the training symbol [+A +A]. Later on, simulation experiments will be presented to illustrate further that the proposed time acquisition scheme is robust to both ISI effects and carrier frequency offsets.

In [21], Bhargava *et al.* proposed a slightly different training symbol [+B +B -B -B]. Using the same method as before, the timing metric corresponding to the training symbol [+B +B -B -B] takes the expression:

$$Q_1(l) = \frac{|R_1^H R_2 + R_3^H R_4 - R_2^H R_3| + |R_1^H R_3 + R_2^H R_4| + |R_1^H R_4|}{3(|R_3|^2 + |R_4|^2)}. \tag{4.22}$$

By performing a similar analysis, the mean value of $Q_1(l)$ can be evaluated. In Fig. 22-b, the mean values of several timing metrics are plotted. When compared with the timing metric (4.19) corresponding to the training symbol [+B +B -B +B], the timing metric (4.22) has two undesirable peaks located in both intervals of the region $|l| > N/6$. In [21], Bhargava proposed a timing metric similar to (4.22)

$$Q_2(l) = \frac{|R_1^H R_2 + R_3^H R_4|}{0.5(\sum_{i=1}^{4} |R_i|^2)}\ , \tag{4.23}$$

which is found to present a large undesirable correlation peak as shown in Fig. 22-b, and consequently appears not to be appropriate for burst transmission scenarios. If only the last two terms in the denominator of (4.23) are considered, the following

modified timing metric is obtained:

$$Q_3(l) = \frac{|R_1^H R_2 + R_3^H R_4|}{|R_3|^2 + |R_4|^2} \ . \tag{4.24}$$

Fig. 22-b shows that the modified timing metric $Q_3(l)$ has four undesirable local peaks besides the desired correlation peak. Thus, the modified metric is less reliable than (4.22). Since the timing metrics (4.22)-(4.24) have some undesirable peaks besides the desired correlation peak, in what follows we will focus our analysis on the timing metric (4.19) corresponding to the proposed training symbol (4.2).

The implementation of the timing acquisition scheme requires searching techniques for finding the correlation peak of the timing metric. In [25], Coulson proposed a two-step based searching technique for packet detection. We adapted this two-step searching technique to fit the proposed timing metric.

Step 1: *Coarse packet detection.* A detection threshold T_c is set up to assure that the receiver can find the peak of the metric in a short range. The estimator compares $Q(l)$ with a given threshold T_c. Once $Q(l) > T_c$, the receiver obtains a coarse packet detection range Ω and proceeds with the next step.

Step 2: Fine packet detection and frequency offset estimation. In this step, the receiver searches for the local peak of $P(l)$[3] in the range Ω, and the frequency offset estimator is implemented using (4.15). The resolution of this searching step is limited to one sampling period.

Normally, the coarse estimated value l obtained in the first step is always negative (we assume w.l.o.g. that $|l| \leq \Omega$), a fact which will be corroborated in the next section. To detect the correct start ($l = 0$) of the packet, the receiver needs to search

[3] $Q(l)$ can also be used in this step and we found the searching using these two different metrics have almost the same performance in slow-varying channel. So we take $P(l)$ to simplify the analysis.

the maximum of $P(l)$ by sliding the observation window R in a continuous interval that runs from l to $l + \Omega$ and that contains the correct starting point ($l = 0$) of the frame. Fig. 23-a and 23-b depict two critical scenarios, where the right acquisition time is present at one of the extremities of the searching interval. In any case, the receiver requires a processing delay in the second step, which depends on the value Ω. Thanks to the guard time (cyclic prefix) of the succeeding OFDM symbol, as shown in the Fig. 23, if $\Omega = L$, then the correct correlation peak can be found in a search range equal to L. Fig. 23-b shows that the last location of the sliding window will not overlap with the useful part of the succeeding OFDM symbol. Thus, the second step requires a processing delay not larger than L.

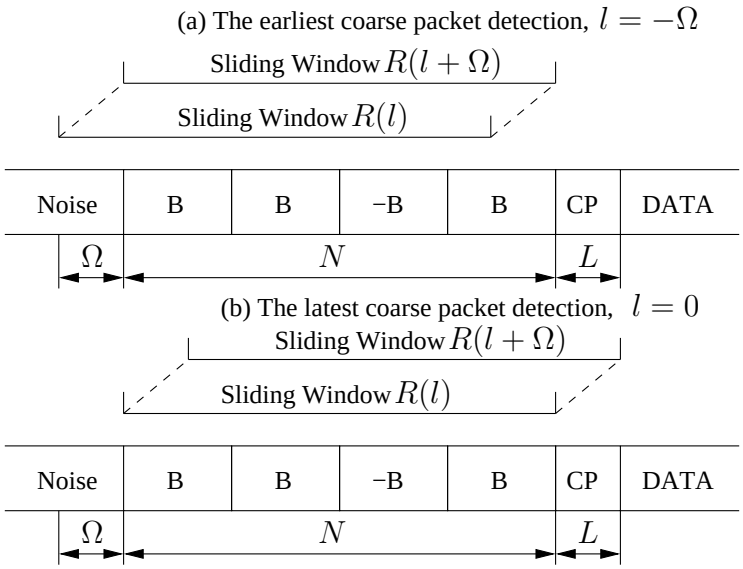

Fig. 23. Coarse packet detection and fine packet detection($\Omega = L$).

Based on the above considerations, in the first step the following condition must be satisfied for the success of fine packet detection step

$$\forall\, l < -L, \quad Q(l) < T_c \quad \text{and} \quad \exists\, l \in [-L, 0], \quad Q(l) > T_c \;, \tag{4.25}$$

which means that the coarse packet detection is obtained only in the range of $[-L+1, 0]$.

D. Theoretical Analysis of Estimators

In this section we perform a theoretical analysis of the estimators proposed in the previous section. Since most of the detected peaks are delayed several samples from the correct time in multipath environments and OFDM is tolerant to this kind of errors whenever a short cyclic postfix is present, in what follows we will limit the analysis of estimators only for lags $l \leq 0$. Since the samples succeeding the training symbol contain data besides noise, we remark that the analysis is right only for $l \leq 0$. The analysis for $l > 0$ appears intractable.

1. Coarse Packet Detection

We use the same method as in [25], and define:

$$Z(l) := P(l) - T_c V(l) \quad . \tag{4.26}$$

The receiver will declare it obtains coarse packet detection once $Z(l) > 0$. Since both $P(l)$ and $V(l)$ can be approximated as real Gaussian RV for high SNR, it follows that

$$p_{1r} := \text{prob}(Z(l) > 0) = \frac{1}{2}\text{erfc}\left(-\frac{\mu_Z}{\sqrt{2}\sigma_Z}\right) \quad , \tag{4.27}$$

where

$$\mu_Z := \mu_P - T_c\mu_V \ , \quad \sigma_Z^2 := \sigma_P^2 + T_c^2\sigma_V^2 - 2T_c\text{cov}\{P, V\} \ . \tag{4.28}$$

From Fig. 24 we infer that (4.25) can be satisfied with probability asymptotically approaching to 1.0 when $T_c = 0.6$ and SNR$>$ 10 dB. As for [+A +A], there is no threshold value to get robust (high probability) coarse packet detection in the range

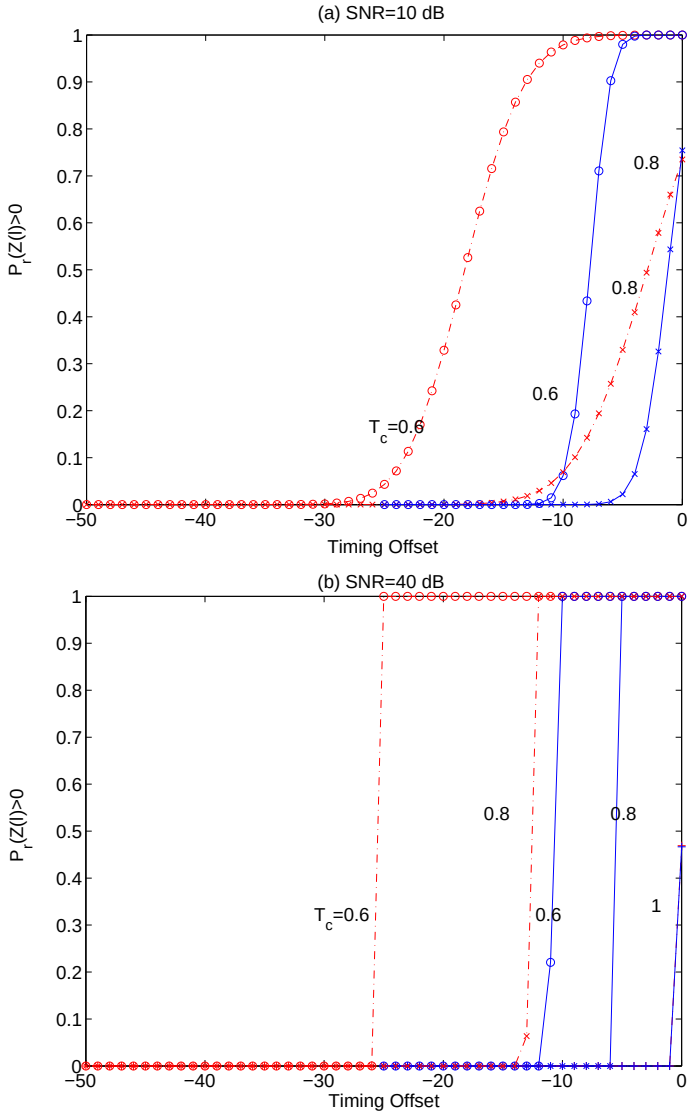

Fig. 24. Probability of $Z(l) > 0$ for (a) $E_s/N_0 = 10$dB, (b) $E_s/N_0 = 40$dB. The solid and the dash lines are associated with the metrics of [+B +B -B +B] and [+A +A], respectively.

$-L \leq l \leq 0$. An longer cyclic prefix length L, e.g., $L = N/4$, can increase the probability of coarse packet detection, but at the same time the system throughout is reduced.

In the absence of signal, the product of two noise vectors can not be omitted like the approximation performed in Appendix-B. From [24], according to the Central Limit Theorem (CLT), $P_1(l)$, $P_2(l)$ and $P_3(l)$ can be approximated as three Gaussian RV with variances $\sigma_i^2 := (1 - i/4)N\sigma_w^4$, i=1,2,3, respectively. From (4.13), $P(l)$ can be viewed as the summation of three independent Rayleigh RV with the pdfs $f(x_i) = 2x_i/\sigma_i^2 \exp(-x_i^2/\sigma_i^2)$, $i = 1, 2, 3$.

$V(l)$ can be viewed as a Gaussian RV with mean $\mu_V := 3N\sigma_w^2/2$ and variance $\sigma_V^2 := 9N\sigma_w^4/2$. Since a closed-form expression for the probability of false alarm $p_{FA} :=$ prob $(|P_1(l)| + |P_2(l)| + |P_3(l)| > T_c V(l))$ can not be obtained, we resorted to numerical calculations. For $N = 128$ and $T_c = 0.6$, an extremely small value is obtained $p_{FA} = 1.38e - 9$. Increasing the threshold T_c and training symbol length N can reduce further the probability of false alarm (see Fig. 25). It is interesting to note that an upper bound of p_{FA} may be obtained based on the inequality $p_{FA} <$ prob $(3|P_1(l)| > T_c V(l)) \approx \exp(-NT_c^2/(3 + 4T_c^2))/\sqrt{1 + 4T_c^2/3}$, which shows an exponential dependence w.r.t. N.

2. Fine Packet Detection

First, we derive the probability of a type of estimation error that takes place at the closest neighbor to the correct time location. In Appendix-C, it is shown that $\Delta := P(0) - P(-1)$ can be viewed as a real Gaussian RV with mean $\mu_\Delta = 7\sigma_s^2\alpha^2$ and variance $\sigma_\Delta^2 := (41 + 12\cos(\beta))\sigma_s^2\sigma_w^2\alpha^2 < 53\sigma_s^2\sigma_w^2\alpha^2$ The probability of $\Delta < 0$ can be

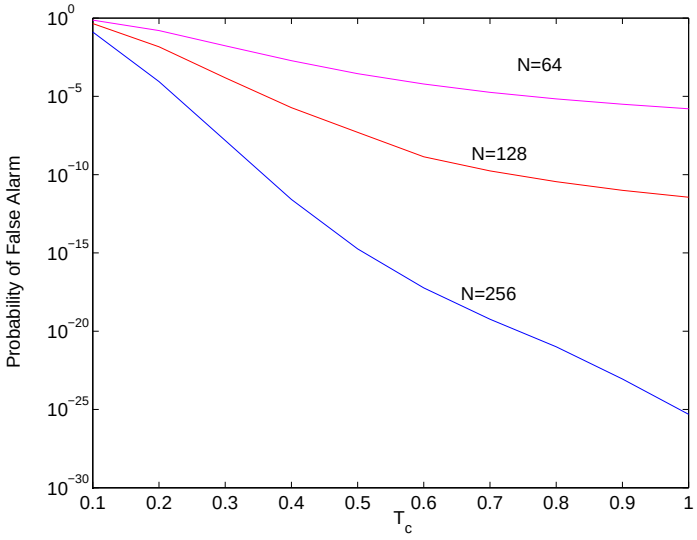

Fig. 25. The probability of false alarm versus N and T_c.

expressed as

$$p_{2r} := \text{prob}\{\Delta < 0\} = \frac{1}{2}\text{erfc}\left(\frac{\mu_\Delta}{\sqrt{2}\sigma_\Delta}\right) < \frac{1}{2}\text{erfc}\left(7\sqrt{\frac{\text{SNR}}{106}}\right) . \tag{4.29}$$

At high SNR, p_{2r} is very small, e.g., $p_{2r} < 0.0033$, at SNR= 9 dB. Thus, the detected correlation peak deviates from the correct location to the closest neighbor with small probability. Similarly, the probabilities of $P(l) > P(0)$ for $-\Omega \leq l < -1$ ($\Omega = L = N/8$) can be determined after some similar calculations and they are much smaller than p_{2r}. Thus, we can approximate the probability of fine packet detection p_{fd} by $p_{fd} \approx 1 - p_{2r}$.

As for the training symbol [+A +A], if the timing metric $P^{'}(l)$ (see (4.21)) is defined, a similar result can be obtained for the difference between the time metric corresponding to the correct time and that corresponding to its closest neighbor,

$\Delta^{'} = P^{'}(0) - P'(-1)$. Define

$$p_{3r} := \text{Prob}\{\Delta^{'} < 0\} = \frac{1}{2}\text{erfc}\left(\sqrt{\frac{\text{SNR}}{6}}\right) . \tag{4.30}$$

It follows that a higher probability for detecting a (false) peak deviating from the correct time to its neighborhood is expected for the Schmidl-Cox's estimator [19], e.g., $p_{3r} = 0.05$ when SNR= 9dB. The above analysis shows that the proposed timing metric is more robust than the timing metric corresponding to the training symbol [+A +A].

3. Carrier Frequency Offset Estimation

According to (4.15), the identifiability limit of the proposed carrier frequency offset estimator is given by $|f_n| < 2$, which is equal to twice the subcarrier spacing and is larger than that corresponding to estimators [18], [19] and [24]. If there is no timing error, the estimator (4.15) is shown (in Appendix-C) to be an unbiased estimator with mean-square error:

$$\text{MSE}[\hat{f}_n] \approx \frac{16}{9 \cdot \pi^2 \cdot N \cdot \text{SNR}} , \tag{4.31}$$

which is even smaller than the MSE of the frequency offset estimator proposed in [19]. In the presence of small timing errors $l \neq 0$ this estimator is shown (see Appendix-D) to be still unbiased and its mean-square error is given by:

$$E[(\hat{f}_n - f_n)^2] \approx \frac{16 \cdot (1 + \frac{10|l|}{N})}{9 \cdot \pi^2 \cdot N \cdot \text{SNR} \cdot (1 - \frac{4|l|}{N})^2} . \tag{4.32}$$

The MSE of the frequency offset estimator depends on the timing error, SNR and the length of training symbol. Fig. 26-b indicates that small timing offsets result in little degradation.

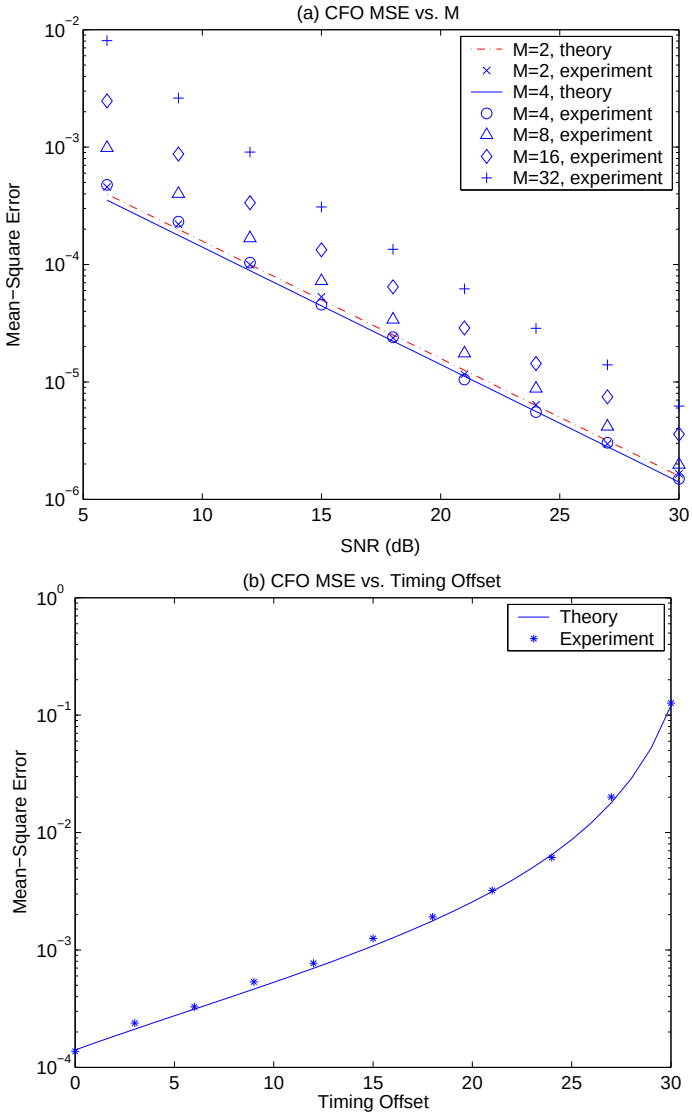

Fig. 26. MSE of carrier frequency offset estimator in AWGN channels.

Assume now the following general form of a training symbol with length N

$$[\ b_1 S_1^T\ b_2 S_2^T\ \cdots\ b_M S_M^T\ ]^T\ , \tag{4.33}$$

where $S_i = B,\ i = 1, \cdots, M$, are identical sub-vectors of length N/M, and $b_i = \pm 1$ represents a bit sign ($\pm$) associated with S_i. We observe that the signaling set-ups proposed in [19], [24], and in this chapter are special cases of (4.33) $M = 2$, $b_1 = b_2 = 1$, and $M = 4$, $b_1 = b_2 = b_4 = 1$, $b_3 = -1$, respectively.

If R_i is the observation vector corresponding to $b_i S_i$ corrupted by the AWGN vector W_i, an general estimator for f_n can be expressed as:

$$\hat{f}_n = \frac{M}{2\pi} \arg\left(\frac{\Im[\sum_{i=1}^{M-1} b_i b_{i+1} R_i^H R_{i+1}]}{\Re[\sum_{i=1}^{M-1} b_i b_{i+1} R_i^H R_{i+1}]} \right)\ , \tag{4.34}$$

which is proved to be unbiased and following general expression for the MSE of the frequency estimator holds (see Appendix C):

$$\mathrm{MSE}[\hat{f}_n] = \frac{M^3}{4 \cdot \pi^2 \cdot (M-1)^2 \cdot N \cdot \mathrm{SNR}}\ . \tag{4.35}$$

For a fixed SNR and N, the value $M = 4$ minimizes (4.35), even integers M. This result is corroborated by the set of curves depicted in Fig. 26-a. When compared with [19] and [24], the proposed estimator (4.15) achieves a similar MSE-performance but assumes a larger (twice) estimation range.

In [24], Coulson used the same coarse correlator as [19] before the matched filter to estimate and correct the fractional frequency offset $|f_n| < 1$. Unfortunately, the received samples after Coulson's coarse frequency estimator might still be affected by large frequency offsets $|f_n| > 1$, which will cause the failure of the fine packet detection step. However, we note that the proposed frequency estimator (4.15) is robust to large frequency offsets.

It is interesting that this single sliding window estimator (SSE) in (4.34) is a sub-

optimal and the simplest version of estimators used in [53] and [54]. The best linear unbiased estimator (BLUE) was derived in these two references, which obtains the minimal variance by increasing the complexity ($M/2$ sliding windows and properly weighted averaging). In Fig. 27, we compare the performance and complexity between SSE and BLUE for different M, which is proportional to frequency offset detection range. The designer can choose a tradeoff between performance, detection range and complexity. Constrained by the performance requirement (e.g., MSE less than 10^{-4}), we should use BLUE estimator to detect large frequency offset. If only small frequency offset is needed to estimate, the simple version, SSE estimator can be selected.

Different from the above estimators , a nonlinear least squares (NLS) approach was proposed in [55]. The accurate frequency offset estimation can be obtained by large points FFT grid searching which increases the complexity of estimator.

E. Numerical Analysis of Estimators

We assume a wireless OFDM system of bandwidth 5 MHz operating at 5.8 GHz, with $N = 128$ subcarriers and cyclic prefix $L = 16$. The channel is time-varying continuously with a maximum Doppler frequency of 50 Hz and has an exponentially decaying power-delay profile with 16 independent T_s-spaced Rayleigh-fading paths that are modeled in accordance with Jakes model. The root-mean square delay spread for this power-delay profile is assumed $\tau_{rms} = 1$ sample, and the maximum delay spread is 16 samples. A frequency offset $f_e = 0.8NT_s$ is assumed. A number of 2,000 Monte Carlo trials were performed for each SNR point.

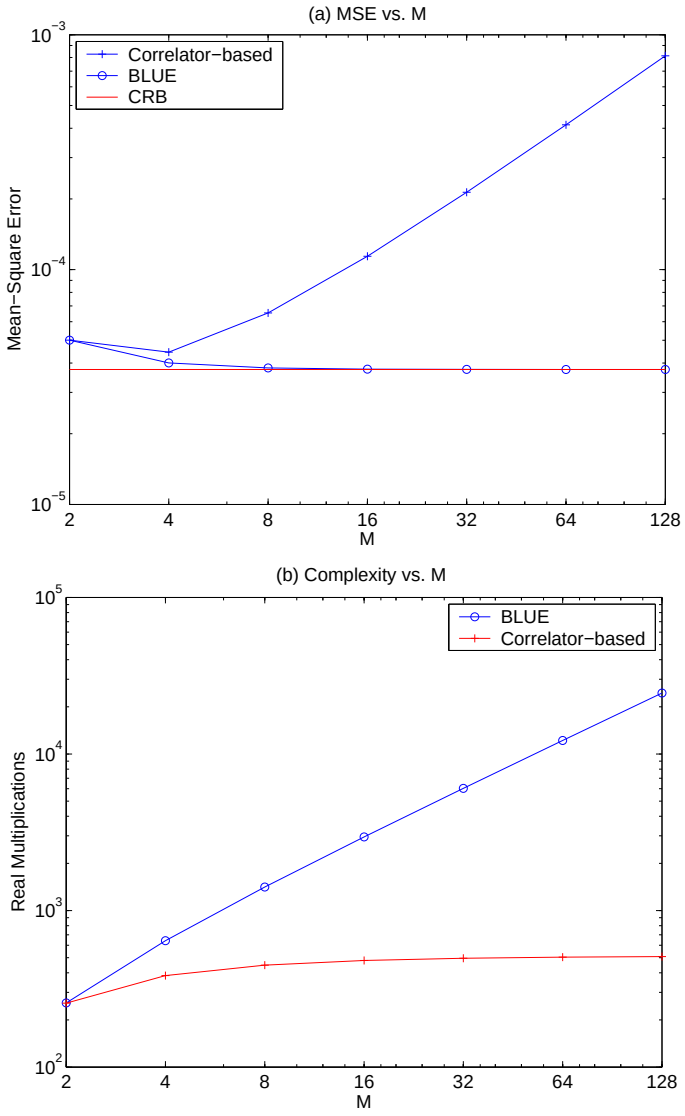

Fig. 27. Comparison of MSE and complexity of carrier frequency offset estimators in AWGN channels, SNR=15dB.

1. Performance of Algorithms

The performance of five algorithms are compared by computer simulation: (a) Schmidl-Cox method [19], (b) Modified method A, which assumes the timing metric $Q'(l)$ (4.21) and the training symbol [+A +A] (no cyclic prefix), (c) Modified method B, which assumes the timing metric (4.24), (d) Proposed method (4.19), and (e) Coulson's method [24]. We assume that methods (a)-(d) use the same searching techniques as the ones proposed in Section C.B.2. The threshold value for the coarse packet detection step is set to $T_c = 0.6$ for all five methods and SNR$\geq$ 6 dB. The second threshold value for the matched filter in [24] is set to 0.5. Because the poor localization properties of the Schmidl-Cox method and the modified method A, we extend the searching range from L to 2L during the second searching step.

At SNR=20 dB, the distributions of timing estimation errors l are shown in Fig. 28, where the path with strongest power is assumed to be the correct time. The high inaccuracy of Schmidl-Cox method (see Fig. 28-a) is caused by the cyclic prefix which causes a plateau for the timing metric [21]. In Figs. 28 b-e, most estimation errors are delayed values in the range $0 \leq l \leq 2$. The delayed errors will result in interference between adjacent symbols. In [56], a short cyclic postfix is used to mitigate ISI errors due to delayed FFT windows. Here we use a cyclic postfix with length 2 for the OFDM symbols succeeding the training symbol.

The timing errors $l > 2$ or $l < 0$ will still cause ISI, and we compare the probabilities of this kind of timing errors for all the five estimators in Fig. 29. Most timing errors of the Schmidl-Cox method induce ISI and a longer cyclic prefix for succeeding symbols is needed to decrease the ISI, which means a loss in the system throughout. Although no cyclic prefix (no plateau for timing metric) is used in the modified method A, its performance is worse than methods (c) and (d). The performance of

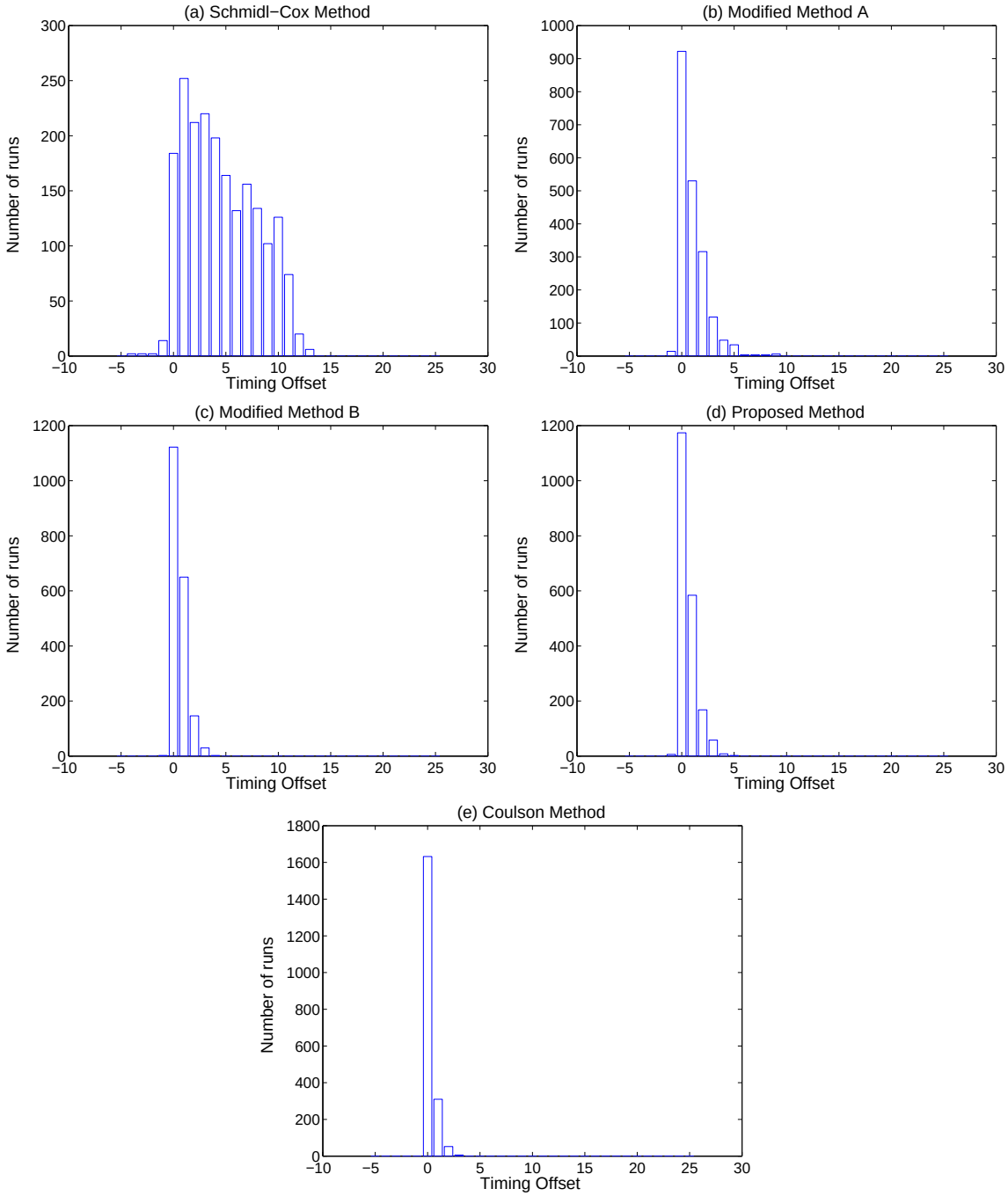

Fig. 28. Time offset estimation $\hat{l}$ in frequency-selective channels.

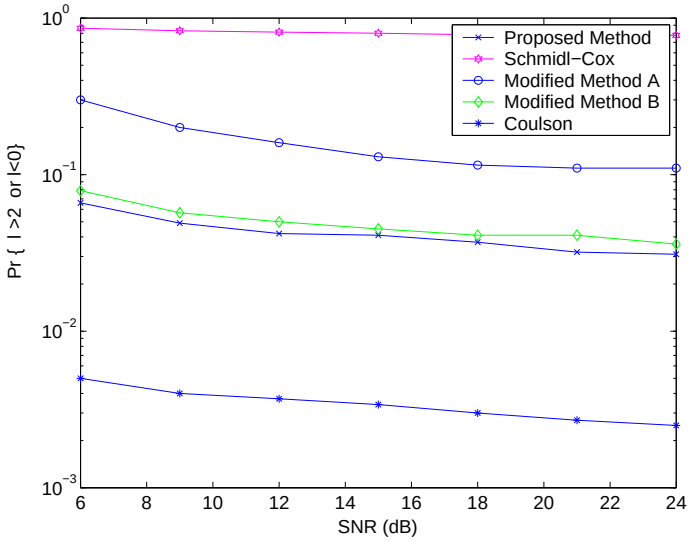

Fig. 29. The probabilities of timing errors that will cause ISI in frequency-selective channels.

method (c) is close to proposed estimator. But in our simulation, we use high quantization resolution (limited by computer) when calculating timing metrics. If a small quantization resolution (e.g., 6 bits) is used, due to its undesirable peaks beside the correct peak in Fig. 23, it can be expected that the packet detection of method (c) is much worse than that of proposed scheme. Due to the excellent autocorrelation characteristic of m-sequences, it is not surprising that Coulson's method provides the best performance with increased complexity[4]. However, Coulson's method is sensitive to large frequency offsets as discussed in [51].

Next, we compare the performance of frequency offset estimators. The same frequency offset estimator as [19] is used in the case of estimators (a) and (b). No carrier estimator was proposed in [21]. Therefore, we extend the corresponding frequency

[4]For each sample, Coulson's method needs N/2+4 complex products while the proposed scheme needs 8 complex products.

estimator here. Since (4.24) exploits only the set of statistics $R_1^H R_2$ and $R_3^H R_4$, a frequency offset estimator similar to (4.15) and which exploits only the reduced set of statistics present in (4.24) can be expressed as:

$$\hat{f}_n := \frac{2}{\pi} \arg(R_1^H R_2 + R_3^H R_4) \; . \tag{4.36}$$

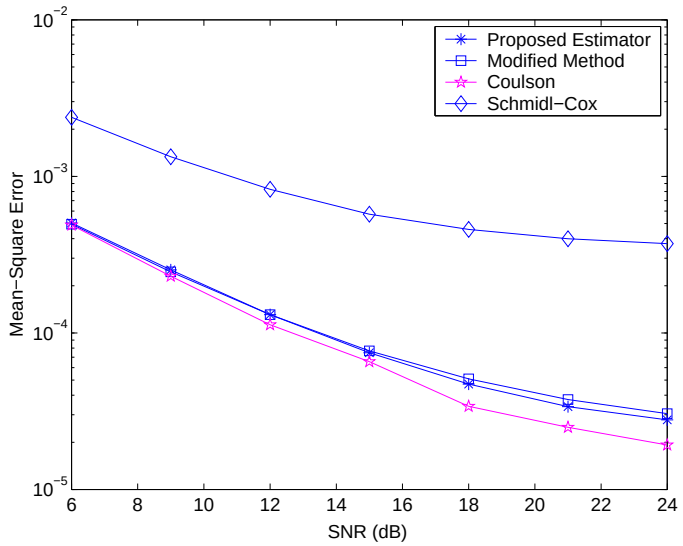

Fig. 30. MSE of the carrier frequency offset estimators in frequency-selective channels.

From Fig. 30, it is concluded that the MSE of the proposed estimator is almost the same as that of Coulson method and modified method A. However, the proposed estimator (4.15) exhibits a larger identifiability range. The larger MSE of (4.36) is due to the neglected statistics $R_2^H R_3$. Thanks to the cyclic prefix, which keeps the periodic property in slow varying multipath channel, the Schmidl-Cox method provides better performance than the other methods, especially at high SNR. According to [17], for a negligible degradation of about 0.1 dB, the maximum tolerable frequency offset is less than 1% of the subcarrier spacing, which is satisfied by all estimators (excluding the estimator (4.36)) whenever SNR$>$ 13dB. So we expect that this improvement of

frequency offset estimation obtained by using cyclic prefix in training symbol hardly can improve BER performance. Actually BER performance will be degraded due to large timing errors in Fig. 28-a and it will be verified by simulation later.

2. System Performance

In order to assess the performance of the proposed synchronization scheme, we compare the BER performance of three systems with the proposed scheme, Schmidl-Cox scheme and perfect synchronization, respectively. We use DQPSK/DBPSK modulations in frequency domain to simplify the receiver. A 1/2 rate convolutional code with 16 states, and block interleaving are utilized to correct random and burst errors caused by additive noise and frequency nulls created by deep fades.

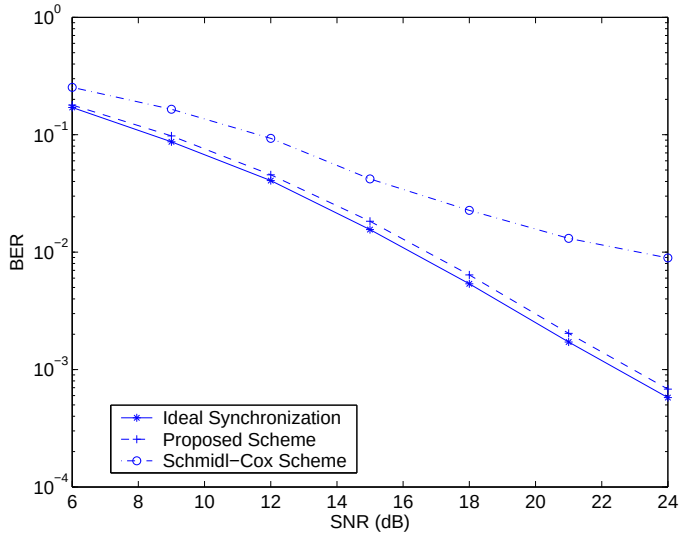

Fig. 31. BER performance versus SNR in frequency-selective channels.

From Fig. 31, compared to the system with ideal synchronization, there is a large degradation in the system with Schmidl-Cox scheme. As shown in the Fig. 28-a, the detected value l often deviate from the start of frame ($l = 0$) in dispersive channels.

The timing errors have two results and both of them bring BER degradation. At first, a phase rotation $\exp(j2\pi ln/N)$ is induced by small timing errors $l \leq 2$ and results in a constant phase difference $\exp(j2\pi l/N)$ between adjacent subcarriers. The second results and main reason for degradation is ISI induced by timing errors $l > 2$.

As for the system with the proposed scheme (dash line), the proposed estimator results in 0.3-dB degradation. The reason of this degradation is dominated by the phase rotation induced by small timing errors $l \leq 2$. So this degradation can almost be avoided by using channel estimation techniques to correct this linear phase offset between adjacent subcarriers.

F. Summary

Motivated by the need to obtain a clear assessment of Barghava's estimator [21], this chapter developed a fast and robust frame and carrier synchronization scheme for burst and continuous-mode OFDM transmissions in AWGN and ISI-channels. The proposed scheme exploits the repetitive structure of a training symbol and presents superior performance w.r.t. Schmidl-Cox approach [19] and Bhargava's method [21] in terms of better detection properties and accuracy, and extended identifiability range of the carrier estimate. When compared with Coulson's method [24], the proposed scheme presents a reduced implementation complexity, and is more robust to large carrier offsets and exhibits nearly the same performance in terms of estimation accuracy.

It should be noted that, after coarse acquisition, there could be some timing and phase error caused by residual carrier frequency offset and sampling clock frequency offset. To remove these errors, OFDM receiver needs timing and phase tracking, a topic that is to be discussed in next chapter.

CHAPTER V

DECISION-DIRECTED FINE SYNCHRONIZATION FOR OFDM SYSTEMS

A. Introduction

After coarse synchronization, there might still be a residual CFO and a sampling clock frequency offset (SFO), which will introduce time and subcarrier varying phase rotations [57]- [49] and FFT window shift.

To remove the effect of CFO and SFO, some authors proposed pilot based post-FFT synchronizers [50]- [59]. Although the estimator [50] appears to work under general channel conditions, no analytical result has been reported to assess its unbiasedness in F-S channels. Also, the alternative estimator [60] appears to be biased in F-S channels. In this chapter, we propose a new decision-directed (DD) post-FFT CFO and SFO synchronization scheme without relying on pilots. It is shown that the proposed CFO and SFO estimators are (approximately) unbiased in both AWGN as well as F-S channels. Analytical closed-form expressions of the mean-square error (MSE) of the proposed estimators are also reported for AWGN channels.

B. Signal Models

The transmitted complex baseband OFDM signal can be described by

$$s(t) = \frac{1}{\sqrt{T_u}} \sum_{l=0}^{\infty} \sum_{k=-K/2, k\neq 0}^{K/2} a_{l,k} e^{j2\pi(k/T_u)(t-T_g-lT)} g(t-lT) \ , \tag{5.1}$$

where $a_{l,k}$ denotes the complex data modulated on the $f_k = k/T_u$ subcarrier frequency of the l_{th} OFDM symbol with the unit variance, $g(t)$ is a rectangular pulse with unit amplitude during $0 \leq t < T$ and T_g is the length of cyclic prefix. A discrete-time implementation (with the sampling period $T_s = T_u/N$) of $s(t)$ is generated by means

of an N-point inverse fast Fourier transform (IFFT). In addition, K is chosen to be less than N to avoid spectrum aliasing. Therefore, the symbol period is $T = T_g + T_u$, which corresponds to $M = N + N_g$ samples.

The received signal sampled with the period T'_s, in the presence of carrier frequency offset (CFO) f_e, timing offset $n_e T'_s$ and small sampling clock frequency offset (SFO) $\epsilon = (T'_s - T_s)/T_s$, is given by

$$r(nT'_s) = e^{j2\pi f_e n T'_s} \sum_i h_i(nT'_s) s(nT'_s - \tau_i - n_e T'_s) + w(nT'_s) \ , \tag{5.2}$$

where $\{h_i(nT'_s)\}$ present the samples of channel. We assume that the channel presents normalized power $\sum_i E[|h_i(nT'_s)|^2] = 1$, and its maximum delay spread τ_{max} is less than T_g. In addition, $w(nT'_s)$ denotes complex additive white Gaussian noise with variance $\sigma_n^2 = E\{|w(nT'_s)|^2\}$. The average signal-to-noise ratio (SNR) for data subcarriers is defined as $E_s/N_o = 1/\sigma_n^2$.

After the coarse timing estimation, $\hat{n}_e$ is used by the FFT window controller. Therefore, the FFT window can be assumed to start from the ISI-free area $[\tau_{max} + 1 + lM, N_g + lM]T'_s$.

To reduce possible intercarrier interference (ICI), a coarse CFO estimate $\hat{f}_e$ is used by the frequency corrector block. The channel is assumed to be constant during an OFDM symbol duration, and its Fourier transform is given by $H_{l,k} = \sum_{n=0}^{\tau_{max}} h_{l,n} e^{-j2\pi k(n/N)}$, $h_{l,n} = h_n(lMT'_s)$.

The output of the N-point FFT block can be expressed as:

$$z_{l,k} = 1/\sqrt{N} \sum_{n=0}^{N-1} r_{l,n} e^{-j2\pi kn/N}$$

where $r_{l,n} = r((n + N_g + lM)T'_s)$. Taking into account the small SFO ϵ and residual

CFO $f_N = f_e T_u$ [49], the l_{th} symbol of the N-point FFT block takes the expression:

$$z_{l,k} \approx a_{l,k} H_{l,k} e^{j\pi\theta_k (N-1)/N} e^{j2\pi\theta_k (N_g + lM)/N} + \text{ICI} + n_{l,k} \ , \tag{5.3}$$

where $n_{l,k}$ has the same characteristic as $w(nT_s')$ and $\theta_k = f_N(1+\epsilon) + \epsilon k \approx f_N + \epsilon k$. In the approximate expression (5.3), the ICI caused by small CFO and SFO can be omitted since its power is very small compared to the additive noise ($n_{l,k}$) power [57], [49]. The effect of slow drifts of the FFT window caused by small SFO ϵ is not shown in (5.3).

Some phase compensation techniques, e.g., [63], can be used to remove the phase rotation (5.3), and such techniques are popular in short packet transmission systems. However, the window shift caused by the small SFO ϵ, can be very large enough to introduce intolerable ISI in long packet based transmissions systems. For example, multiband-OFDM proposal [27] can have up to 1,000 symbols per packet, and the window shift caused by a 40 ppm SFO can be up to 6 samples. Thus, to remove both phase rotation and window shift, we need to estimate f_N and ϵ.

Similar to [49], we take the conjugate product of two consecutive OFDM symbols

$$x_{l,k} = z_{l,k} \cdot z_{l-1,k}^* \approx e^{j2\pi\rho\theta_k} a_{l,k} a_{l-1,k}^* |H_{l,k}|^2 + \text{noise} \ , \tag{5.4}$$

where $\rho = M/N$, $*$ denotes the conjugate operation, and we assume $H_{l,k} \approx H_{l-1,k}$.

C. Data-aided Estimator

A post-FFT data-aided (DA) CFO and SFO estimator was proposed in [50] and [52]

$$\hat{f}_N = \frac{1}{2\pi\rho} \cdot \frac{\varphi_{l,1} + \varphi_{l,2}}{2} \ , \quad \hat{\epsilon} = \frac{1}{2\pi\rho} \cdot \frac{\varphi_{l,2} - \varphi_{l,1}}{K/2} \ , \tag{5.5}$$

where $\varphi_{l,(1|2)} = \arg\left[\sum_{k\in P_{(1|2)}} x_{l,k}\right]$, $P_{(1|2)}$ denotes the first and the second half of pilots (MPSK modulated), respectively, which are assumed symmetrically and uniformly distributed around DC ($k = 0$).

It is easy to prove that estimators (5.5) are unbiased in the presence of AWGN and flat fading channels. In [52], the mean-square error (MSE) of (5.5) in AWGN channels are reported:

$$\mathrm{MSE}(\hat{f}_N) = \frac{1}{4\pi^2\rho^2 N_P \cdot E_s/N_o}\ , \quad \mathrm{MSE}(\hat{\epsilon}) = \frac{4}{\pi^2\rho^2 K^2 N_P \cdot E_s/N_o}\ , \tag{5.6}$$

respectively, where N_P stands for the number of pilots per symbol. To reduce synchronization overhead, we may use a reduced number of pilots. However, it will degrade the performance in (5.6). Furthermore, the pilot-based approach may be not possible in non-coherent systems since there is no pilot available.

In fact, the above estimator is not the optimal one. We find that the carrier frequency offset estimator [62] for single carrier systems can be easily modified to estimate SFO in OFDM systems and presents slightly better performance (not reported here due to space limitations). However, due to the high complexity of estimator in [62], we will focus on estimators similar to (5.5) hereafter.

D. Proposed Synchronization Scheme

1. Decision-Directed Estimator

In this chapter, we propose a decision-directed (DD) scheme to replace the conventional DA scheme,

$$\hat{f}_N = \frac{1}{2\pi\rho} \cdot \frac{\varphi_{l,1}^{'} + \varphi_{l,2}^{'}}{2}\ , \quad \hat{\epsilon} = \frac{1}{2\pi\rho} \cdot \frac{\varphi_{l,2}^{'} - \varphi_{l,1}^{'}}{K/2+1} \tag{5.7}$$

where

$$\varphi'_{l,(1|2)} = \arg\left[A_{l,(1|2)}\right] \ , \quad A_{l,(1|2)} = \sum_{k \in C_{(1|2)}} \frac{z_{l,k} z^*_{l-1,k}}{\hat{a}_{l,k} \hat{a}^*_{l-1,k}} \ , \tag{5.8}$$

and $C_1 = [-K/2, -1], C_2 = [1, K/2]$ denote 1st and 2nd half of data subcarriers, respectively. For coherent systems, data decisions are available right after the coarse synchronization and channel estimation. For non-coherent systems, we can use data decisions right after coarse synchronization.

To obtain reliable $\hat{a}_{l,k}$, we may use the outer channel decoder output to reconstruct the complex $\hat{a}_{l,k}$. However, such an approach requires more memory and arithmetic operations. Furthermore, the decoding and interleaver delay will degrade the tracking performance ([1], pp. 239).

A simpler way is to use the hard data decisions. In highly frequency-selective channels, the data decisions in spectral nulls might be unreliable. However, these decision errors have small contribution on the final estimate since $|H_{l,k}|^2$ are very small (5.4), and their effects are averaged out in (5.7) and (5.8). The decision directed synchronizer is plotted in Fig. 32.

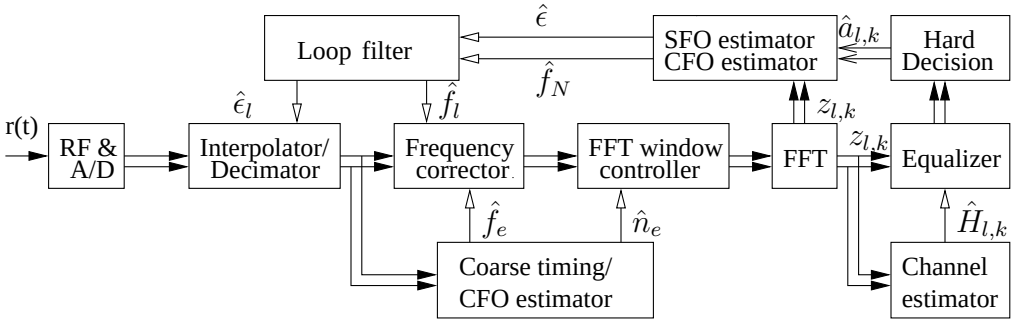

Fig. 32. The receiver structure.

In Appendix-E we show that the MSE of the proposed estimator in AWGN

channels is given by

$$\mathrm{MSE}(\hat{f}_N) = \frac{1}{4\pi^2\rho^2 K \cdot E_s/N_o} \ , \qquad \mathrm{MSE}(\hat{\epsilon}) = \frac{4}{\pi^2\rho^2 K(K+2)^2 \cdot E_s/N_o} \ . \tag{5.9}$$

which are much smaller than (5.5). Due to channel fading effects, as shown by the computer simulations in Fig. on p. 75, the MSE performance in F-S channels is slightly worse than (5.9).

In Appendix-F, we have also shown that estimators (5.7) are approximately unbiased in F-S channels for small ϵ. A similar proof can be carried out for the estimator (5.5) using some slight modifications.

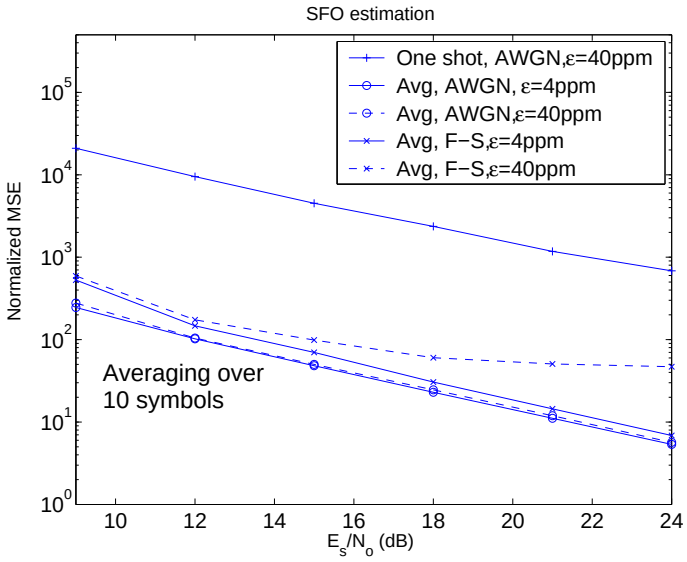

Fig. 33. Normalized MSE (normalized by 10^{-12}) of open-loop DD SFO estimators.

As we will show later in simulations, the above one-shot estimation may be not accurate enough for correction. As shown in Fig. 33, averaging over 10 symbols can greatly decrease the MSE in AWGN channels. Unfortunately, in F-S channels, an error floor is found for large SFO ϵ, which can be explained that (5.5) and (5.7) are not anymore unbiased for large SFO.

2. Closed-Loop Scheme

The above results suggest us to utilize a closed-loop synchronization scheme. The one-shot estimates are post-processed by following first-order tracking loop filters

$$\hat{f}_l = \hat{f}_{l-1} + \gamma_f \hat{f}_N, \qquad \hat{\epsilon}_l = \hat{\epsilon}_{l-1} + \gamma_\epsilon \hat{\epsilon} \ . \tag{5.10}$$

Symbol by symbol, the above loop filters update the control parameters of number-controlled oscillators in the interpolator and frequency corrector, and the residual frequency errors gradually converge to smaller values.

After convergence, the estimators exhibit small fluctuations about the stable equilibrium points. Based on a linearized equivalent model [2] , we can derive the tracking performance as follows

$$\text{MSE} = \int_{-1/(2T)}^{1/(2T)} S(f)|G(f)|^2 df \ , \tag{5.11}$$

where $S(f)$ is the power spectral density of loop noise (derived in Appendix-A)

$$S_{\text{CFO}}(f) = \frac{\sigma_n^2 T[1-\cos(2\pi fT)]}{4\pi^2\rho^2 K}, \quad S_{\text{SFO}}(f) = \frac{4\sigma_n^2 T[1-\cos(2\pi fT)]}{\pi^2\rho^2 K(K+2)^2} \ , \tag{5.12}$$

and $G(f)$ is the closed-loop transfer function given by

$$G(f) = \frac{-\gamma}{e^{j2\pi fT} - (1-\gamma)} \ . \tag{5.13}$$

Substituting (5.12)-(5.13) into (5.11), we can easily find the MSE of closed-loop DD estimators

$$\text{MSE}(\hat{f}_l) = \frac{\gamma_f^2/(2-\gamma_f)}{4\pi^2\rho^2 K \cdot E_s/N_o} \ , \qquad \text{MSE}(\hat{\epsilon}_l) = \frac{4\gamma_\epsilon^2/(2-\gamma_\epsilon)}{\pi^2\rho^2 K(K+2)^2 \cdot E_s/N_o}. \tag{5.14}$$

Similarly, we obtain the MSE of closed-loop DA estimators in [50] and [52]

$$\text{MSE}(\hat{f}_l) = \frac{\gamma_f^2/(2-\gamma_f)}{4\pi^2\rho^2 N_P \cdot E_s/N_o} \ , \qquad \text{MSE}(\hat{\epsilon}_l) = \frac{4\gamma_\epsilon^2/(2-\gamma_\epsilon)}{\pi^2\rho^2 K^2 N_P \cdot E_s/N_o}. \tag{5.15}$$

E. Computer Simulations

From [61], the modified Cramer-Rao bound (MCRB) for SFO estimation in AWGN channels is given by

$$\mathrm{MCRB}(\epsilon) \approx \frac{9}{2\pi^2 K^3 L^3 (M/N)^2 E_s/N_0} \ , \tag{5.16}$$

where L is the equivalent number of symbols $L = \sqrt{2-\gamma_\epsilon}/\gamma_\epsilon$.

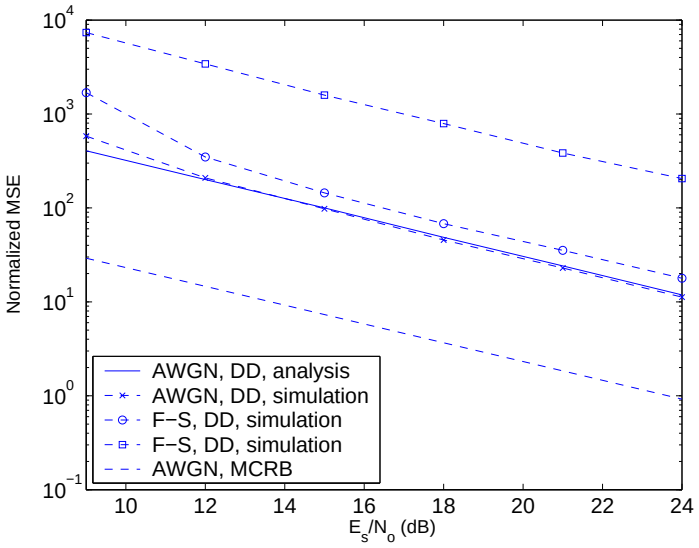

Fig. 34. Normalized MSE (normalized by 10^{-12}) of closed-loop SFO estimators.

In the loop filters, we use $\gamma_\epsilon = 0.2$ and $\gamma_f = 0.3$ for both DD and DA schemes. The closed-loop tracking performance of the DD scheme in Fig. 34 which is much closer to the MCRB than the conventional DA scheme, corroborates the closed-loop analysis result presented in Section IV. At low SNRs, the simulation results for the DD scheme deviate from the analysis results, a fact which is due to error propagations. However, error propagations are hardly found for SNRs larger than 12 dB.

F. Summary

We have introduced a new decision-directed post-FFT joint estimator for the carrier frequency offset and sampling clock frequency offset in OFDM systems. By performance analysis and computer simulations, we prove that our new scheme exhibits much better performance compared to conventional data-aided scheme in both AWGN and frequency-selective channels. Since we save the pilots for synchronization, the throughput of system is also increased. With very few additional hardware, this new synchronization scheme can be implemented in many wireless OFDM systems.

CHAPTER VI

ADAPTIVE NARROWBAND INTERFERENCE MITIGATION FOR MB-OFDM UWB SYSTEMS

In last two sections, we have discussed coarse and fine synchronization for OFDM systems. This chapter will focus on the analysis of the impacts of narrowband interference (NBI) and the design of efficient NBI mitigation scheme for OFDM systems.

A. Introduction

The high data rate, low-power, huge spatial capacity and high precision ranging of ultra-wideband (UWB) [27] communications promise to address the needs of the quickly growing home networking market that are not currently being met by the existing communication schemes [64]. According to the Federal Communications Commission (FCC) regulations [28] and [65], the transmitted power level of UWB systems is limited to -41.3 dBm/MHz and can be spread over a huge bandwidth 7.5 GHz. Such a noise floor operation enables the coexistence of UWB devices with other services such as GPS, IEEE 802.11 WLANs, etc. Due to their low transmission power and huge reception bandwidth, UWB systems are subject to intentional and unintentional[1] narrowband interferences (NBI) [66].

The scope of this chapter is to analyze the impacts of NBI on the performance of a multi-band (MB) OFDM UWB receiver [27] and to design efficient signal processing schemes for acquisition and extraction of information in the presence of NBI. We remark that our contributions are complementary to the results reported in [67], where a unifying performance analysis of UWB systems in the presence of NBI was

[1]The radiation level of unintentional NBI is only limited by FCC Part 15 rule to not more than -41.3 dBm/MHz.

reported for UWB multiple access schemes encompassing direct-sequence (DS), single and multi-carrier (SC/MC), and time hopping (TH) modulations and Rake receivers. Thus far, most of the existing works have focused on digital NBI cancellation for spread spectrum systems (see [68] and [6] and the references cited therein) and these techniques do not represent viable solutions for MB-OFDM UWB systems. The main impediments of the digital NBI suppression schemes [68] and [6] are the need for high precision analog-to-digital converters (ADC) and high complexity digital processing elements. Due to their huge bandwidths, UWB receivers usually employ low-bit ADCs, e.g., 4-bit uniform ADCs as suggested by [27]. In addition, a NBI might increase significantly the level of quantization noise at the output of ADCs [71]- [73], which might require higher precision ADCs in order to ensure a negligible loss in performance of the overall receiver. Therefore, it is necessary to develop novel and low complexity NBI mitigation schemes for MB-OFDM UWB receivers that take into account the effects induced by NBI.

One of the main results of this chapter is the development of a mixed (hybrid) interference mitigation scheme that consists of a digital NBI detector and an adaptive analog notch filter (AANF). Our study shows that such mixed schemes could be applied with success to combat strong NBI (i.e., interferences that give rise to signal-to-interference ratios (SIR) less than 0 dB) in MB-OFDM UWB receivers. It is also found that for combating mild interferences (i.e., those interferences for which SIR $\geq$ 0 dB), it is sufficient to consider a low-complexity digital frequency excision method. Our comprehensive simulations show that in the presence of strong NBI, a mixed NBI mitigation scheme provides a significant gain (9 dB) relative to a receiver that assumes only a digital frequency excision method.

An additional contribution of this chapter is an in-depth analysis of the impact of NBI on the signal-to-interference-and-noise ratio (SINR) loss at the output of

ADC and on the performance of the carrier frequency offset (CFO) estimator. The importance of these studies is due to the fact that the SINR at the output of ADC serves as a good metric to evaluate the uncoded bit error rate (BER) performance of a MB-OFDM UWB receiver, and that very accurate CFO estimators (offsets less than 1% of the subcarrier spacing) are needed in order to keep the BER degradation to less than 0.1 dB [17]. Our study finds that NBI introduces significant degradation in the conventional carrier frequency offset estimators [18] - [24], and that the CFO estimator based on the pseudo-noise (PN) matched-filtering method [26] presents the most robust performance in the case when the SIR is larger than 0 dB. However, as the interference level increases, the performance of PN matched-filtering method also becomes unacceptable. These results suggest the need for synchronization schemes robust to NBI suppression.

The rest of this chapter is organized as follows. The system models of single-band and multi-band OFDM UWB receivers are depicted in Section II. The analysis of the impact of narrowband interference on the signal-to-interference-and-noise ratio at the output of analog-to-digital convertor, accuracy of carrier acquisition, and block error rate (BLER) performance of a MB-OFDM receiver are presented in Section III . Section IV addresses the problem of suppressing the narrowband interference in MB-OFDM receivers. For mitigation of mild interferences, a digital frequency excision method is first proposed and shown to perform well. For compensating strong narrowband interferences, it is found that a mixed mitigation scheme containing an adaptive analog notch filtering scheme and a digital detection scheme are necessary to be jointly operated. Also, comprehensive design considerations for the adaptive analog notch filter and performance analysis studies for the digital and mixed interference mitigation schemes are presented in Section IV. Finally, several concluding remarks are drawn in Section V.

B. Signal Model

1. Single-Band OFDM Systems

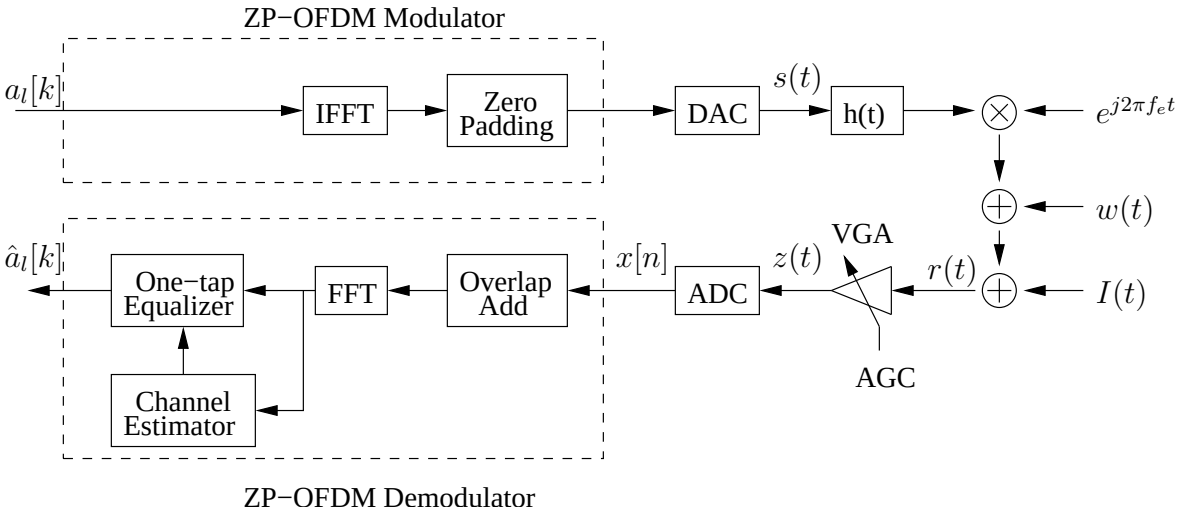

Fig. 35. The signal model of single-band OFDM systems.

The block diagram of a single-band (SB) OFDM system is generically represented in Fig. 35, and the transmitted signal is expressed as:

$$s(t) = \frac{1}{\sqrt{KT}} \sum_{l} \sum_{k \in C} a_l[k] e^{j2\pi k(t-lT_0)/T} g(t - lT_0) \ , \tag{6.1}$$

where $a_l[k]$, $1/T$, and $C = [-\frac{K}{2}, -1] \cup [1, \frac{K}{2}]$ stand for the QPSK modulated data, the subcarrier spacing, and the set of data subcarriers, respectively. The power of transmit symbols $a_l[k]$ is normalized to unity $P_a = E[|a_l[k]|^2] = 1$, $P_s = E[|s(t)|^2] = 1$, and $g(t)$ is a rectangular pulse of duration T_0.

As shown in Fig. 35, a discrete-time implementation of $s(t)$ that assumes the sampling period $T_s = T/N$ is generated by means of an N-point Inverse Fast Fourier Transform (IFFT). According to the Central Limit Theorem (CLT), $s[n] := s(nT_s)$ can be approximated as a complex Gaussian random variable (RV) for sufficiently large number of subcarriers $N \geq 20$. In addition, the OFDM modulation assumes

a zero-padding of length $T_g = N_g T_s$ at the end of each symbol [74] instead of a cyclic prefix (CP). Such modulations are referred as zero-padding (ZP) OFDM and their properties were analyzed comprehensively in [74]. Unlike CP-OFDM modulations, ZP-OFDM modulations present the important feature that their power spectral densities do not contain significant spectral line components. Therefore, ZP-OFDM appears as a viable solution to avoid significant transmitter power back-off in UWB transceivers [75]. In addition, if the duration of multipath channel $h(t)$ is shorter than the guard interval T_g, reference [74] has shown through simple overlap-and add-(OLA) operations, FFT and one-tap equalization that the ZP-OFDM receiver achieves a good performance (very close to that of a CP-OFDM receiver).

After digital-to-analog conversion (DAC), the transmitted signal $s(t)$ propagates through the multipath channel with impulse response $h(t)$ [76] and is further corrupted by thermal noise $w(t)$ with power P_n, and by narrowband interference $I(t)$ with power P_i. Thus, the received signal can be expressed by

$$r(t) = e^{j2\pi f_e t}[s(t) \otimes h(t)] + w(t) + I(t) \ , \tag{6.2}$$

where $\otimes$ is the convolution operator, $P_c = \int |h(t)|^2 dt$ represents the channel power, and f_e denotes the carrier frequency offset, i.e., the frequency mismatch between transmitter and receiver.

The narrowband interference is modeled by a linearly modulated signal of the form:

$$I(t) = A_i \sum_n b_n e^{j(2\pi f_i t + \Phi_i)} p(t - nT_i) \ , \tag{6.3}$$

where b_n stands for the modulated symbols of the interference, T_i denotes the symbol period, and $p(t)$ is a rectangular pulse [77]. The parameters $A_i = \sqrt{P_i}$, f_i and Φ_i stand for the carrier amplitude, frequency, and phase, respectively. If $T_i = T$, then

the interference can be viewed as a modulated subcarrier. On the other hand, if $T_i >> T$, one can interpret $I(t)$ as an unmodulated tone. Thus, the NBI model (6.3) is sufficiently general to encompass a broad class of interferers. We remark also that all the ensuing derivations hold also for other models of NBI interferences such as single tone [5], [78], rectangle spectrum interferer [79], or AR-process [80].

2. Multi-Band OFDM Systems

According to FCC regulations, the power spectral density (PSD) of UWB transmitters should be less than -41.3 dBm/MHz, which imposes a very tight constraint for the UWB systems. To transmit more power and thus improve the link budget, a huge bandwidth is used by UWB systems. However, current technology puts an upper limit for the performance of analog and digital processing elements, i.e., designing a low-power 4-bit ADC is a non-trivial task for current circuit designers. Therefore, it is undesirable to increase the working frequency of baseband processing. A better way to increase the system bandwidth is to apply frequency-hopping to a conventional OFDM system. Such OFDM systems equipped with frequency-hopping are called multi-band (MB) OFDM systems [27].

In the MB-OFDM transmitter, $s_l(t)$ represents the lth symbol modulated by the ZP-OFDM technique and is spread over J sub-bands by frequency-hopping:

$$s(t) = \sum_l s_l(t - lT_0) e^{j2\pi H[(l)_P]\Delta f t} \,, \tag{6.4}$$

where Δf is the frequency separation between two neighboring sub-bands, $(\cdot)_P$ denotes the modulo P operator, and $\{H(i),\ i \in [1, P]\}$ is the frequency-hopping sequence with period P, which may be larger than the number of sub-bands J. The IEEE 802.15.3a proposal [27] assumes the following set of parameters $J = 3$, $P = 6$ and $\Delta f = N/T$.

In the MB-OFDM receiver, the received signal is at first down-converted to baseband by a fast switching local oscillator (LO), which uses the same hopping frequency as the one used by the transmitter. The signal is next lowpass filtered to remove the interference from neighboring sub-bands. The ensuing processing elements are quite similar to that of a SB-OFDM receiver, except of the fact that a MB-OFDM receiver requires independent channel estimators and equalizers for each sub-band.

To gain a comprehensive understanding of the impact of a narrowband interference on the performance of a MB-OFDM receiver, we will next analyze the effects of NBI on the operation of ADC, carrier synchronizer, and BLER-performance of overall system.

C. Impact of Narrowband Interference

1. Optimization of Data Converters

In the absence of narrowband interference, the received signal takes the form:

$$r(t) = e^{j2\pi f_e t}[s(t) \otimes h(t)] + w(t) \ . \tag{6.5}$$

Therefore, the average power of $r(t)$ is given by $P_r = P_c + P_n$.

Due to the channel fading, $r(t)$ presents a very large dynamic range. As illustrated by Fig. 35, to improve the efficiency of the finite precision ADC, a variable-gain amplifier (VGA) is used to normalize the power of signal $r(t)$ to a desirable level. The normalized signal $z(t)$ is next sampled by ADC $z[n] = z(nT_s)$, and quantized into the digital signal $x[n]$. Let P_z denote the power of $z(t)$. The gain of VGA can be expressed as $G = \sqrt{P_z/P_r}$. Note that two ADCs are required for the complex-valued signal $z(t)$.

If the maximum quantization level of ADC is assumed equal to unit, then the

peak-to-average ratio (PAR) of a single ADC can be defined as

$$\Omega = \frac{1}{P_z/2} \, . \tag{6.6}$$

In practice, the VGA is controlled by an automatic gain controller (AGC) and assumes the following operational regime. At first, the VGA uses a predefined gain and the output $z(t)$ is pre-sampled by ADC. Then, the AGC estimates the root mean-square (RMS) level of the pre-sampled digital signal, compares it with the desirable RMS level $\sqrt{P_z}$, and generates a proper gain controlling signal for VGA. Usually, this closed-loop operation requires several iterations to normalize $z(t)$ to the desirable level [81].

To achieve a sampling speed as high as 528 MHz in OFDM-UWB receivers [27], a low-bit memoryless uniform ADC appears as the best solution. For a uniform b-bit ADC, the number of quantization levels is 2^b, and the quantization step size is given by

$$\Delta = \frac{2}{2^b - 1} \, . \tag{6.7}$$

The power of complex quantization noise $q[n] := x[n] - z[n]$ can be expressed as [71], [73]:

$$\begin{aligned} P_q &= 4 \sum_{i=0}^{2^{b-1}-2} \int_{i\Delta}^{(i+1)\Delta} (z - (i+1/2)\Delta)^2 \, p(z) dz \\ &\quad + 4 \int_{1-\Delta/2}^{\infty} (z-1)^2 \, p(z) dz \, , \end{aligned} \tag{6.8}$$

where $p(z)$ represents the probability density function (pdf) of the I (in-phase) and Q (quadrature) components of $z[n]$. Notice also that for a quasi-static channel model $h(t)$ [76], $z[n]$ can be expressed as

$$z[n] = G e^{j2\pi v n} \sum_{m=0}^{M-1} s[n-m] h[m] + w[n] \, , \tag{6.9}$$

where $v = f_e T_s$ stands for the normalized CFO, and M denotes the number of paths (normalized channel delay spread). According to [76], M is normally a large number ($M > 15$) in the case of UWB channels. Since both $s[n]$ and $w[n]$ can be interpreted as complex Gaussian RVs, and with no loss of generality each path of $\{h[n]\}$ can be assumed independently and identically distributed, then $z[n]$ can also be viewed as a complex Gaussian RV. Therefore, given b and P_z, one can easily calculate P_q. The signal-to-quantization-noise ratio of ADC is given by

$$\gamma_q = \frac{P_z}{P_q} \, . \tag{6.10}$$

For a given b, the optimum Ω can be found by solving $\partial \gamma_q / \partial \Omega = 0$ [71].

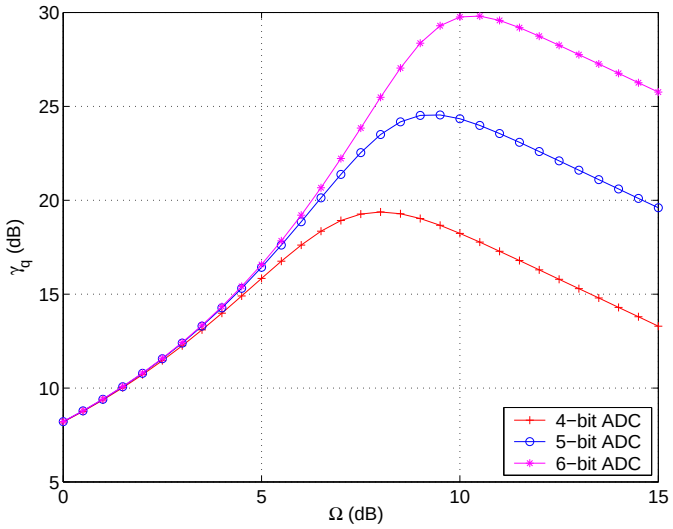

Fig. 36. γ_q versus Ω and number of bits of ADC.

In Fig. 36, we plot the numerically calculated γ_q versus different values of b and Ω. The optimum values of Ω for a specific b-bit ADC are listed in Table I. It turns out that higher precision ADCs lead to larger Ω and higher γ_q.

For the output $x[n]$ of ADC, the signal-to-noise (quantization and thermal noise)

Table I. Optimum Ω versus ADC bit number for OFDM receiver in AWGN channels.

ADC bit number	Optimum Ω (dB)	Best γ_q (dB)
4	8.0	19.4
5	9.3	24.6
6	10.3	29.8

ratio (SNR) is given by

$$\text{SNR} = \frac{G^2 P_c}{P_q + G^2 P_n} \ . \tag{6.11}$$

Assuming perfect carrier frequency synchronization, one can find that the FFT of the lth symbol is given by

$$X[k] = \text{FFT}(z[n] + q[n]) = G(A[k]H[k] + W[k]) + Q[k] \ , \tag{6.12}$$

where $Q[k]$, $H[k]$ and $W[k]$ stand for the FFT of $q[n]$, $h[n]$ and $w[n]$, respectively. According to the CLT, $Q[k]$ can be modeled as a Gaussian RV. Therefore, $X[k]$ can be viewed as Gaussian RV, as well. After some direct manipulations, one can find that

$$\text{SNR} = \frac{P_c}{(P_c + P_n)/\gamma_q + P_n} \ , \tag{6.13}$$

which can be used to evaluate the uncoded bit error rate (BER) of the OFDM receiver. As shown by [72], the theoretical BER derived from (6.13) coincides with the simulated results.

In the presence of narrow-band interference, the output of ADC becomes

$$x[n] = G(e^{j2\pi\upsilon n} \sum_{m=0}^{M-1} s[n-m]h[m] + w[n] + I[n]) + q[n] \ . \tag{6.14}$$

Defining the signal-to-interference-plus-noise-ratio (SINR) by

$$\text{SINR} = \frac{G^2 P_c}{P_q + G^2(P_n + P_i)} \ , \tag{6.15}$$

one can easily find that

$$\text{SINR} = \frac{P_c}{(P_c + P_n + P_i)/\gamma_q + (P_n + P_i)} \ . \tag{6.16}$$

Comparing (6.16) with (6.13), we find that NBI introduces two effects:

1. The increase of received signal power P_r leads to a smaller gain G for VGA, which increases the normalized quantization noise $P_q/G^2 = (P_c + P_n + P_i)/\gamma_q$.

2. Due to its sub-band occupancy effect in the frequency domain, interference degrades directly the receiver's performance.

Now we will focus on the enlarged ratio P_q/G^2 and assume that the NBI can be removed digitally. Omitting the term $G^2 P_i$ in (6.15) yields

$$\text{SINR} = \frac{P_c}{(P_c + P_n + P_i)/\gamma_q + P_n} \ . \tag{6.17}$$

Assuming the same optimal value for γ_b as the one given by Table I and denoting $\text{SIR} = P_c/P_i$ as the signal-to-interference ratio (SIR) of $r(t)$, we compare the SINR curves of ADC in Fig. 37. As shown in Fig. 37, as the NBI becomes stronger (lower SIR), the SINR of ADC is reduced, e.g, reducing the SIR from 20 dB to 0 dB results in 0.5 dB SINR loss for the 4-bit ADC.

In the above analysis, we used the value of γ_q, which was previously derived by assuming a Gaussian distribution for the input signal. However, such a value might not be optimal for non-Gaussian inputs. If $T_i >> T$ and the interference level increases, $r(t)$ becomes a sinusoid-like waveform, and therefore both the I and

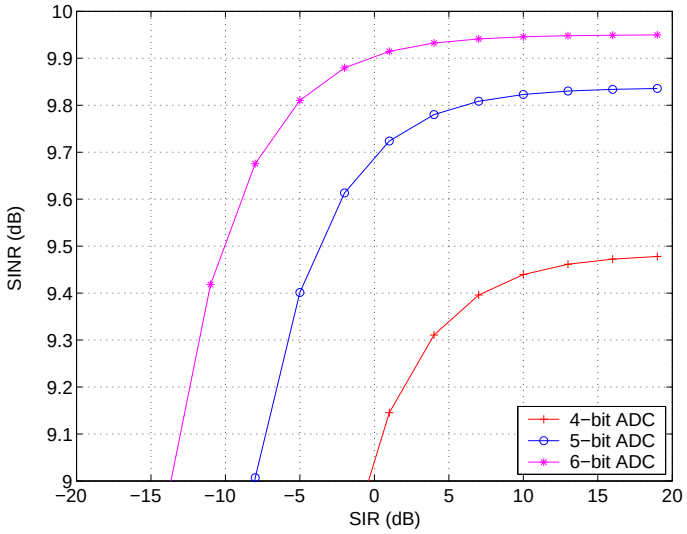

Fig. 37. SINR curves of ADC, $P_c/P_n = 10$dB.

Q-components of $I[n]$ can be modeled as RVs with pdf:

$$p(I) = \frac{1}{\pi\sqrt{P_i - I^2}} , \qquad I \in [-\sqrt{P_i}, \sqrt{P_i}] . \tag{6.18}$$

Therefore, $z[n]$ is a mixed RV depending on the Gaussian input $G(s[n] + w[n])$ and non-Gaussian input $GI[n]$, and the pdf of its I and Q-components is given by

$$p(z) = \frac{1}{\sqrt{2\pi G^2(P_c + P_n)}} \int_{-G\sqrt{P_i}}^{G\sqrt{P_i}} \exp\left(\frac{-(z-I)^2}{2G^2(P_c+P_n)}\right) \cdot \frac{1}{\pi\sqrt{G^2P_i - I^2}} dI . \tag{6.19}$$

Substituting (6.19) into (6.8), we can calculate P_q numerically. As shown in Fig. 38, the increase of NBI power (smaller SIR) leads to larger γ_q for optimal Ω.

The SINRs of the ADC with optimal and non-optimal γ_q are compared in Fig. 39, which shows that the SINR is improved by using an optimal value for Ω. However, to obtain the optimized SINR requires knowledge of SIR for $r(t)$, a parameter which may be difficult to obtain in a practical receiver. We also remark that even with the above optimized AGC and ADC, the SINR loss caused by NBI is still significant for

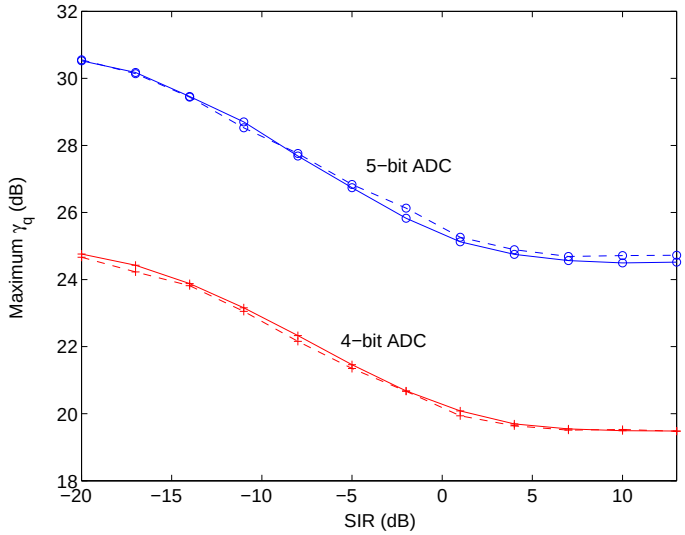

Fig. 38. Theoretical (dashed line) and simulated (solid line) optimum γ_q versus SIRs.

a UWB receiver.

To reduce the SINR loss caused by the NBI, it appears that one might need to use a higher precision ADC. Let us assume that the maximum implementation loss of the receiver is 0.6 dB, which means that the SINR at the ADC output should be larger than 9.4 dB if $P_c/P_n = 10$ dB. As shown in Fig. 39, for weak interference (e.g., SIR>7 dB), we may use 4-bit ADCs to achieve SINR= 9.4 dB. However, as the interference level increases, higher precision ADCs may be required to obtain a satisfactory SINR. In addition, it is known that the accuracy of representation in digital signal processing (DSP) elements (e.g., FFT) depends on the number of bits used by the ADC. Therefore, increasing the number of bits in the ADC will lead to high precision DSP elements, which is undesirable for UWB receivers.

2. Carrier Synchronization

As discussed before, conventional CFO estimation algorithms exploit cross correlations in the time domain by using repeated training symbols [18]- [19], [24], or the

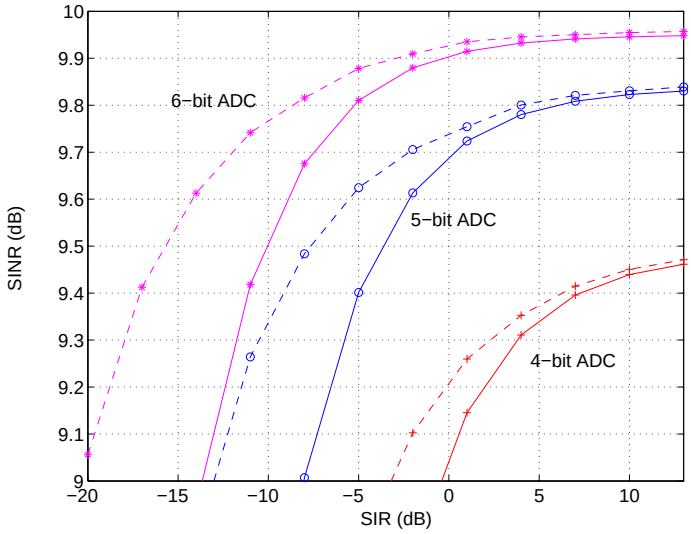

Fig. 39. SINR with non-optimal γ_q (solid line) and with optimal γ_q (dashed line), $P_c/P_n = 10$dB.

redundancy present in the modulated OFDM symbol [22]. These algorithms work well in the absence of NBI. However, UWB systems can be subject to significant NBI. Very recently, Coulson reported that the performance of the conventional carrier synchronization algorithms could be seriously degraded by NBI [78]. Our goal herein is to provide a more rigorous analysis of the effects introduced by NBI on the CFO synchronizer and to propose a more robust CFO synchronization scheme relative to the existing algorithms. To simplify the exposition, we will assume a flat-fading channel model and assume that the NBI interference is modeled as an unmodulated sinusoid. Furthermore, since the focus is on the impact of the NBI, the additive noise is omitted in the received preamble. The main conclusion of this study is that the novel CFO estimation scheme [26] appears as the most robust scheme among the existing algorithms, and therefore we will focus next on its performance in the presence of NBI.

The CFO synchronization scheme [26] assumes a preamble $\{s[n]\}$ of length $2L$,

which consists of two identical pseudo-noise (PN) sequences in the time domain: $s[n] = s[n+L],\ n = 0, \cdots, L-1$. The model for the received signal in the presence of NBI is given by:

$$r[n] = A_c e^{j(2\pi v n + \theta)} s[n] + A_i e^{j(2\pi \xi n + \Phi)} \ , \tag{6.20}$$

where $A_c = \sqrt{P_c}$ and θ stand for the amplitude and phase of the channel, respectively. The normalized frequency of NBI is $\xi = f_i T_s$. In the receiver that assumes the synchronization scheme [26], the received signal $r[n]$ is correlated with the local PN sequence using an L-tap PN matched-filter

$$x[l] = \sum_{n=0}^{L-1} r[l-n] s^*[n] \ , \tag{6.21}$$

where l denotes the timing offset. Due to the repetitions in the preamble, the output of the PN matched-filter presents two correlation peaks:

$$\begin{aligned} x[0] &= A_c \alpha e^{j[\pi v(L-1)+\theta]} + I_d \ , \\ x[L] &= A_c \alpha e^{j[\pi v(3L-1)+\theta]} + e^{j2\pi\xi L} I_d \ , \end{aligned} \tag{6.22}$$

where the approximation $\alpha = \sin(\pi v L)/\sin(\pi v) \approx L$ for small v holds in a UWB receiver, and I_d denotes the NBI despread by the PN sequence $s^*[n]$:

$$I_d = \sum_{n=0}^{L-1} A_i e^{j2\pi\xi n + \Phi} s^*[n] \ . \tag{6.23}$$

Assuming perfect timing synchronization $l = 0$, one can find

$$x^*[0]x[L] \approx L^2 P_c e^{j2\pi v L} + e^{j2\pi\xi L} |I_d|^2 + 2A_c L \beta e^{j\pi L(\xi - v)} \ , \tag{6.24}$$

where $\beta = \Re\left\{ I_d e^{j\pi(\xi L - v(2L-1))} e^{j[\Phi - \theta]} \right\}$. The expression of the CFO estimator [26]

takes the form:

$$\hat{v} = \frac{1}{2\pi L} \arg\{x^*[0]x[L]\} \ . \tag{6.25}$$

Some straightforward manipulations lead to

$$L(\hat{v} - v) = \frac{1}{2\pi} \arctan \left\{ \frac{\sin(2\pi L(\xi - v))|I_d|^2 + 2A_c L\beta \sin(\pi L(\xi - v))}{L^2 P_c + \cos(2\pi L(\xi - v))|I_d|^2 + 2A_c L\beta \cos(\pi L(\xi - v))} \right\} \ , \tag{6.26}$$

which indicates that $L(\hat{v} - v)$ depends on $(\xi - v)$ and I_d, and therefore the CFO estimator is biased. Due to the despreading operation in (6.23), viewing $s[n]$ as a random sequence leads to $E\{I_d\} = 0$ and $E\{|I_d|^2\} = LP_i$. If SIR $= P_c/P_i >> 1/L$, the expected value of the bias conditioned on v and ξ can be approximated by

$$E\{L(\hat{v} - v)\} \approx \frac{1}{2\pi} \cdot \frac{\sin(2\pi L(\xi - v))}{L \cdot \text{SIR} + \cos(2\pi L(\xi - v))} \approx 0 \ , \tag{6.27}$$

which indicates that unlike the conventional CFO estimators [18]- [24], the PN matched-filter based CFO estimator (6.25) is approximately unbiased as long as SIR $>> 1/L$. To check the above results, we run simulations to compare the normalized mean-square errors (MSEs) $E\{L^2(\hat{v} - v)^2\}$ of (6.25) and Coulson's CFO estimator [24]. The simulations assume $v = 0.08$, $L = N = 128$, ξ is uniformly distributed over $(-0.4,\ 0.4)$, and P_c/P_n is fixed to 5 dB. The theoretical value of normalized MSE in AWGN channels is given by

$$E\{L^2(\hat{v} - v)^2\} \approx \frac{1}{4\pi^2 \cdot L \cdot P_c/P_n} \ , \tag{6.28}$$

which is a lower bound for the two CFO estimators [24], [26].

As shown in Fig. 40, the performance of both methods deteriorates as SIR decreases. Compared to Coulson's estimator, the estimator [26] presents much better performance over the SIR range of interest. At high SIR (> 5 dB), the normalized MSE of method [26] converges to the lower bound (6.28). These results suggest that

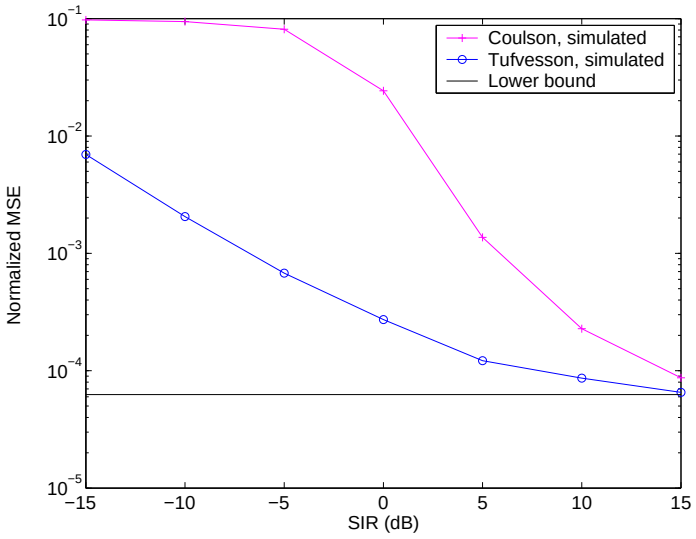

Fig. 40. The performance of CFO estimators versus SIR, $v = 0.08$, $L = 128$, and $P_c/P_n = 5$dB.

(6.25) is the preferred CFO estimator in the presence of NBI. However, as shown in Fig. 40, if interference is stronger, e.g., SIR<0 dB, the normalized MSE of (6.25) is much larger than 1E-4, which could introduce significant system performance degradation.

3. System Performance of a MB-OFDM Receiver

We have already shown that narrowband interference increases the quantization noise of ADC and might cause significant errors in the CFO estimator of the receiver. In addition to these effects, the NBI might enter directly into the frequency domain and cause significant performance losses.

To evaluate the overall impacts of NBI on a MB-OFDM system [27], we run simulations with the configuration parameters from Table II. Reference [76] defines four quasi-static multipath channels models for UWB systems, and channel model 1 (90 normalized channel realizations) is used in our simulations.

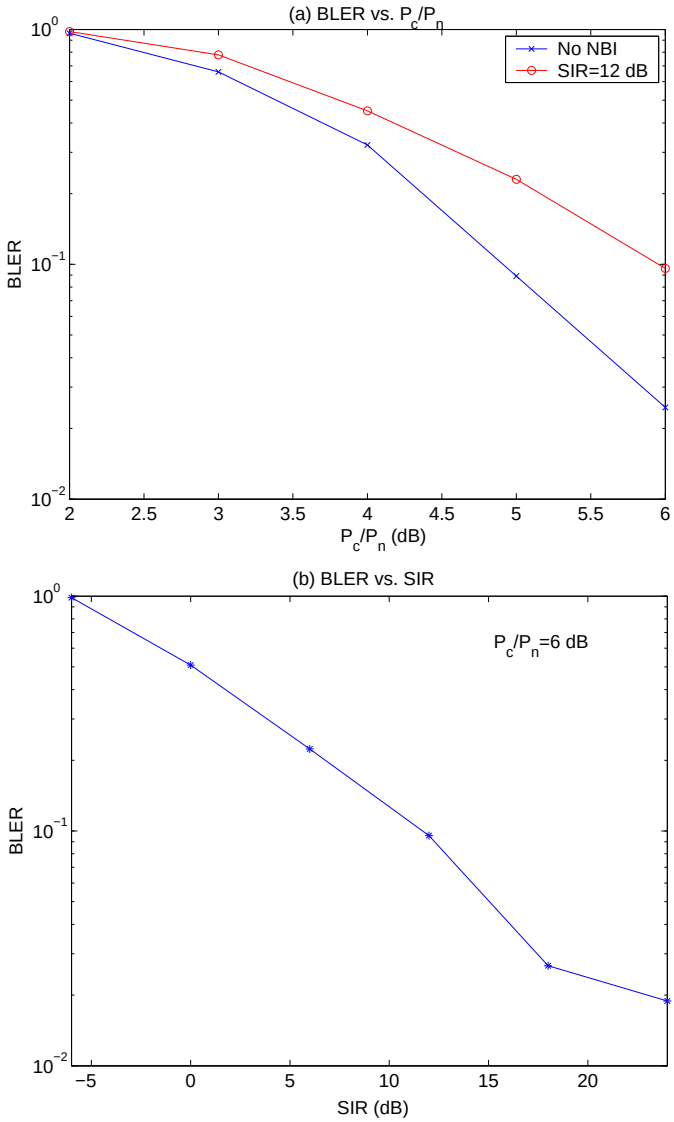

Fig. 41. The block error rate versus P_c/P_n and SIR.

Table II. The simulation configuration of MB-OFDM systems.

Modulation type	MB-OFDM proposal, 3 sub-bands
OFDM modulation parameters	$N = 128$, N_g=37
Data rate	200 Mbps
Packet length	128 bytes
Propagation channels	IEEE 802.15.3a channel model 1
Interference	Modulated NBI in sub-band 1
Timing and carrier synchronization	Perfect
Channel estimation	Using 2 pilot symbols/sub-band
AGC algorithm	RMS of received preamble
ADC	uniform 4-bit ADC, $\Omega = 8$ dB
Viterbi decoding	Soft decision (4-bits)

In Fig. 41 we compare the block error rate (BLER) for different P_c/P_n and SIRs. Fig. 41 (a) shows that when compared to the ideal system (without NBI) a small NBI of SIR = 12 dB could cause 1 dB loss at BLER= 0.1. In Fig. 41 (b), one can find that for a fixed $P_c/P_n = 6$ dB, the BLER is monotonically increasing as the SIR is reduced. Thus, to avoid the performance loss caused by NBI, an efficient interference suppression technique is required.

D. Narrowband Interference Suppression

Historically, most of the NBI suppression methods were reported for spread spectrum systems. The works [70]– [6] outline the most relevant NBI mitigation schemes, which can be broadly classified into two main groups.

The first class of methods is motivated by the fact that the received signal consists

of a correlated NBI and an uncorrelated spread spectrum signal. A pre-whitening filter [68]– [70] can be used to reduce the correlation of the received signal, and thus to suppress the NBI. The pre-whitening filter is found to improve the performance of spread spectrum receivers especially when the interference is strong [70]. However, the underlying assumption required by this class of methods can not be further extended since the OFDM signal is correlated during one symbol period.

When compared to the desired wideband signal, the interference occupies a much smaller frequency band and presents a higher power spectral density. Motivated by this fact, the second class of methods relies on transform domain filtering techniques to suppress the NBI. By converting the received signal into the frequency domain via real-time transform devices [69], one can easily determine the frequency location of NBI. The part of the signal corrupted by NBI is excised in the frequency domain and the remaining signal is re-transformed into the time domain. This method appears to be also fit for NBI suppression in OFDM receivers.

1. Digital NBI Detection and Mitigation

The detection of NBI requires an FFT device, which is already present in an OFDM receiver. Since the phase of NBI is unknown, the NBI has to be detected noncoherently based on the absolute values of the received signal samples. In Fig. 42, the magnitude-squared of the received signal samples $|X[k]|^2$ are plotted. Fig. 42-(a) shows that for flat-fading channels it is straightforward to ascertain the fact that the highest peak corresponds to the subcarrier affected by NBI. Therefore, by comparing the magnitude-squared of the FFT bins $|X[k]|^2$ with a threshold T_0, one can easily find out not only the existence of NBI but also the subcarrier location of NBI. The performance of the NBI detector depends on the value of threshold: a too small T_0 could lead to large false alarms, while a larger T_0 could increase the probability of a

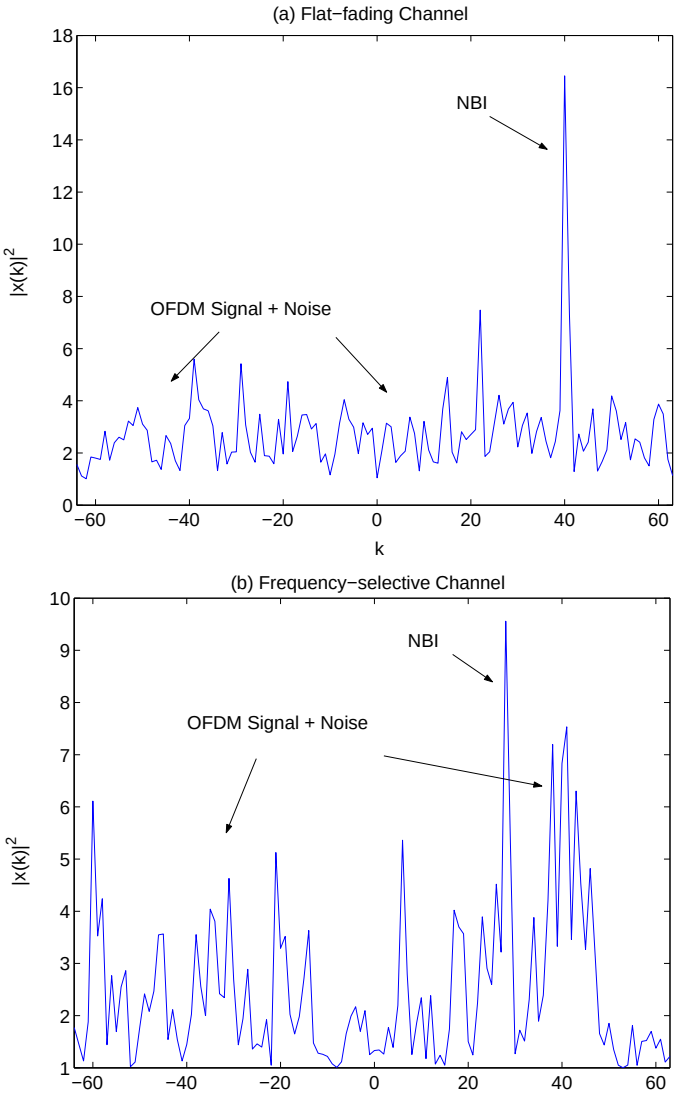

Fig. 42. The magnitude-squared of FFT bins: $|X[k]|^2$, SIR $= 8$ dB, $P_c/P_n = 5$dB.

miss. In general, the Neyman-Pearson detection framework could be used to optimize the value of threshold T_0.

Fig. 42-(b) shows that in frequency-selective channels the OFDM signal presents a large dynamic range, and some signal peaks could take values close to the peak induced by NBI. This observation indicates that the detection of NBI becomes difficult in frequency-selective channels, especially if the SIR is high. Fortunately, in packet-oriented UWB systems, for most of the time the channel is clear of the transmitted signal. To avoid the effects introduced by the OFDM signal, we may detect the NBI during the time interval between the two packets.

Since the subcarriers corrupted by NBI are not reliable anymore, they should not be used during the demodulation. The method of erasing the corrupted subcarriers is referred to as frequency excision, and the lost data caused by excision can be recovered by exploiting channel decoding techniques. To evaluate the performance of the frequency excision method, we run simulations assuming an MB-OFDM receiver. It is well known that, due to the finite window length, the FFT outputs are subject to a spectral leakage phenomenon and the NBI could be leaked to neighboring subcarriers. To resolve this problem, in addition to the center subcarrier where the NBI is located, 4 adjacent subcarriers are also excised in our simulations.

The BLER plots in Fig. 43 show that relative to the conventional receiver with no frequency excision, the frequency excision method can greatly improve the performance. To achieve BLER= 0.05, the conventional receiver requires SIR= 15 dB. However, the receiver with frequency excision can allow the SIR to be as low as 0 dB. Fig. 43 also shows that as SIR decreases, the BLER of the receiver with frequency excision increases very quickly. This result is caused by the following facts:

1. As the NBI becomes stronger, the normalized quantization noise P_q/G^2 is in-

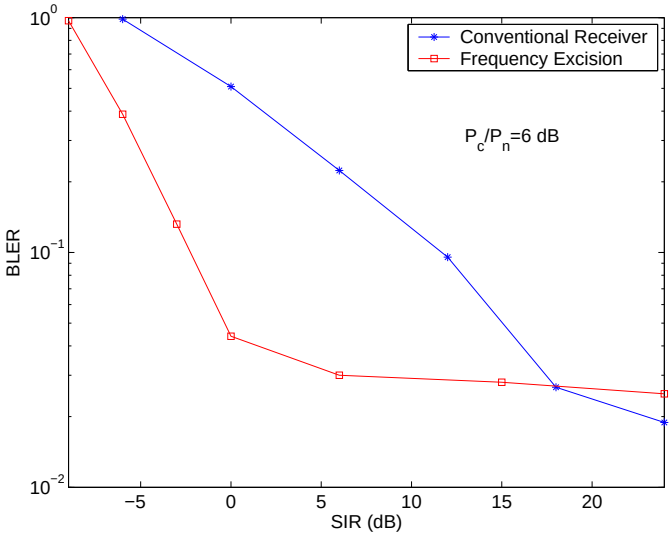

Fig. 43. Performance comparison of MB-OFDM receiver assuming ideal NBI detection.

creased, which leads to the SINR loss (6.17).

2. As a consequence of the increase of NBI power, the spectral leakage problem becomes worse: more power of NBI will be leaked to the neighboring subcarriers.

There are some possible digital solutions, e.g., increasing the number of bits of the ADC could reduce the quantization noise, and using larger size FFTs could remedy the spectral leakage problem. However, the complexity of these solutions may be too high to be affordable for practical UWB receivers. To suppress strong interference (SIR< 0 dB), we need to find a low complexity scheme, a study which will be conducted in the next sub-section.

2. Analog NBI Cancellation

The above results indicate that the performance of an OFDM based UWB receiver is degraded by narrowband interference, and the frequency excision method cannot remedy the performance degradation when SIR<0 dB. These problems occur due to

the fact that the gain of the VGA is set according to the power of the interference, effectively increasing the quantization noise of the ADC as compared to the desired signal. The logical solution to this problem is to remove the interference before it enters the AGC and ADC. By removing the interference before it enters the digital domain, the above mentioned performance degradation is avoided. This observation motivates us to propose a new interference suppression scheme, which is based on an adaptive analog notch filter (AANF) to filter the NBI out of the received signal. The structure of the proposed NBI suppression scheme is shown in Fig. 44.

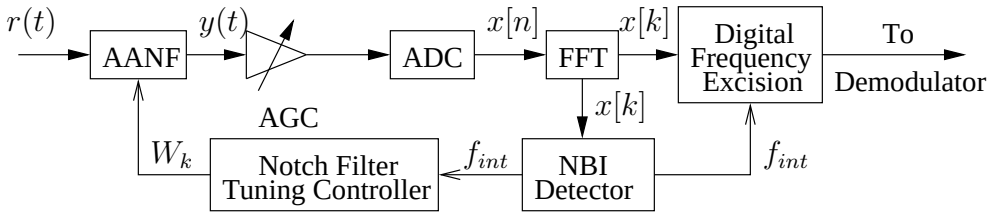

Fig. 44. The structure of proposed NBI suppression scheme.

A notch filter with a single notch frequency can be modeled by the following Laplace transfer function

$$H(s) = \frac{s^2 + 2\pi f_{BW} A_{notch} s + (2\pi f_0)^2}{s^2 + 2\pi f_{BW} s + (2\pi f_0)^2} \ , \tag{6.29}$$

with f_o, f_{BW}, and A_{notch}, respectively, representing the center frequency, the -3 dB bandwidth, and the filter's attenuation at $f = f_0$.

Fig. 45 displays the amplitude and step response of (6.29) for the two cases of $f_0 = 20$ and $f_0 = 40$, with $f_{BW} = 24$ MHz. The settling behavior of the AANF is very important for MB-OFDM systems in the presence of single-channel interference. The reason for this is the abrupt change of the signal level between channels. This settling time is a function of f_{BW}, and presents a tradeoff in system performance. Increasing f_{BW} decreases settling time, however, it also attenuates additional adjacent

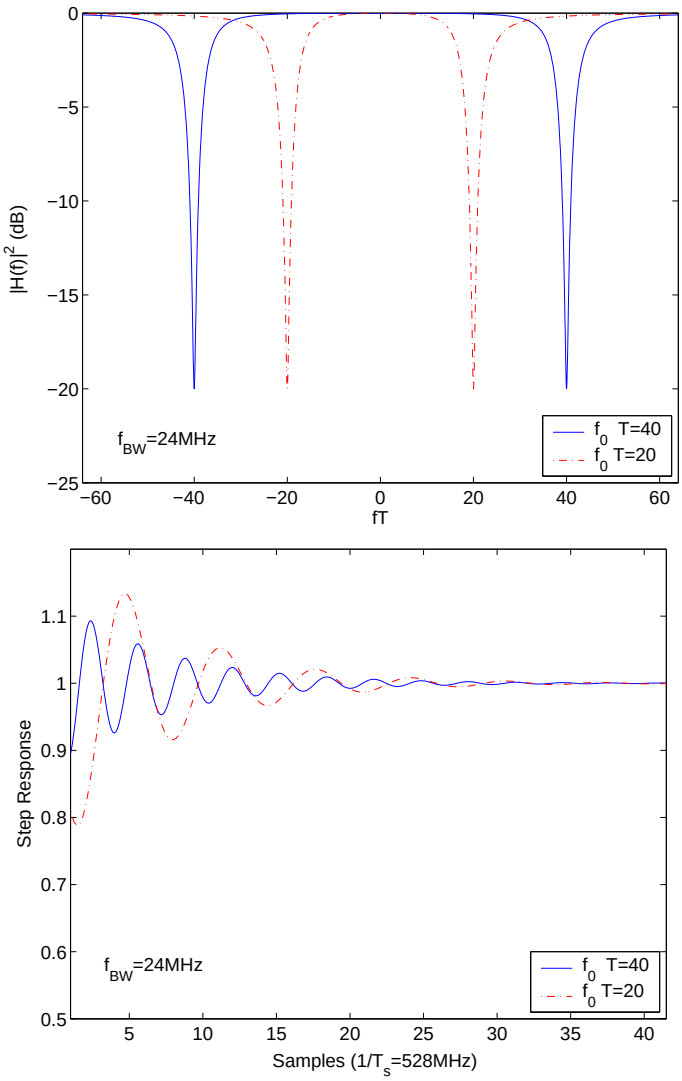

Fig. 45. The amplitude and step response of adaptive analog notch filter, $A_{notch} = -20\text{dB}$, $f_{BW} = 24\text{MHz}$.

subcarriers. The optimum f_{BW} is determined by simulations for MB-OFDM, the results of which are provided in Fig. 46. These results indicate an optimum f_{BW} of 24 MHz, however, this is only a slight optimum and the BLER of the system is fairly independent over f_{BW} of interest.

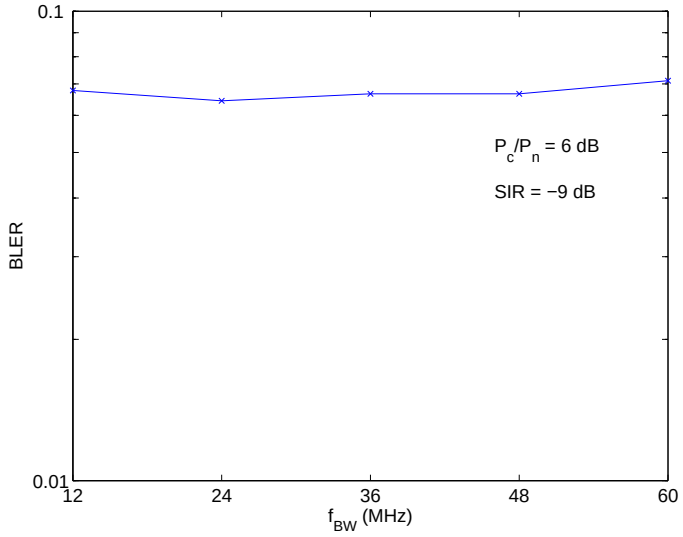

Fig. 46. Simulated BLER versus f_{BW} of AANF.

The AANF architecture is based on feed-forward cancelation, and results from the fact that subtracting a unity-gain bandpass frequency response from a unity-gain all-pass frequency response yields a notch filter, as depicted in Fig. 47. A circuit level implementation is provided in Fig. 48. The Laplace transfer function including operational transconductance amplifier (OTA) output conductance [82] is derived as:

$$\frac{v_o}{v_i} = \frac{g_{m6}}{g_{m7}} \frac{s^2 + \left(\frac{g_{m2} + g_{o2} - g_{m1}}{C_1} + \frac{g_{o3}}{C_2}\right) s + \frac{g_{m3}g_{m4} + g_{o3}\left(g_{m2} + g_{o2}\right) - g_{m1}g_{o3}}{C_1 C_2}}{s^2 + \left(\frac{g_{m2} + g_{o2}}{C_1} + \frac{g_{o3}}{C_2}\right) s + \frac{g_{m3}g_{m4} + g_{o3}\left(g_{m2} + g_{o2}\right)}{C_1 C_2}} . \tag{6.30}$$

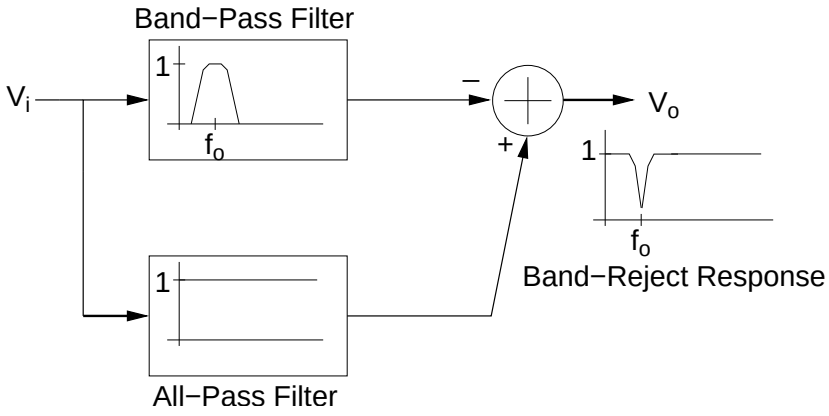

Fig. 47. Notch filter based on band-pass feed-forward cancelation.

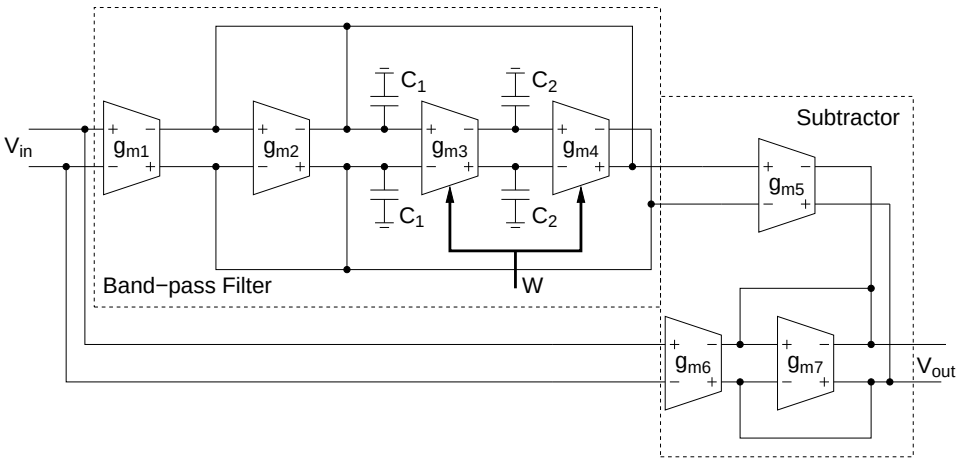

Fig. 48. Circuit structure of notch filter with a single notching frequency, f_0 controlled by the digital word, W.

The relevant characteristics of this response are provided below.

$$\begin{aligned} f_0 &\approx \sqrt{g_{m3}g_{m4}/(4\pi^2 C_1 C_2)}\ , \\ f_{BW} &= g_{o3}/2\pi C_2 + (g_{m2}+g_{o2})/2\pi C_1\ , \\ A_{notch} &= 1 - \frac{g_{m1}}{\frac{C_1}{C_2}g_{o3} + g_{m2} + g_{o2}}\ . \end{aligned}$$

An ideal notch is thus created by designing

$$g_{m1} = g_{m2} + g_{o2} + g_{o3}\frac{C_1}{C_2}\ . \tag{6.31}$$

The level of attenuation achieved will be dependent on how well this relationship holds. While it is not practical to expect (6.31) to hold in the presence of IC process variation, a simple master-slave tuning circuit [82] has been designed to adjust g_{m1} to make the error as small as possible. Transistor level simulations have shown A_{notch} to be on the order of -40 dB.

To combat NBI adaptively, the notch filter was designed to be tunable in the whole reception bandwidth. For the MB-OFDM proposal [27], the bandwidth of one sub-band is 528 MHz, spread from -264 MHz to 264 MHz. Since the frequency response of AANF is symmetric across DC, the tuning range of the filter must extend from near DC up to 264 MHz. As discussed before, the DSP part can detect not only the existence but also the location of NBI, $f_{int} = [f_i/T]$. Based on f_{int}, the notch filter is linearly controlled such that $f_0 = f_{int}$. This is done using banks of OTAs, which are digitally controlled by placing switches at their supply inputs. The number of bits required for controlling the filter is determined by the level of interference attenuation that is needed by the system. If it is desired that any interference could be attenuated by at least 20 dB, it needs to be ensured that the -20 dB bandwidth of the filter is greater than the center frequency step size. The -3 dB bandwith of the AANF

optimizes MB-OFDM receiver performance at $f_{BW} = 24$ MHz. This corresponds to a -20 dB bandwidth of around 2.4 MHz. With a maximum center frequency of 264 MHz, this requires there to be at least 110 discrete center frequency locations, indicating at least a 7-bit control word. In this work, an 8-bit control word was used in order to sufficiently compensate for temperature and IC process variations. Figure 49 displays the AANF's magnitude response for three consecutive control words (W) of 100, 101, and 102. The magnitude response for any W overlaps the adjacent response around -28 dB. Figure 50 displays how the filter characteristics change with respect to W. The designed filter provides a linear relationship between the center frequency and the control word with a slope of 1.2 MHz/Unit. Furthermore, the -3 dB and -20 dB bandwidths remain relatively unchanged across all W. The slight changes in bandwidths are attributed to the above mentioned feedback scheme that maximizes attenuation by compensating for the output conductance of the OTAs.

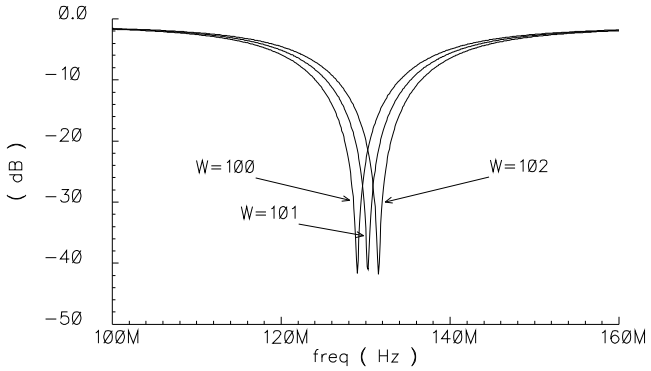

Fig. 49. AANF frequency response versus W, $A_{notch} = -40$dB.

Due to temperature and IC process variations, a mapping from the digital control to the filter characteristics will change from time to time, and needs to be adaptively learned by DSP. The algorithm used for this purpose is a guess and search outward

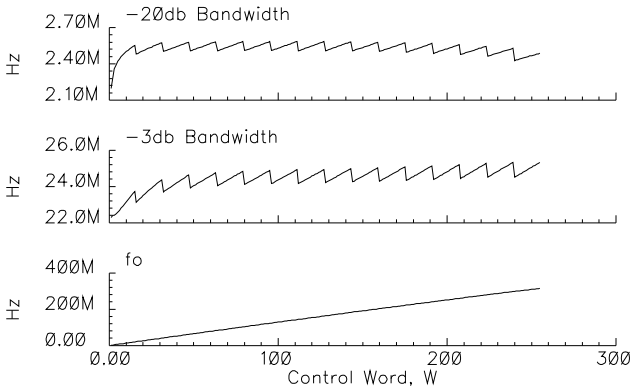

Fig. 50. AANF filter characteristics versus W, $A_{notch} = -40$dB.

algorithm (GSO). The flow of the GSO algorithm is shown in Fig. 51.

Once interference is initially detected via the FFT, the notch filter will be turned on. The control word (W) will be set assuming f_0 varies linearly with W, having a slope of $\rho = f_0/W$. The value of ρ will be adaptively learned by the algorithm, and is initially set to the simulated value (in this case 1.2 MHz/Unit). Once interference is detected and located, we let $W_0 = f_{int}/\rho$. In all likelihood, due to process or temperature variations, f_0 will not match that of the interference during this first try and the interference will still appear at the output of the FFT [2]. W is then decreased by one, and the FFT is taken again. If the interference still exists, W is increased by 2, and pending an incorrect control, will be decreased by 3, such that on the kth attempt, the control word will be:

$$W_k = W_{k-1} + (-1)^{k-1}(k-1)\,. \tag{6.32}$$

This outward search will continue until the interference is sufficiently attenuated in

[2]One may think f_0 can be learned by detecting the notch in the output of FFT. However, it is found that detecting such notch could be very unreliable, if the additive noise is much weaker than NBI.

the output of the FFT. Once the filter has been properly adjusted, a new value can be computed for the slope, according to $\rho = W/f_{int}$. This will be used for the slope the next time an interference is detected. By adaptively changing ρ, the time required for convergence will be reduced for subsequent interference because the control of the filter is effectively learned by the algorithm.

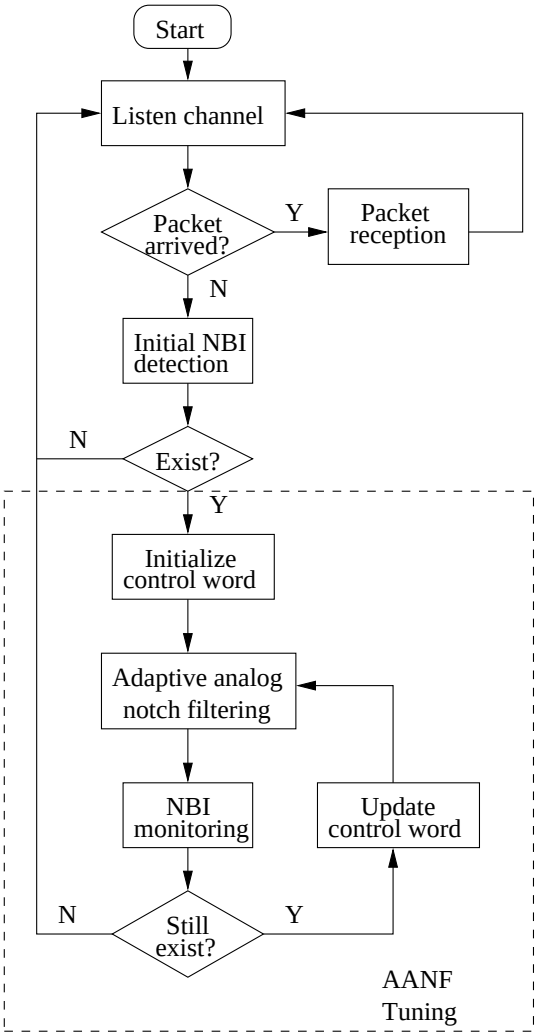

Fig. 51. The working flow of proposed NBI suppression scheme.

Note that the NBI could disappear or change in frequency after a short while. Although not shown in Fig. 51, a proper working policy to monitor such events should

be considered in practice. One possible way is that, the notch filter is switched off periodically so that the change of NBI can be monitored by the receiver.

For simplicity, the above discussions assume the NBI detection and suppression for one sub-band of MB-OFDM receiver. However, by using the same algorithm as discussed above, and scanning through all sub-bands, these results have been extended to the multi-band OFDM receiver.

3. Performance of the Mixed NBI Suppression Scheme

To evaluate the performance of the proposed NBI suppression scheme, we run computer simulations that assume a multi-band OFDM receiver. The simulation parameters are given in Table II.

In the first test, we assume that a single NBI with a fixed frequency $f_{int} = 20$ is present in the sub-band 1, and there are no NBIs for the other two sub-bands. Therefore, the AANF will be used only for the sub-band 1. Also, a frequency-hopping pattern of [1 2 3] is used by the transmitter, while in the receiver we assume perfect timing synchronization.

In Fig. 52, we compare the time and frequency domain signals of the MB-OFDM systems with or without AANF. Fig. 52-(a) and (b) plot the signal in the time domain and the frequency domain, where no AANF is applied. As illustrated in Fig. 52-(a), the NBI level is 10 times larger than the signal level in the time domain for sub-band 1. In the frequency domain, Fig. 52-(b) shows that the PSD of NBI is much higher than the PSD of OFDM signal.

In Fig. 52-(c) and (d), we plot the signals of the MB-OFDM receiver with AANF. Comparing Fig. 52-(c) and Fig. 52-(a), one can find that the NBI is significantly reduced by AANF. Thanks to the NBI reduction, the signal level in Fig. 52-(d), is higher than that in Fig. 52-(b), which indicates that AANF leads to a better usage

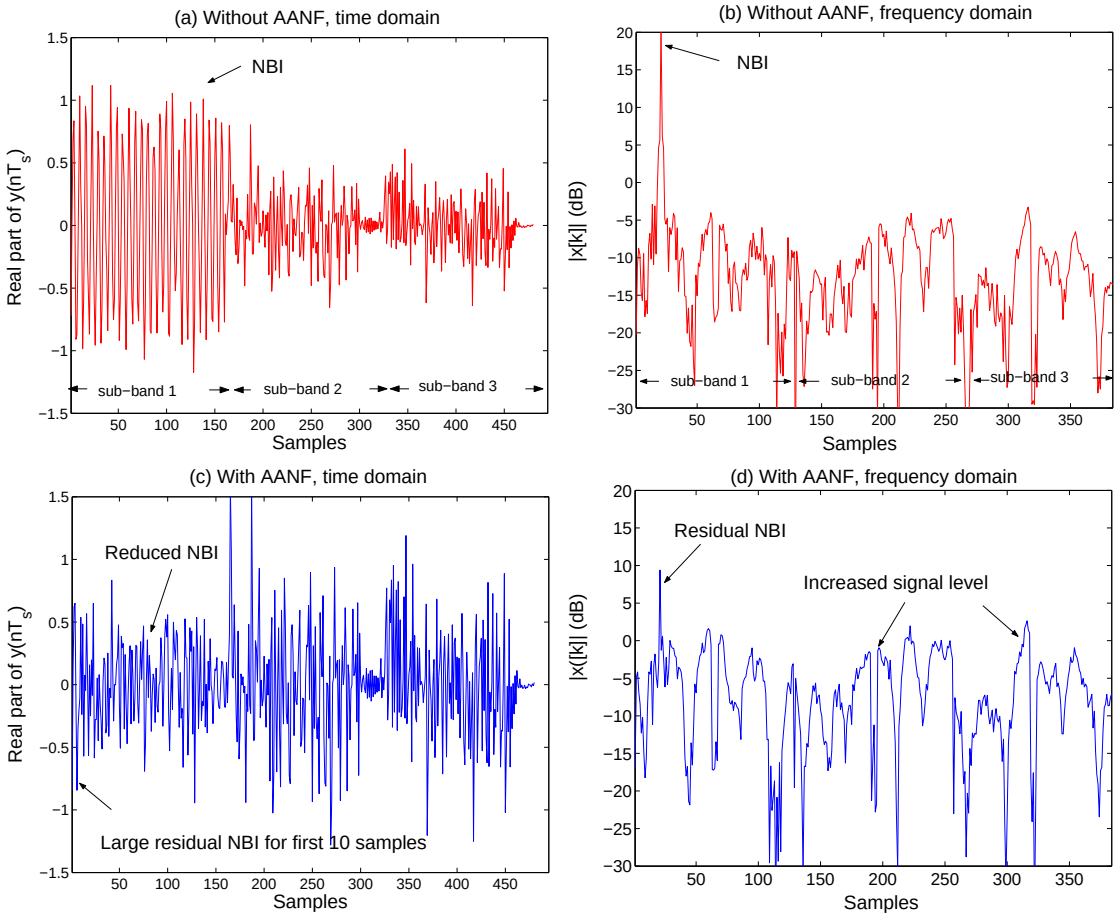

Fig. 52. Time and frequency domain signals after AGC: without or with adaptive analog notch filter, SIR=−10dB, $f_{int} = 20$, $A_{notch} = -20$dB, $f_{BW} = 24$MHz.

of the ADC bits. If $A_{notch} = -20$ dB, one might expect that after AANF filtering, the residual NBI level should be 20 dB lower than the original level, which however is not true. As shown in Fig. 52-(d), the residual NBI is is still close to 10 dB. It is found that this large residual NBI is caused by the long settling time of AANF. As illustrated in Fig. 45, it takes the AANF more than $10T_s$ to settle down. Note that, due to the frequency hopping, the interference level observed by baseband processing is varying over different sub-bands. Therefore, during the sub-band switching time, the notch filter presents poor performance and a large residual NBI is found for the first 10 samples in Fig. 52-(c).

We also run link level simulations to evaluate the effectiveness of the proposed NBI suppression scheme. The BLER curves in Fig. 53 shows that, compared to the digital frequency excision scheme, the proposed mixed (hybrid) scheme presents a better performance at low SIRs. For example, to achieve BLER=0.1, the receiver with digital frequency excision needs SIR> -3 dB while the receiver with the proposed mixed scheme can allow SIR as low as -12 dB.

At SIR> 0 dB, there is a crossover between the BLER curves of two NBI suppression schemes, and the performance of the proposed scheme is slightly lower, a fact which can be explained by the signal loss caused by notch filtering. This result suggests that we should not use the analog notch filter at SIR> 0 dB where the digital notch filtering is sufficient for NBI suppression. In this case, the AANF can be turned off simply by removing the band-pass feed-forward path in Fig. 47.

E. Summary

This chapter has conducted an in-depth study to assess the impact of a narrowband interference on the performance of a MB-OFDM UWB receiver. It was found that

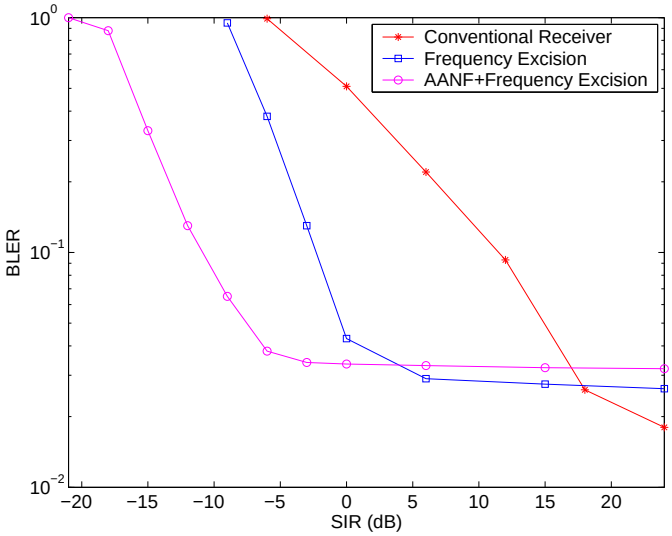

Fig. 53. Performance comparison of MB-OFDM receiver, ideal NBI detection, 200Mbps date rate, UWB channel model 1.

mild interferences could be mitigated by using a low-complexity digital frequency excision method without introducing any severe performance degradation. However, to suppress more efficiently severe interferences, a novel mixed-mode mitigation scheme has been proposed based on the joint cooperation between an adaptive analog notch filter and a digital NBI detector. Computer simulations illustrated that significant performance improvements are due to the proposed NBI mitigation schemes. The present chapter has also presented a detailed analysis of the effects of NBI on the operation of ADC and carrier synchronization algorithm, and proposed several results to optimize the design of ADC and carrier synchronizer. Given that the MB-OFDM UWB proposal appears as one of the most important competitors for the IEEE 802.15.3a standard and the outstanding record of the OFDM modulation of being already adopted in numerous standards, the problem of suppressing the impact of NBI appears of paramount importance in the design of future generation of MB-OFDM UWB transceivers.

CHAPTER VII

CONCLUSIONS

In this dissertation, we have investigated signal acquisition algorithms for both narrowband and wideband wireless communications systems.

Significant efforts have been put into timing recovery in narrowband systems. In Chapter II, a new two-step timing recovery scheme have been proposed to avoid the hang-up problem. The analysis and simulation results show that this simple scheme greatly speeds up the timing recovery for both linearly and nonlinearly modulated systems. The self-noise analysis in Chapter III leads to the finding of a novel prefiltering technique for blind feedforward timing recovery schemes.

High performance synchronization for wideband systems is discussed in Chapter IV and V. In Chapter IV, a novel and robust synchronization scheme is proposed for efficient coarse carrier frequency offset and timing acquisition in OFDM systems. A new decision directed tracking scheme is also discussed in Chapter V. Both theoretical analysis and simulation results indicate that the proposed algorithms greatly improve the performance of standard OFDM receivers.

In Chapter VI, in-depth study has been conducted to assess the impact of narrowband interference on the performance of MB-OFDM UWB receivers. To suppress severe interferences, a novel mixed-mode mitigation scheme has been proposed based on the joint cooperation between an adaptive analog notch filter and a digital NBI detector. One of future open problems is to extend the proposed scheme for NBI mitigation in non-OFDM systems.

REFERENCES

[1] U. Mengali and A. N. D'Andrea, *Synchronization Techniques for Digital Receivers*, Plenum Press, New York, NY, 1997.

[2] H. Meyr, M. Moeneclaey, and S. A. Fechtel, *Digital Communication Receivers: Synchronization, Channel Estimation and Signal Processing*, John Wiley & Sons Inc., Hoboken, NJ, 1998.

[3] M. K. Simom, J. K. Omura and R. A. Scholtz, *Spread Spectrum Communications Handbook*, revised version, McGraw-Hill, New York, NY, 1994.

[4] W. C. Lindsey and M. K. Simon, *Telecommunication System Engineering*, Prentice Hall, Englewood Cliffs, NJ, 1972.

[5] L. B. Milstein, "Interference rejection techniques in spread spectrum communications," in *Proc. IEEE*, vol. 76, no. 6, pp. 657-671, June 1988.

[6] J. D. Laster and J. H. Reed, "Interference rejection in digital wireless communications," *IEEE Signal Proc. Mag.*, vol. 14, no. 3, pp. 37 - 62, May 1997.

[7] F. M. Gardner, "Hangup in phase-lock loops," *IEEE Trans. on Commun.*, vol. COM-25, no. 4, pp. 1210-1214, Oct. 1977.

[8] H. Meyr and L. Popken, "Phase acquisition statistics for phase-locked loops," *IEEE Trans. on Commun.*, vol. 28, no. 6, pp. 1365-1372, Aug. 1980.

[9] F. M. Gardner, "Equivocation as a cause of PLL hangup", *IEEE Trans. on Commun.*, vol. COM-25, no. 7, pp. 1210-1214, Oct. 1977.

[10] M. Oerder and H. Meyr, "Digital filter and square timing recovery," *IEEE Trans. on Commun.*, vol.36, no. 5, pp. 605-612, May 1988.

[11] K. E. Scott and E. B. Olasz, "Simultaneous clock phase and frequency offset estimation," *IEEE Trans. on Commun.*, vol. 43, no. 7, pp. 2263-2270, July 1995.

[12] Y. Wang, P. Ciblat, E. Serpedin and P. Loubaton, "Performance analysis of a class of nondata-aided frequency offset and symbol timing estimators for flat-fading channels," *IEEE Trans. on Signal Processing*, vol. 5, no. 9, pp. 2295-2305, Sept. 2002.

[13] F. Gini and G. B. Giannakis, "Frequency offset and symbol timing recovery in flat-fading channels: a cyclostationary. approach," *IEEE Trans. on Commun.*, vol. 46, no. 3, pp.400-411, Mar. 1998.

[14] S. J. Lee, "A new non-data-aided feedforward symbol timing estimator using two samples per symbol," *IEEE Commun. Lett.*, vol. 6, no. 5, pp. 205-207, May 2002.

[15] Y. Wang, E. Serpedin and P. Ciblat, "An alternative blind feedforward symbol timing estimator using two samples per symbol," *IEEE Trans. on Commun.*, vo. 51, no. 9, pp. 1451-1455, Sept. 2003.

[16] F. M. Gardner, "Self-noise in synchronizers," *IEEE Trans. on Commun.*, vol. COM-28, no. 6, pp. 1159-63, Aug. 1980.

[17] R. van Nee and R. Prasad, *OFDM for Wireless Multimedia Communications*, Artech House, Norwood, MA, 2000.

[18] P. H. Moose, "A technique for orthogonal frequency division multiplexing frequency offset correction," *IEEE Trans. on Commun.*, vol. 42, no. 10, pp. 2908-2914, Oct. 1994.

[19] T. M. Schmidl, and D. C. Cox, "Robust frequency and timing synchronization for OFDM," *IEEE Trans. on Commun.*, vol. 45, no. 12, pp. 1613-1621, Dec.1997.

[20] S. H. Muller-Weinfurtner, "On the optimality of metrics for coarse frame synchronization in OFDM: a comparison," in *Proc. Int. Symp. on Personal, Indoor and Mobile Radio Comm.*, vol. 2, pp. 533-537, Sept. 1998.

[21] H. Minn, M. Zeng, and V. K. Bhargava, "On timing offset estimation for OFDM systems," *IEEE Commun. Lett.*, vol. 4, no. 12, pp. 242-244, July 2000.

[22] J. J. van de Beek, M. Sandell, and P. O. Borjesson, "ML estimation of time and frequency offset in OFDM systems," *IEEE Trans. on Signal Processing*, vol.45, no. 7, pp.1800-1805, July 1997.

[23] N. Lashkarian, and S. Kiaei, "Class of cyclic-based estimators for frequency-offset estimation of OFDM systems," *IEEE Trans. on Commun.*, vol. 48, no. 12, pp. 2139-2149, Dec. 2000.

[24] A. J. Coulson, "Maximum likelihood synchronization for OFDM using a pilot symbol: algorithm," *IEEE Journal on Selected Areas in Commun.*, vol.19, no. 12, pp.2486-2494, Dec. 2001.

[25] A. J. Coulson, "Maximum likelihood synchronization for OFDM using a pilot symbol: analysis," *IEEE Journal on Selected Areas in Commun.*, vol.19, no. 12, pp.2495-2503, Dec. 2001.

[26] F. Tufvesson, O. Edfors and M. Faulkner, "Time and frequency synchronization for OFDM using PN-sequence preambles," in *Proc. IEEE Vehicular Tech. Conf.*, vol.4, pp. 2203-7, Sept. 1999.

[27] A. Batra, J. Balakrishnan, A. Dabak, R. Gharpurey, J. Lin, et al., "Multi-band OFDM physical layer proposal," IEEE P802.15-04/0493r1-TG3a, ftp://ftp.802wirelessworld.com/15/, Sept. 2004.

[28] Federal Communications Commission, "New public safety applications and broadband internet access among uses envisioned by FCC authorization of ultra-wideband technology," http://www.fcc.gov/Bureaus/Engineering Technology/News Releases/2002/nret0203.html, Feb. 2002.

[29] K. H. Muller and M. Muller, "Timing recovery in digital synchronous data receivers," *IEEE Trans. on Commun.*, vol. 24, pp. 516-531, no. 5, May 1976.

[30] F. M. Gardner, "A BPSK/QPSK timing error detector for sampled receivers," *IEEE Trans. on Commun.*, vol. 34, no. 5, pp. 423-429, May 1986.

[31] A. N. D'Andrea, U. Mengali and R. Reggiannini, "A digital approach to clock recovery in generalized minimum shift keying," *IEEE Trans. on Vehicular Tech.*, vol. 39, no. 8, pp. 227-234, Aug. 1990.

[32] F. Dolivo, W. Schott and G. Ungerbock, "Fast timing recovery for partial-response signal systems," in *Proc. of IEEE Int. Commun. Conf.*, vol. 1, pp. 0573-0577, 1989.

[33] F. M. Gardner, "Interpolation in digital modems-part I: fundamentals," *IEEE Trans. on Commun.*, vol. COM-41, no. 3, pp. 501-507, Mar. 1993.

[34] L. Erup, F. M. Gardner and R. A. Harris, "Interpolation in digital modems-part II: implementation and performance," *IEEE Trans. on Commun.*, vol. COM-41, no. 6, pp. 998-1008, June 1993.

[35] W. G. Cowley, "The performance of two symbol timing recovery algorithms for PSK demodulators," *IEEE Trans. on Commun.,* vol. 42, no. 6, pp. 2345-2355, June 1994.

[36] M. Morelli and U. Mengali, "Joint frequency and timing recovery for MSK-type modulation," *IEEE Trans. on Commun.,* vol. 47, no. 6, pp. 938-946, June 1999.

[37] P. Ciblat, P. Loubaton, E. Serpedin and G. B. Giannakis, "Asymptotic analysis of blind cyclic correlation based symbol rate estimators," *IEEE Trans. Inform. Theory*, vol. 48, no. 7, pp. 1922-1934, July 2002.

[38] L. E. Franks and J. P. Bubrouski, "Statistical properties of timing jitter in a PAM timing recovery scheme," *IEEE Trans on Commun.*, vol. COM-22, no. 5, pp. 913-920, July 1974.

[39] A. N. D'Andrea, U. Mengali and M. Moro, "Nearly optimum prefiltering in clock recovery," *IEEE Trans. on Commun.*, vol. COM-34, no. 11, pp. 1081-88, Nov. 1986.

[40] A. N. D'Andrea, and M. Luise, "Design and analysis of a jitter-free clock recovery scheme for QAM systems," *IEEE Trans. on Commun.*, vol. 41, no. 9, pp. 1296-1299, Sept. 1993.

[41] A. N. D'Andrea, and M. Luise, "Optimization of symbol timing recovery of QAM data demodulators," *IEEE Trans. on Commun.*, vol. 44, no. 9, pp. 399-406, Sept. 1996.

[42] K. Schmidt and A. Wittneben, "Systematic complexity reduction for digital square timing recovery," in *Proc. IEEE Vehicular Tech. Conf.*, vol. 1, pp. 283-288, May 1992.

[43] P. A. Laurent, "Exact and approximate construction of digital phase modulations by superposition of amplitude modulated pulses," *IEEE Trans. on Commun.*, vol. COM-34, no. 2, pp. 150-160, Feb. 1986.

[44] R. Mehlan, Y. Chen and H. Meyr, "A fully digital feedforward MSK demodulator with joint frequency offset and symbol timing estimation for burst mode mobile radio," *IEEE Trans. on Vehicular Tech.*, vol. 42, no. 11, pp. 434-443, Nov. 1993.

[45] U. Lambrette and H. Meyr, "Two timing recovery algorithms for MSK," in *Proc. IEEE Int. Commun. Conf.*, vol. 3, pp. 1155-1159, May 1994.

[46] Y. Wu and T. Ng, "Symbol timing recovery for GMSK modulation based on square algorithm," *IEEE Commun. Lett.*, vol. 5, no. 5, pp. 221-223, May 2001.

[47] M. Morelli and G. M. Vitetta, "Joint phase and timing recovery for MSK-type signals," *IEEE Trans. on Commun.*, vol. 48, no. 12, pp. 1997-1999, Dec. 2000.

[48] K. Shi, Y. Wang and E. Serpedin, "On the design of digital blind feedforward jitter free timing recovery schemes for linear modulations," *IEEE Trans. on Commun.*, vol. 52, no. 9, pp. 1464-1469, Sept. 2004.

[49] M. Speth, S. A. Fechtel, G. Fock and H. Meyr, "Optimum receiver design for wireless broad-band systems using OFDM–part I," *IEEE Trans. on Commun.*, vol.47, no. 11, pp.1668-1677, Nov. 1999.

[50] M. Speth, S. A. Fechtel, G. Fock and H. Meyr, "Optimum receiver design for wireless broad-band systems using OFDM–part II," *IEEE Trans. on Commun.*, vol.49, no. 4, pp.571-578, April. 2001.

[51] E. Sourour and G.E. Bottomley, "Effect of frequency offset on DS-SS acquisition in slowly fading channels," in *Proc. IEEE Wireless Commun. and Networking*

Conf., vol.2, pp.569-573, Sept. 1999.

[52] S. A. Fechtel, "OFDM carrier and sampling frequency synchronization and its performance on stationary and mobile channels," *IEEE Trans. on Consumer Electronics*, vol. 46, no. 8, pp. 438-441, Aug. 2000.

[53] M. Morelli, U. Megali, "An improved frequency offset estimator for OFDM applications," *IEEE Commun. Lett.*, vol. 3, no. 3, pp.75-77, March 1999.

[54] M. Morelli, U. Mengali, "Carrier-frequency estimation for transmmsion over selective channels," *IEEE Trans. on Commun.*, vol. 48, no. 9, pp. 1580-1589, Sept. 2000.

[55] J. Li, G. Liu, G. B. Giannakis, "Carrier frequency offset estimation for OFDM-based WLANs," *IEEE Signal Processing Lett.*, vol. 8, no. 5, pp. 80-82, May 2001.

[56] T. Keller, L. Piazzo, P. Mandarini, and L. Hanzo, "Orthogonal frequency division multiplex synchronization techniques for frequency-selective fading channels," *IEEE Journal on Selected Areas in Commun.,* vol. 19, no. 6, pp. 999-1008, June 2001.

[57] T. Pollet and M. Moeneclaey, "The BER performance of OFDM systems using non-synchronized sampling," in *Proc. IEEE GLOBECOM,* vol. 1, pp. 253-257, Dec. 1994.

[58] K. K. Dong, H. D. Sang, C. B. Hong, C. J. Hyung, and K. B. Ki "A new joint algorithm of symbol timing recovery and sampling clock adjustment for OFDM systems," *IEEE Trans. on Consumer Electronics*, vol. 44, no. 8, pp. 1142-1149, Aug. 1998.

[59] M. J. F. -G. Garcia, and J. M. Paez-Borrallo, "Tracking of time misalignments for OFDM systems in multipath fading channels," *IEEE Trans. on Consumer Electronics*, vol. 48, no. 11, pp. 982-989, Nov. 2002.

[60] B. Yang, K. B. Letaief, R. S. Cheng and Z. Cao, "Timing recovery for OFDM transmission," *IEEE Journal on Selected Areas in Commun.*, vol. 18, no. 11, pp. 2278-2290, Nov. 2000.

[61] K. Shi and E. Serpedin, "On the estimation of sampling clock frequency offset in single and multiple carrier systems", in *Proc. CISS*, vol. 1, pp. 474-478, March 17-19, Princeton, NJ, 2004.

[62] M. Luise and R. Reggiannini, "Carrier frequency recovery in all-digital modems for burst-mode transmissions," *IEEE Trans. on Commun.,* vol. 43, no. 2, pp. 1169-1178, Feb./March/April 1995.

[63] K. Nikitopoulos and A. Polydoros, "Compensation schemes for phase noise and residual frequency offset in OFDM systems," in *Proc. IEEE GLOBECOM Conf.*, vol. 1, pp. 330-333, Nov. 2001.

[64] L. Yang and G. B. Giannakis, "Ultra-wideband communications: an idea whose time has come," *IEEE Signal Processing Magazine*, vol. 21, no. 11, pp. 26-54, Nov. 2004.

[65] R. Morrow, *Wireless Network Coexistence*, McGraw-Hill, New York, NY, 2004.

[66] J. Ellis and K. Siwiak, "P802.15. 3a alternative PHY selection criteria," *IEEE P802.15-03/031r5*, http://www.802wirelessworld.com, Dec. 2002.

[67] L. Yang and G. B. Giannakis, "Ultra-wideband multiple access: unification and narrowband interference analysis," in *Proc. IEEE Conference on Ultra Wideband*

Systems and Technologies, vol. 1, pp. 320-324, Nov. 2003,

[68] B. Widrow, "Adaptive noise canceling: principles and applications," in *Proc. IEEE*, vol. 63, no. 12, pp. 1692-1716, Dec. 1975.

[69] L. B. Milstein, "An analysis of a real-time transform domain filtering digital communication system, part I: narrowband interference rejection," *IEEE Trans. on Commun.*, vol. 28, no. 6, pp. 816-824, June 1980.

[70] L. Li and L. B. Milstein, "Rejection of narrow-band interference in PN spread-spectrum systems using transversal filters," *IEEE Trans. on Commun.*, vol. 30, no. 5, pp. 925-928, May 1982.

[71] J. Max, "Quantizing for minimum distortion," *IRE Trans. on Information Theory*, vol. 6, no. 3, pp. 7-12, March 1960.

[72] A. Moschitta and D. Petri, "Wideband communication system sensitivity to overloading quantization noise," *IEEE Trans. on Instrumentation and Measurement*, vol. 52, no. 8, pp. 1302-1307, Aug. 2003.

[73] A. Moschitta and D. Petri, "Stochastic properties of quantization noise in memoryless converters affected by integral nonlinearity," *IEEE Trans. on Instrumentation and Measurement*, vol. 53, no. 8, pp. 1179-1183, Aug. 2004.

[74] B. Muquet, Z. Wang, G. B. Giannakis, M. de Courville, and P. Duhamel, "Cyclic prefix or zero padding OFDM for wireless multicarrier transmissions," *IEEE Trans. on Commun.*, vol. 50, no. 12, pp. 2136-2148, Dec. 2002.

[75] A. Batra, J. Foerster, and R. Aiello, "Design of a multiband OFDM system for realistic UWB channel environments," *IEEE Trans. on Microwave Theory and Techniques*, vol. 52, no. 9, pp. 2123-2138, Sept. 2004.

[76] J. Foerster, Ed., "Channel modeling sub-committee report final," IEEE802.15-02/490, http://www.802wirelessworld.com, Nov. 2002.

[77] Y. Kamiya and O. Besson, "Interference rejection for frequency-hopping communication systems using a constant power algorithm," *IEEE Trans. on Commun.*, vol. 51, no. 4, pp. 627-633, April 2003.

[78] A. J. Coulson, "Narrowband interference in pilot symbol assisted OFDM systems," *IEEE Trans. on Wireless Commun.*, vol. 3, no. 11, pp. 2277-2287, Nov. 2004.

[79] I. Bergel, E. Fishler, and H. Messer, "Narrowband interference suppression in time-hopping impulse-radio systems," in *Proc. IEEE Conf. on Ultra Wideband Systems and Technologies*, vol. 1, pp. 303-307. May 2002.

[80] R. Vijayan and H. V. Poor, "Nonlinear techniques for interference suppression in spread-spectrum systems," *IEEE Trans. on Communications*, vol. 38, no. 7, pp. 1060-1065, July 1990.

[81] T. Fujisawa, J. Hasegawa, K. Tsuchie, T. Shiozawa, T. Fujita, et al., "A single-chip 802.11a MAC/PHY with a 32-b RISC processor," *IEEE Trans. on Solid-state Circuits*, vol. 38, no. 11, pp. 2001-2009, Nov. 2003.

[82] R. Schaumann, M. S. Ghausi, and K. R. Laker, *Design of Analog Filters: Passive, Active RC and Switched-Capacitor,* Prentice-Hall, Englewood Cliffs, NJ, 1990.

[83] J. G. Proakis, *Digital Communications*, fourth edition, McGraw-Hill, New York, NY, 2000.

APPENDIX A

EVALUATION OF SELF-NOISE POWER FOR $P = 2$

We assume without any loss of generality that the transmit symbol stream belongs to an M-QAM or M-PSK modulation with $M > 2$ (the case of a real-valued (BPSK/PAM) modulation supports only a minor modification). For $P = 2$, the quadrature and in-phase components of the jitter can be expressed as:

$$\begin{aligned} Q_{ss} &= G^2(1)\sin^2(2\pi\epsilon)A + G^2(0)\cos^2(2\pi\epsilon)B - G(0)G(1)\sin(4\pi\epsilon)C \\ I_{ss} &= G^2(1)\cos^2(2\pi\epsilon)A + G^2(0)\sin^2(2\pi\epsilon)B + G(0)G(1)\sin(4\pi\epsilon)C \end{aligned} \quad \text{(A.1)}$$

where

$$\begin{aligned} A &:= \sum_{n=0}^{PN-1}\sum_{m=0}^{PN-1} |x[n]|^2|x[m]|^2 e^{\frac{-j2\pi(n+m)}{P}} , \\ B &:= \sum_{n=0}^{PN-2}\sum_{m=0}^{PN-2} \Re\{x^*[n]x[n+1]\}\Re\{x^*[m]x[m+1]\}e^{\frac{-j2\pi(n+m)}{P}}, \\ C &:= \sum_{n=0}^{PN-2}\sum_{m=0}^{PN-1} \Re\{x^*[n]x[n+1]\}|x[m]|^2 e^{\frac{-j2\pi(n+m)}{P}}. \end{aligned} \quad \text{(A.2)}$$

The expectation of $|x[m]|^2|x[n]|^2$ can be expressed by

$$\begin{aligned} E\{|x[m]|^2|x[n]|^2\} &= \sum_l \sum_i g_0[m - lP - \epsilon P]g_0[n - iP - \epsilon P] && (= E_1) \\ &+ \sum_l \sum_i g_l[m - iP - \epsilon P]g_l[n - iP - \epsilon P] && (= E_2) \\ &+ (\gamma - 2)\sum_i g_0[m - iP - \epsilon P]g_0[n - iP - \epsilon P] && (= E_3) \end{aligned} \quad \text{(A.3)}$$

where $g_l[n] := h[n - lP]h^*[n]$. Thus, we write the expectation of A as

$$E[A] = \sum_{n=0}^{PN-1}\sum_{m=0}^{PN-1} (E_1 + E_2 + E_3)e^{\frac{-j2\pi(n+m)}{P}} \quad \text{(A.4)}$$

Following the steps in [12], the first part of $E[A]$ is found

$$E[A_1] = \sum_{n=0}^{PN-1}\sum_{m=0}^{PN-1} E_1 e^{\frac{-j2\pi(n+m)}{P}} = \{N\sum_{l}|h[l-\epsilon P]|^2 e^{\frac{-j2\pi l}{P}}\}^2 = G^2(0)\cos^2(2\pi\epsilon)N^2. \tag{A.5}$$

Making use of Parseval's theorem, we find

$$\begin{aligned} E[A_2] &= \sum_{n=0}^{PN-1}\sum_{m=0}^{PN-1} E_2 e^{\frac{-j2\pi(n+m)}{P}} \\ &= \sum_{l}\sum_{i}\left[\sum_{m}\text{Rect}[NP]g_l[m-iP-\epsilon P]e^{\frac{-j2\pi m}{P}}\right]^2, \\ &= \sum_{l}\sum_{i}\left[\int_{-1/2}^{1/2} H(f+\frac{1}{P})H^{'}(f)e^{-j2\pi lfP}df\right]^2, \end{aligned} \tag{A.6}$$

where Rect$[NP]$ is a rectangular window of length NP, $H(f)$ is the FT of $h[n-\epsilon P]$ and

$$H^{'}(f) := \int_{-1/2}^{1/2} H^*(f-v)\frac{\sin(\pi NPv)}{\pi v}e^{j2\pi(N/2-i)Pv}dv. \tag{A.7}$$

For $|f| < 1/2$, $P = 2$ and $k = \pm 1$, it is found that

$$\begin{aligned} H(f) &= \frac{2}{T}H_1(\frac{2f}{T})e^{-j4\pi f\epsilon}, \\ H(f+\frac{k}{2}) &= \frac{2}{T}[H_1(\frac{2f+k}{T})e^{-j2\pi\epsilon} + H_1(\frac{2f-k}{T})e^{j2\pi\epsilon}]e^{-j4\pi kf\epsilon}. \end{aligned} \tag{A.8}$$

Thus, it follows that

$$E[A_2]=\sum_{l}\sum_{i}\left[\frac{2}{T}\int_{-1/T}^{1/T} H_1^{'}(F)[H_1(F+\frac{1}{T})e^{-j2\pi\epsilon} + H_1(F-\frac{1}{T})e^{j2\pi\epsilon}]e^{-j2\pi lFT}dF\right]^2 \tag{A.9}$$

where

$$H_1^{'}(F) := \int_{-1/T}^{1/T} H_1(F-V)\frac{\sin(\pi NVT)}{\pi V}e^{j2\pi(N/2-i+\epsilon)VT}dV.$$

Making use of Poisson's formula:

$$\sum_{l} e^{-j2\pi l(F_1+F_2)T} = \frac{1}{T}\sum_{k}\delta(F_1+F_2-\frac{k}{T}),$$

after lengthy algebra, we obtain

$$E[A_2] = \frac{4}{T^4}\int_{-1/2T}^{1/2T}\int_{-1/2T}^{1/2T} U_A(F,V)U_A(-F,-V)dF\frac{\sin^2(\pi NVT)}{\pi^2V^2}dV \ , \tag{A.10}$$

where we omit the tail of FT of rectangular window and

$$U_A(F,V) := H_2(F,V)e^{-j2\pi\epsilon} + H_2(-F,-V)e^{j2\pi\epsilon}$$

Similarly, the third part of $E[A]$ can be expressed by

$$E[A_3] = \frac{4(\gamma-2)}{T^3}\int_{-1/2T}^{1/2T} U_{A3}(V)\frac{\sin^2(\pi NVT)}{\pi^2V^2}dV \ , \tag{A.11}$$

where

$$U_{A3}(V) := \int_{-1/2T}^{1/2T}\int_{-1/2T}^{1/2T} U_A(F_1;V)U_A(F_2;-V)dF_1dF_2.$$

Following the steps (A.3)-(A.11), the expectation of B can be expressed as

$$E[B] = E[B_1] + E[B_2] + E[B_3], \tag{A.12}$$

and

$$\begin{aligned}
E[B_1] &= G^2(1)\sin^2(2\pi\epsilon)N^2, \\
E[B_2] &= -\frac{4}{T^4}\int_{-1/2T}^{1/2T}\int_{-1/2T}^{1/2T} U_B(F,V)U_B(-F,-V)dF\frac{\sin^2(\pi NVT)}{\pi^2V^2}dV \ , \\
E[B_3] &= \frac{-4(\gamma-2)}{T^3}\int_{-1/2T}^{1/2T} U_{B3}(V)\frac{\sin^2(\pi NVT)}{\pi^2V^2}dV \ ,
\end{aligned} \tag{A.13}$$

where

$$\begin{aligned}
U_B(F,V) :=& H_2(F,V)e^{-j2\pi\epsilon} - H_2(-F,-V)e^{j2\pi\epsilon}, \\
U_{B3}(V) :=& \int_{-1/2T}^{1/2T}\int_{-1/2T}^{1/2T} U_B(F_1;V)U_B(F_2;-V)dF_1dF_2.
\end{aligned}$$

And the expectation of C is computed as

$$E[C] = E[C_1] + E[C_2] + E[C_3] \ , \tag{A.14}$$

and

$$\begin{aligned}
E[C_1] &= (1/2)G(0)G(1)\sin(4\pi\epsilon)N^2, \\
E[C_2] &= \frac{4j}{T^4}\int_{-1/2T}^{1/2T}\int_{-1/2T}^{1/2T} U_C(F,V)U_C(-F,-V)e^{-j\pi FT}dF\frac{\sin^2(\pi NVT)}{\pi^2V^2}dV \ , \\
E[C_3] &= \frac{4j(\gamma-2)}{T^3}\int_{-1/2T}^{1/2T} U_{C3}(V)\frac{\sin^2(\pi NVT)}{\pi^2V^2}dV \ ,
\end{aligned} \tag{A.15}$$

where

$$U_{C3}(V) := \int_{-1/2T}^{1/2T}\int_{-1/2T}^{1/2T} U_A(F_1;V)U_B(F_2;-V)e^{-j\pi F_1T}dF_1dF_2.$$

Thus,

$$\begin{aligned}
E[Q_{ss}] \ &= \ G^2(1)\sin^2(2\pi\epsilon)E[A_2+A_3] + G^2(0)\cos^2(2\pi\epsilon) \\
&\quad \cdot \ E[B_2+B_3] - G(0)G(1)\sin(4\pi\epsilon)E[C_2+C_3] \ , \\
E[I_{ss}] \ &= \ N^2[G(1)G(0)]^2 + G^2(1)\cos^2(2\pi\epsilon)E[A_2+A_3] \\
&\quad + G^2(0)\sin^2(2\pi\epsilon)E[B_2+B_3] + G(0)G(1)\sin(4\pi\epsilon)E[C_2+C_3] \ .
\end{aligned} \tag{A.16}$$

APPENDIX B

STATISTICAL PROPERTIES OF CORRELATOR OUTPUT AT HIGH SNR

Assuming a small time offset $l < 0$ from the start of frame, the observation vector R around the location of the training symbol can be expressed as

$$R = \alpha X e^{j(2\pi\varepsilon n/N+\theta)} + W \ , \tag{B.1}$$

where $X := [X_1^T \ X_2^T \ X_3^T \ X_4^T]^T$ is the observed training symbol shifted by l samples from the correct time and $W := [W_1^T \ W_2^T \ W_3^T \ W_4^T]^T$ is the white noise vector independent w.r.t. X.

Let S_1 and S_2 denote the first and the second part of S $(= B)$ with lengths $N/4 - |l|$ and $|l|$, respectively. Thus, it is easy to rewrite $X_1 = [\underbrace{0 \cdots 0}_{|l|} \ S_1^T]^T$, $X_2 = [S_2^T \ S_1^T]^T$, $X_3 = [S_2^T \ -S_1^T]^T$ and $X_4 = [-S_2^T \ S_1^T]^T$. Let W_{i1} and W_{i2}, $i = 1, 2, 3, 4$, represent the first and the second part of W_i with lengths $|l|$ and $N/4-|l|$, respectively. The following relations hold

$$\begin{aligned}
&P_1(l) = R_1^H R_2 - R_2^H R_3 - R_3^H R_4 \\
=&\beta^{-1}\{(3N/4 - 3|l|)\sigma_s^2\alpha^2 + \alpha[W_{11}^H S_2 + W_{12}^H S_1 - W_{21}^H S_2\beta^{-1} + 2\Re(S_1^H W_{22}\beta - S_1^H W_{32}\beta^2) \\
&-2\Im(S_2^H W_{31}\beta^2) + S_1^H W_{42}\beta^3 - S_2^H W_{41}\beta^3 \ ]\} + W_1^H W_2 - W_2^H W_3 - W_3^H W_4 \\
\approx&\beta^{-1}\{(3N/4 - 3|l|)\sigma_s^2\alpha^2 + \alpha[W_{11}^H S_2 + W_{12}^H S_1 - W_{21}^H S_2\beta^{-1} + 2\Re(S_1^H W_{22}\beta - S_1^H W_{32}\beta^2) \\
&-2\Im(S_2^H W_{31}\beta^2) + S_1^H W_{42}\beta^3 - S_2^H W_{41}\beta^3]\} \ ,
\end{aligned} \tag{B.2}$$

where we omit the products of two noise vectors. Thus, $P_1(l)$ can be approximated by a complex Gaussian RV. As for $|P_1(l)| := \sqrt{\Re^2(P_1(l)) + \Im^2(P_1(l))}$, it is a Rice RV.

At high SNR, it is accurate to approximate $|P_1(l)|$ by its real part

$$|P_1(l)| \approx \Re(P_1(l)) = (3N/4 - 3|l|)\sigma_s^2\alpha^2 + \alpha\Re[W_{11}^H S_2 + W_{12}^H S_1 - W_{21}^H S_2\beta^{-1} + 2W_{22}^H S_1\beta^{-1} - 2W_{32}^H S_1\beta^{-2} + W_{42}^H S_1\beta^{-3} - W_{41}^H S_2\beta^{-3}] , \quad \text{(B.3)}$$

which is correct for $-N/4 \leq l \leq 0$ to keep the first term (signal part) positive. Similarly, for $-N/6 \leq l \leq 0$, we can approximate $|P_2(l)|$ by

$$|P_2(l)| \approx (N/2 - 3|l|)\sigma_s^2\alpha^2 + \alpha\Re(-W_{11}^H S_2 + W_{12}^H S_1 - W_{21}^H S_2\beta^{-1} + W_{22}^H S_1\beta^{-1} - W_{32}^H S_1\beta^{-2} + W_{41}^H S_2\beta^{-3} + W_{42}^H S_1\beta^{-3}) . \quad \text{(B.4)}$$

For $-N/4 \leq l \leq 0$, $|P_3(l)|$ can also be approximated as

$$|P_3(l)| \approx (N/4 - |l|)\sigma_s^2\alpha^2 + \alpha\Re(-W_{11}^H S_2 + W_{12}^H S_1 + W_{42}^H S_1\beta^{-3}) . \quad \text{(B.5)}$$

Based on (B.3)-(B.5), for $-N/6 \leq l \leq 0$, it follows that

$$P(l) \approx (3N/2 - 7|l|)\sigma_s^2\alpha^2 + \alpha\Re(-W_{11}^H S_2 + 3W_{12}^H S_1 - 2W_{21}^H S_2\beta^{-1} + 3W_{22}^H S_1\beta^{-1} - 3W_{32}^H S_1\beta^{-2} + 3W_{42}^H S_1\beta^{-3}) , \quad \text{(B.6)}$$

which is made up of a number of real Gaussian random variables. Thus, $P(l)$ can be viewed as a real Gaussian RV. As for $V(l)$, we approximate it by

$$V(l) = 3(N - |l|)\sigma_s^2\alpha^2/2 + 6\alpha\Re(W_{31}^H S_2 - W_{41}^H S_2 - W_{32}^H S_1 + W_{42}^H S_1) + 3|W_3|^2 + 3|W_4|^2 . \quad \text{(B.7)}$$

From [24], if $N/2$ is sufficiently large, according to the CLT, $V(l)$ can be approximated as a real Gaussian RV with mean and variance:

$$\mu_V := 3N/2(\sigma_s^2\alpha^2 + \sigma_w^2) , \quad \sigma_V^2 := 9N\sigma_w^2(\sigma_s^2\alpha^2 + \sigma_w^2/2) , \quad \text{(B.8)}$$

respectively. From (B.6) and (B.7), it follows that $\text{cov}(P, V) = 18(N/4 - |l|)\sigma_s^2\sigma_w^2\alpha^2$.

APPENDIX C

APPROXIMATION FOR $\Delta = P(0) - P(-1)$

If the estimated l advances one sample from the correct time, $P(l)$ can be rewritten as

$$\begin{aligned} P(-1) &\approx (3N/2-7)\sigma_s^2\alpha^2 + \alpha\Re[3(W_{12}^H + W_{22}^H\beta^{-1} - W_{32}^H\beta^{-2} + W_{42}^H\beta^{-3})S_1 \\ &\quad -(w_{11}^* + 2w_{21}^*\beta^{-1})s_2] \,, \end{aligned} \tag{C.1}$$

where W_{i1} and S_2 are replaced by the scalars w_{i1} and s_2, respectively.
In the absence of timing error, $P(l)$ becomes

$$\begin{aligned} P(0) &\approx 3N\sigma_s^2\alpha^2/2 + 3\alpha\Re[(W_{12}^H + W_{22}^H\beta^{-1} - W_{32}^H\beta^{-2} + W_{42}^H\beta^{-3})S_1 \\ &\quad +(w_{21}^* + w_{31}^*\beta^{-1} - w_{41}^*\beta^{-2} + w_5^*\beta^{-3})s_2] \,, \end{aligned} \tag{C.2}$$

where w_5 is a noise component introduced by the last sample of s_2. Thus, the difference $P(0) - P(-1)$ can be approximated by

$$P(0)-P(-1) \approx 7\sigma_s^2\alpha^2 + \alpha\Re[(w_{11}^* + w_{21}^*(3+2\beta^{-1}) + 3w_{31}^*\beta^{-1} - 3w_{41}^*\beta^{-2} + 3w_5^*\beta^{-3})s_2], \tag{C.3}$$

which can be viewed as a real Gaussian RV with mean $7\sigma_s^2\alpha^2$ and variance $(41 + 12\cos\beta)\sigma_s^2\sigma_w^2\alpha^2$.

APPENDIX D

STATISTICAL PROPERTIES OF THE CARRIER FREQUENCY OFFSET ESTIMATOR

If $l = 0$, $P_1(l)$ can be expressed as

$$P_1(0) \approx 3\alpha^2\beta^{-1}|S|^2 + \alpha(\underbrace{\beta^{-1}W_1^H + \beta^{-2}W_2^H - \beta^{-3}W_3^H}_{N_1^H})S + \alpha S^H(\underbrace{W_2 - \beta W_3 + \beta^2 W_4}_{N_2})$$
$$+W_1^H W_2 - W_2^H W_3 - W_3^H W_4 \approx 3\alpha^2\beta^{-1}|S|^2 + \alpha(N_1^H S + S^H N_2). \quad \text{(D.1)}$$

According to (4.15), the carrier frequency offset estimator is given by

$$\hat{\varepsilon} = \frac{2}{\pi}\arg\left(\frac{\Im[P_1(0)]}{\Re[P_1(0)]}\right) \approx \frac{2}{\pi}\arctan\left(\frac{3\alpha|S|^2\sin(\varepsilon\pi/2) + \Im(N_1^H S + S^H N_2)}{3\alpha|S|^2\cos(\varepsilon\pi/2) + \Re(N_1^H S + S^H N_2)}\right). \quad \text{(D.2)}$$

Using the same method as in [18], we can obtain

$$\tan\left[\frac{\pi}{2}(\hat{\varepsilon} - \varepsilon)\right] = \frac{\Im[(P_1(0)\beta]}{\Re[P_1(0)\beta]}\ . \quad \text{(D.3)}$$

If the estimation error $|\hat{\varepsilon} - \varepsilon|$ is very small, $\tan[\frac{\pi}{2}(\hat{\varepsilon} - \varepsilon)]$ can be approximated by $\frac{\pi}{2}(\hat{\varepsilon} - \varepsilon)$, and (D.3) becomes

$$\hat{\varepsilon} - \varepsilon \approx \frac{2}{\pi}\frac{\Im[P_1(0)\beta]}{\Re[P_1(0)\beta]} \approx \frac{2}{\pi}\frac{\Im(\beta N_1^H S + \beta S^H N_2)}{3|S|^2\alpha + \Re(\beta N_1^H S + \beta S^H N_2)} \approx \frac{2}{\pi}\frac{\Im(\beta N_1^H S + \beta S^H N_2)}{3|S|^2\alpha} \quad \text{(D.4)}$$

where the last approximation holds at high SNRs. From (D.4), we infer that the proposed carrier frequency offset estimator is unbiased if there is no timing error. The mean-square error of estimate $\hat{\varepsilon}$ can be obtained after some simple calculations:

$$E[(\hat{\varepsilon} - \varepsilon)^2] = \frac{16}{9 \cdot \pi^2 \cdot N \cdot \mathrm{SNR}}\ . \quad \text{(D.5)}$$

In the presence of small timing error l, from (B.2) and (D.4), it follows

$$\hat{\varepsilon} - \varepsilon \approx \frac{2}{\pi} \frac{\Im(P_1(l)\beta)}{3|S_1|^2\alpha} , \tag{D.6}$$

where $\Im(P_1(l)\beta)$ is a zero mean RV with variance $N(1+10|l|/N)\alpha^2\sigma_w^2/4$ for $|l| < N/4$. In this case, the estimator (D.2) is still unbiased and its MSE becomes

$$E[(\hat{\varepsilon} - \varepsilon)^2] \approx \frac{16 \cdot (1 + \frac{10|l|}{N})}{9 \cdot \pi^2 \cdot N \cdot \mathrm{SNR} \cdot (1 - \frac{4|l|}{N})^2} . \tag{D.7}$$

Furthermore, we can extend the above analysis to a more general framework. If a general kind of training symbol (4.33) with constant length N and frequency offset estimator (4.34) are assumed, using the same method as in (D.2)-(D.4), it is easy to obtain a similar expression for the estimation error

$$\hat{\varepsilon} - \varepsilon \approx \frac{M}{2\pi} \frac{\Im(\beta' N_1^H S + \beta' S^H N_2)}{(M-1)|S|^2\alpha} , \tag{D.8}$$

where $\beta' := \exp(-j2\pi\varepsilon/M)$, $N_1^H = \sum_{k=1}^{M-1} b_i \exp(j2k\pi\varepsilon/M) W_i^H$ and $N_2 = \sum_{k=2}^{M} b_i \exp(-j2(k-1)\pi\varepsilon/M) W_i$. Eq. (D.8) leads to the following general MSE-expression of estimator (4.34):

$$E[(\hat{\varepsilon} - \varepsilon)^2] = \frac{M^3}{4 \cdot \pi^2 \cdot (M-1)^2 \cdot N \cdot \mathrm{SNR}} . \tag{D.9}$$

APPENDIX E

PERFORMANCE ANALYSIS OF TRACKING SCHEMES IN AWGN CHANNELS

For simplicity, MPSK modulation is assumed in the following analysis. In AWGN channels, assuming correct decisions and substituting (5.3) into (5.8), one can find

$$A_{l,k} = z_{l,k}a^*_{l,k}z^*_{l-1,k}a_{l-1,k} \approx e^{j2\pi\rho\theta_k} + v_{l,k} \ , \tag{E.1}$$

where $v_{l,k} = n_{l,k}a^*_{l,k}e^{-j\phi_{l-1,k}} + n^*_{l-1,k}a_{l-1,k}e^{j\phi_{l,k}}$, and the products of two noise terms are negligible. From (5.7), denoting $\alpha = e^{-j2\pi\rho f_N}$ and making use of $\tan(a \pm b) \approx \tan(a) \pm \tan(b)$ (if $\tan(a)\tan(b) \ll 1$), we obtain:

$$\tan[4\pi\rho(\hat{f}_N - f_N)] \approx \frac{\Im(A_{l,1}\alpha)}{\Re(A_{l,1}\alpha)} + \frac{\Im(A_{l,2}\alpha)}{\Re(A_{l,2}\alpha)} \approx 4\pi\rho(\hat{f}_N - f_N) \ , \tag{E.2}$$

where $\Re(x)$ and $\Im(x)$ denote real and imaginary part of x, respectively. Substituting (E.1) into (5.8) and (E.2), it follows that

$$e_l \approx \frac{1}{4\pi\rho}\left[\frac{\Im(A_{l,1}\alpha)}{\sum_{k\in C_1}\cos(\pi\rho\epsilon k)} + \frac{\Im(A_{l,2}\alpha)}{\sum_{k\in C_2}\cos(\pi\rho\epsilon k)}\right] \approx \frac{1}{2\pi\rho K}\Im[\alpha \sum_{k\in C_1, C_2} v_{l,k}] \ , \tag{E.3}$$

where we assume $\cos(\pi\rho\epsilon k) \approx 1$ and $\sin(\pi\rho\epsilon k) \approx 0$ for small SFO ϵ. The MSE of CFO estimator can be obtained after some straightforward calculations

$$\mathrm{MSE}(\hat{f}_N) = \frac{1}{4\pi^2\rho^2 K \cdot E_s/N_o} \ . \tag{E.4}$$

Similarly, one can find the MSE of SFO estimator

$$\mathrm{MSE}(\epsilon) = \frac{4}{\pi^2\rho^2 K(K+2)^2 \cdot E_s/N_o} \ . \tag{E.5}$$

From (E.3), after some manipulations, one can find that the CFO estimation noise

$e_l = \hat{f}_N - f_N$ has the following autocorrelation

$$R_e(m) := E\{e_l e_{l+m}\} = \begin{cases} \frac{\sigma_n^2}{4\pi^2\rho^2 K}, & m = 0 \\ -\frac{\sigma_n^2}{8\pi^2\rho^2 K}, & m = \pm 1 \\ 0, & \text{otherwise} . \end{cases} \tag{E.6}$$

Thus, the power spectral density (PSD) of CFO estimation noise is given by

$$S_{\text{CFO}}(f) = T \sum_m R_e(m) e^{-j2\pi m f T} = \frac{\sigma_n^2 T[1 - \cos(2\pi f T)]}{4\pi^2\rho^2 K} . \tag{E.7}$$

Similarly, the PSD of SFO estimation noise can be obtained

$$S_{\text{SFO}}(f) = \frac{4\sigma_n^2 T[1 - \cos(2\pi f T)]}{\pi^2\rho^2 K(K+2)^2} . \tag{E.8}$$

APPENDIX F

UNBIASEDNESS OF ONE-SHOT ESTIMATOR IN FREQUENCY-SELECTIVE CHANNELS

Assuming correct decisions $\hat{a}_{l,k}$ in (5.8), we obtain

$$A_{l,1} = \sum_{k \in C_1} |H_{l,k}|^2 e^{j2\pi\rho\theta_k} + \sum_{k \in C_1} v_{l,k} \ , \tag{F.1}$$

where $v_{l,k} = n_{l,k} a^*_{l,k} H^*_{l-1,k} e^{-j\phi_{l-1,k}} + n^*_{l-1,k} a_{l-1,k} H_{l,k} e^{j\phi_{l,k}}$.

Thus, the 1st term of the right-hand side of $A_{l,1}$ can be rewritten as

$$A_{l,s1} = e^{j2\pi\rho f_N} \left(e^{-j\pi\rho\epsilon(K/2+1)} Si(\epsilon, K) \sum_{n=0}^{\tau_{max}} |h_{l,n}|^2 + \sum_{n=0}^{\tau_{max}} \sum_{m=n+1}^{\tau_{max}} \sum_{k \in C_1} 2\Re\{\Gamma_{l,n,m,k}\} e^{j2\pi\rho\epsilon k} \right) \tag{F.2}$$

where $Si(\epsilon, K) = \frac{\sin(\pi\rho\epsilon K/2)}{\sin(\pi\rho\epsilon)} \approx K/2$ and $\Gamma_{l,n,m,k} = h_{l,n} h^*_{l,m} e^{-j2\pi k(n-m)/N}$.

Defining $\Delta = n - m$, we obtain

$$\begin{aligned} \sum_{k \in C_1} 2\Re\{\Gamma_{l,n,m,k}\} e^{j2\pi\rho\epsilon k} \ &= \ h_{l,n} h^*_{l,m} e^{-j\pi(\rho\epsilon - \Delta/N)(K/2+1)} \frac{\sin[\pi K(\rho\epsilon - \Delta/N)/2]}{\sin[\pi(\rho\epsilon - \Delta/N)]} \\ &\quad + h^*_{l,n} h_{l,m} e^{-j\pi(\rho\epsilon + \Delta/N)(K/2+1)} \frac{\sin[\pi K(\rho\epsilon + \Delta/N)/2]}{\sin[\pi(\rho\epsilon + \Delta/N)]} \end{aligned} \tag{F.3}$$

Thanks to the approximation $\frac{\sin[\pi K(\rho\epsilon \pm \Delta/N)/2]}{\sin[\pi(\rho\epsilon \pm \Delta/N)]} \approx \frac{\sin[\pi\Delta K/(2N)]}{\sin(\pi\Delta/N)}$, which is valid if $\epsilon \ll \Delta/N$ [1], we can approximate (F.3) as

$$\sum_{k \in C_1} 2\Re\{\Gamma_{l,n,m,k}\} e^{j2\pi\rho\epsilon k} \approx e^{-j\pi\rho\epsilon(K/2+1)} \sum_{k \in C_1} 2\Re\{\Gamma_{l,n,m,k}\} \ , \tag{F.4}$$

---

[1] The accuracy of approximation depends on the value of ϵ. For large ϵ, the approximation is not accurate anymore and the unbiasedness of (5.7) can not be shown along this line of proof.

and rewrite $A_{l,1}$ as

$$A_{l,1} \approx e^{j2\pi\rho f_N} e^{-j\pi\rho\epsilon(K/2+1)} \sum_{k\in C_1} |H_{l,k}|^2 + \sum_{k\in C_1} v_{l,k} \ . \tag{F.5}$$

Similarly, we can make the following approximation

$$A_{l,2} \approx e^{j2\pi\rho f_N} e^{j\pi\rho\epsilon(K/2+1)} \sum_{k\in C_2} |H_{l,k}|^2 + \sum_{k\in C_2} v_{l,k} \ . \tag{F.6}$$

Substituting (F.5)-(F.6) into (5.7), it is easy to find that (5.7) is approximately unbiased for slow fading F-S channels.

VITA

Kai Shi was born in Nantong, Jiangsu Province, P. R. China. He received the Bachelor of Science degree from the Department of Electronics Science and Engineering, Nanjing University, China, in July 1998, and the Master of Engineering degree from the Department of Radio Engineering, Southeast University, Nanjing, China, in March 2001.

From 2000 to 2001, he worked as a hardware engineer with the company Bird, Nanjing, China. In 2001, he was a software engineer with Global Software Group of China Motorola. Since January 2002, he has been a Ph. D. student and research assistant with the Department of Electrical Engineering, Texas A&M University. During Summer 2004 and Spring 2005, he was a system engineering intern with Analog Devices, Wilmington, MA. His research interests include the design and implementation of digital signal processing algorithms for communication systems.

Kai Shi may be reached at Olympus Communications Technology of America, 9605 Scranton Rd. Suite 830, San Diego, CA 92121. His email address is kshi@olympus-cta.com.

The typist of this dissertation was Kai Shi.